6-16-2021

A Generalized, Modular Approach to Treating Moving Tumors with Ion Beams

Michelle Jennifer Lis
Louisiana State University and Agricultural and Mechanical College

A GENERALIZED, MODULAR APPROACH TO TREATING MOVING TUMORS WITH ION BEAMS

A Dissertation

Submitted to the Graduate Faculty of the
Louisiana State University and
Agricultural and Mechanical College
in partial fulfillment of the
requirements for the degree of
Doctor of Philosophy

in

The Department of Physics and Astronomy

by
Michelle Jennifer Lis
B.S., Loyola University Chicago, 2010
August 2021

Copyright

Acknowledgements

I would like to thank my research advisors, Dr. Wayne Newhauser and Dr. Christian Graeff, for their support and guidance throughout the course of this project. I would also like to thank the members of my research advisory committee – Dr. Joyoni Dey, Dr. Martin Tsanov, Dr. Robert Carver, and Dr. Amy Grooters – for their assistance and time. Without their mentorship, I would not be where I am today.

I would also like to thank my colleagues at GSI, including those in the detector laboratory, for developing our beamline monitors and the workshop for creating our detector holders. I'd like to also thank Dr. Marco Donetti at CNAO for training me on the delivery system that would become the basis of this project, and for his help thoughout the project, including during beamtimes at CNAO. I would like to especially thank Christoph Schuy for his support during GSI beamtimes, his work in preparing the beamlines for experiments at GSI, and his input throughout the implementation and experimental verification process. I would like to thank all of the OMA fellows, project managers and Carsten Welsch for enriching my experiences during my Ph.D., and for contributing to my professional and scientific development.

I would also like to thank members of our research group and fellow colleagues for their feedback, kind assistance, especially during experiments, and for assistance in the preperation of manuscripts: Moritz Wolf, Christoph Hartmann-Sauter, Ulrich Weber, Marco Donetti, Marco Durante, Timo Steinsberger and Athena Paz.

This project was made possible by funding support through the European Union's Horizon 2020 research and innovation programme under the Marie Sklodowska-Curie OMA grant. The research presented here is a result of a R&D project experiment SBIO at the beam line SIS-18 in the frame of FAIR Phase-0 supported by the GSI Helmholtzzentrum für

Schwerionenforschung GmbH, in Darmstadt (Germany), from the Charles E. Coates travel award (LSU), and from the August Family Professorship (LSU).

Finally, I would like to thank my friends and family. Their support and encouragement throughout my project helped me stay motivated and grounded throughout my studies. I am excited to enter the next chapter of my life as I enter the professional world.

Table of Contents

List of Tables

List of Figures

Abstract

Despite advancements in cancer therapy, certain indications continue to have a poor prognosis, including cancers of the thorax. Existing methods for treating moving tumors with carbon ions have shown promise, but require technologically complex facilities and still have inherent limitations to mitigating tumor motion. The goal of this dissertation was to develop and test a safe, portable and modular motion-synchronized dose delivery system (M-DDS) and its peripheral components as a framework for studying motion mitigation with ion beams.

We designed and integrated a motion-synchronized radiotherapy approach, called multi-phase 4D delivery (MP4D), as modular units of a clinical dose delivery system. The MP4D approach was integrated into a research facility and the facility was redesigned for developing and testing new cancer therapy technologies. We performed a comprehensive risk assessment for the M-DDS and validated the performance of the MP4D approach experimentally. Finally, we compared MP4D to other delivery strategies in terms of dosimetric quality and projected therapeutic outcomes.

The prototype system was implemented and characterized at GSI and CNAO. The functionality and performance was confirmed through a series of tests. Validations revealed that MP4D produces quantitatively superior dosimetric quality and projected therapeutic outcomes. Additionally, we determined that the MP4D dose delivery strategy compensated for heterogeneous anatomical motion with minimal dose distribution degradations. Our safety analysis revealed several risks that are unique to MP4D; appropriate solutions were implemented and tested.

The major findings of this study are that the MP4D approach delivered conformal, motion-synchronized beams with acceptable performance, dosimetric quality, safety and projected therapeutic outcomes. We demonstrated that MP4D may become a suitable strategy

for conformal, motion mitigation in clinical radiotherapy. The modular design of the M-DDS allows for integration into a variety of facilities, and the MP4D methods presented can be utilized at any ion therapy center that operates with a similar delivery system. The generalized and modular design of the M-DDS provides a framework for testing a variety of motion mitigation and other therapy approaches. This work, taken together, provides a comprehensive pre-clinical study on the modular, motion-synchronized dose delivery system for delivering conformal dose distributions to moving targets.

Chapter 1. Introduction

1.1. Background and Motivation

Cancer continues to be a major health care problem globally: 1 in 6 deaths worldwide are due to cancer alone [1]. In the United States, almost 1.8 million people were diagnosed with cancer in 2019 [2]. In the last 20 years, overall cancer survival rates have increased by over 10 %, as new treatment methods have expanded to wide scale use [3]. These methods include radiotherapy technologies, such as IMRT, image guidance, and active scanning ion therapy [4-6]. Ion therapy has proven to be advantageous in treating a wide array of tumor sites, including salvage radiotherapies that were considered incurable [7, 8]. Despite these successes, certain indications continue to have a poor prognosis, such as cancers of the thorax. For these cancers, including lung, liver and pancreatic cancer, the poor outcomes can be attributed, in part, to tumor motion during radiotherapy. Some promise has been shown for applying ion therapy to treating moving tumors [9], but assessing the efficacy of ion therapy methods has been slow due to the diversity of treatment methods, including fractionation schemes and accelerator types [10].

Research in developing new methods for therapy often does not successfully translate to new medical devices [11]. Barriers to implementation of new medical technologies into the clinic exist at several stages: development, safety testing, commercialization and clinical trials. In some cases, as many as 90 % of projects do not translate to human use. During development, technologies created without feedback from clinical experts may not adequately suit the needs of the clinic [12]. Additionally, without feedback on safety and regulatory requirements, developing technologies may require to be redesigned. Finally, the limited number of ion therapy testing and research facilities can make the efficacy of new

modalities hard to quantify, slowing down the process of verifying the safety of new devices, and commercializing the devices at multiple institutions.

In particular, large-scale scientific testing is limited by the diversity of ion therapy systems. Clinical trials are slow, and limited in their impact, as, in contrast to photon therapy, few ion therapy facilities exist. Further, exisitng facilities differ in accelerator types, treatment planning systems, fractionation schemes, delivery control systems and motion maanagement, making comparisons between clinics challenging. More harmonized systems, including similar delivery control systems at more centers and standardized treatment protocols, including at therapy research centers, would allow for performing pre-clinical research and clinical trials at multiple institutes, accelerating the transition of these technologies. So far, we do not have a portable, modular modality for development and preclinical testing of emerging technologies.

One pervasive issue that is yet to be solved due is mitigating tumor motion during treatment. The benefits of ion therapy cannot be fully exploited with current motion mitigation strategies, and new methods must be developed. Current approaches for motion handling rely on external components to control and direct delivery (*i.e.*, beam gating, abdominal compression or ITV based methods). One method has been to use beam gating to limit the amount of motion during active beam delivery. However, this strategy assumes no changes to the tumor motion motion, and requires larger dose volumes to account for delivery uncertainties. A more recent strategy is to use a combination of two common motion handling methods: phase-controlled rescanning and gating [13]. This approach utilizes fast delivery methods and image guidance to limit the extent of postion motion changes during active delivery, while repeating delivery of dose volumes multiple times to “blur out” the remaining inhomogeneities from residual tumor motion. More accurate delivery and smaller safety margins are possible with this approach; however, several limitations still remain,

including difficulty to adjust for changes in tumor motion patterns, long delivery times, and a dependence on accelerator capabilities, making them suboptimal solutions for most ion therapy facilities. Relatively less is known about the efficacy of delivery methods that synchronize beam delivery to the detected motion, such as beam tracking. Some studies have attempted to implement 3D beam tracking solutions [14-16]. So far, no clinically viable, adaptive motion tracking solution has been developed.

1.2. Statement of the Problem

We lack a framework for developing and testingcertain aspects of new radiotherapy modalities for solving persistent problems in cancer therapy, such as treating radioresistant and moving tumors. Further, we lack a dedicated facility for developing and testing the efficacy of a variety of motion mitigation approaches, such as a radiation research facility that contains the infrastructure for testing strategies in conditions similar to those in the clinic, to facilitiate translation into clincial use. Additionally, this necessitates developing programs for performing comprehensive risk analysis and safety testing to facilitiate translation into the clinic. Development of solutions for one such persistant problem, treating moving tumors, has been hindered by the slow progress in implementing new delivery strategies and integrating them into the clinic. No such facility is in existence, therefore, the feasibility of developing such a platform was unknown.

1.3. Objective

The goal of this dissertation was to develop and validate a safe, portable and modular dose delivery system and its peripheral components as a framework for research in novel ion therapy approaches for motion mitigation. We have achieved this by adapting a clinical ion therapy dose delivery system into the ion therapy research room at GSI (Cave M) and implementing motion-synchronization capabilities as modular units (Chapter 2). We then redesigned the research facility at GSI as a platform on which novel delivery methods can be

tested for clinical use, including comparing several motion mitigation solutions with light ion beams (Chapter 3). To do this, we updated the peripheral components and interfaces of beam nozzle components to the M-DDS. We then performed a comprehensive risk analysis to confirm the safety of our implementation of the motion-synchronized DDS (Chapter 4). This analysis allowed for identifying potential safety risks, implementing solutions and suggesting regular safety tests. This strategy can be applied and adapted to any clinical environment that is in the pre-clinical testing phases of adopting the M-DDS hardware and software. Finally, we validated that the M-DDS can mitigate for anatomical motion in heterogenous phantoms (Chapter 5), and demonstrated that the multi-phase 4D dose delivery approach can deliver 4D patient treatment plans with more favorable treatment quality and projected therapeutic outcomes compared to other motion compensation strategies with scanned carbon and proton ion beams (Chapter 6).

Chapter 2. A Modular Dose Delivery System for Treating Moving Targets with Scanned Ion Beams: Performance and Safety Characteristics, and Preliminary Tests

2.1. Introduction

Longstanding impediments to performing clinical trials on the efficacy of proton and heavier ion beam therapies include treatment systems that are technologically diverse. These impediments make it difficult to accrue sufficient numbers of patients in clinical trials to elucidate the role of ion beam therapy in oncology. Technological diversity of treatment systems may further introduce confounding factors that limit the power and utility of studies that are sensitive to details of the treatment techniques. A prominent open question pertains to the potential role of ion beams for treating moving tumors in the lung, a prevalent cancer with a poor prognosis for survival. In particular, contemporary ion beam centers utilize distinct and markedly different technical strategies to mitigate respiratory motion. These differences derive from a variety of factors, including the performance characteristics of beam delivery hardware systems, treatment planning systems, systems to monitor respiratory motion, and treatment control systems. Thus, to increase patient accrual rates and reduce confounding factors, modular technologies offer an attractive way to increase the similarity of treatments delivered by multiple institutions that use treatment systems of different designs. Additionally, a modular approach allows the majority of research and development of a prototype system to be performed in a research facility. It also facilitates translation of the prototype system from a research laboratory to a clinical facility for pre-clinical testing. In commercial systems, due to safety and regulatory considerations, the concepts and approach to modularity are typically implemented by device manufacturers in proprietary form,

---

This chapter was previously published as “Lis M et al. (2020) A modular dose delivery system for treating moving targets with scanned ion beams: Performance and safety characteristics, and preliminary tests Physica Medica 76 307-16”. Reprinted by permission of Elsevier.

complicating research on new functionalities. A more modular control system, developed within an open research platform with a direct link to the clinical environment, may overcome this limitation. For example, this would allow a variety of beam transport system conditions and motion mitigation strategies to be researched and evaluated at a single center, thus accelerating the translation of nascent motion management technologies to clinic implementation.

Many particle therapy centers have implemented motion handling techniques into clinical practice [17]. However, a majority of these techniques consist of auxiliary components for minimizing tumor motion during active beam delivery [18-21]. Comparatively few of these systems have motion mitigation techniques integrated into the dose delivery system design [22]. Additionally, though the feasibility of conformal treatments through beam tracking has been established at GSI Helmholtzzentrum für Schwerionenforschung GmbH [18, 23], pre-clinical testing revealed irreconcilable problems with the design [24]. To our knowledge, there is no charged-particle dose delivery system, which contains a designated motion synchronization unit integrated into the dose delivery system architecture. Thus, existing strategies cannot deliver conformal plans while dynamically adapting the delivery in real time to anatomic movement.

The objective of this study was to design, implement, and test a prototype of a modular motion-synchronized dose delivery system (M-DDS) which can mitigate against target motion. We implemented a modular system, developed from a CE labeled system, which functioned at two markedly different carbon beam centers. The dosimetric performance of the system was characterized with treatment planning calculations and measurements of dose distributions in moving phantoms. Safety was characterized through a series of errors verification tests.

2.2. Methods and Materials

2.2.1 Design of Modular Motion-synchronized Dose Delivery System

This section describes the system we have developed which synchronizes the delivery of scanned ion beam to tumor motion. The fast control portion of the dose delivery system (DDS) at the Centro Nazionale di Adroterapia Oncologica (CNAO) has been updated and adapted to the therapy research beam line at GSI. The fast control system monitors and guides the ion beams to deliver 3D dose volumes. The fast control system interfaces with peripheral components, including the interlock, scanning magnet, beam chopper, beam detector, accelerator control system and timing systems, as well as the treatment control room (LCR) [25], as seen in Figure 2.1. The fast control system hardware is comprised of FPGAs, which serve as the controls of each of these peripheral components, as seen in Figure 2.2. The DDS hardware and associated software have been updated and the memory handling functionalities have been repackaged into a single subunit in preparation for implementing motion mitigation functionalities. Finally, motion monitoring and mitigation capabilities were designed and integrated into the DDS. In the following sections, we describe the design and implementation of the modular motion-synchronized dose delivery system (M-DDS). Additionally, we provide illustrative examples of the performance of the M-DDS.

2.2.1.1. Modular Motion-Synchronized Dose Delivery System

The M-DDS is dedicated to all controls during treatment delivery. It is comprised of a peripheral component interconnect (PCI) eXtensions express (PXIe) crate (National Instruments, Austin, Texas, USA). The crate houses a controller (PXIe-8840 Quad Core controller) and nine PXIe field programmable gate array (FPGA) modules, as seen in Figure 2.2. The FPGA modules control each subsystem during treatment delivery through distinct tasks: the particle count readout and treatment progression is controlled through intFPGA; the beam spot position readout is controlled through pos1FPGA; the beam spot scanning is

controlled through the scanFPGA; the spill and treatment timing synchronization is controlled through timingFPGA; interfacing with the beam request system and creation of simulated timing events (for offline testing) is controlled through GSItimingFPGA; the treatment plan loading, storage and beam spot progression order is controlled and determined through memoFPGA; the safety functionalities and interlocks are controlled through interlockFPGA; the motion detection and motion phase discrimination is determined through motionFPGA. Each FPGA works as a standalone module for maximum speed, versatility, and reliability, as well as portability.

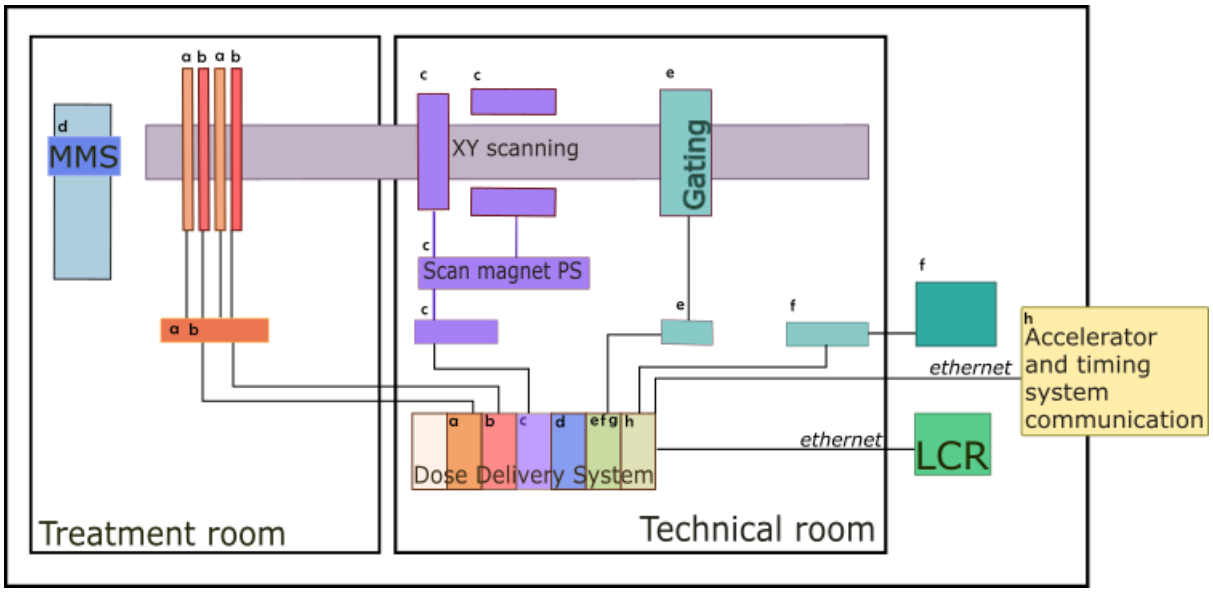

Figure 2.1. CNAO treatment control system layout and connections of the DDS to the treatment controls and accelerator. The intensity detection subunit is indicated in orange (a); the position detection subunit is indicated in red (b); the scanning magnet subunit is indicated in violet (c); the motion mitigation subunit is indicated in blue (d); the safety and monitoring subunits, are indicated in shades of green, including gating system (e) and interlock system which are indicated in teal (f) and the control room monitoring system (LCR) in bright green; the timing subunit is indicated in green-yellow (g), which connects to the accelerator communication system, indicated in yellow (h).

The FPGAs have been updated from the PXI-7813R FPGAs used at CNAO to PXIe-7821R FPGAs. The PXIe cards utilize a faster, backplane communication and synchronization, via a differential reference clock, and contain 512 MB of on-board memory. Output signals and connectors for each PXIe FPGA were modified to account for the reduction from 40 to 32 outputs per front connector. Additionally, memory loading protocols

in each FPGA were modified to direct memory access protocols (DMA), allowing for direct data exchange between the controller and each FPGA without heavy use of processing resources.

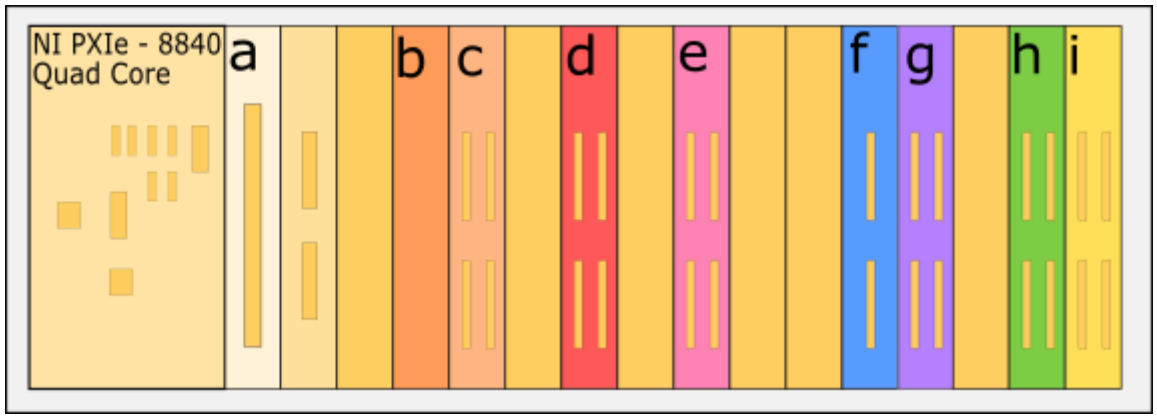

Figure 2.2. Schematic layout of the FPGA cards in the fast control system of the M-DDS. The fast control system is comprised of 9 PXIe FPGA cards, including the (a) interlockFPGA, (b) an ADC readout card, (c) intFPGA, (d) pos1FPGA, (e) memoFPGA, (f) motionFPGA, (g) scanFPGA, (h) timingFPGA, and (i) and optional GSItimingFPGA. Each FPGA card serves as a control unit for their associated DDS subsystem.

The fast control system has been integrated into the GSI therapy research beamline and installed into the CNAO research room. Both facilities are synchrotron based particle accelerators. Integration into the GSI environment was possible with the addition of a layer of interfaces and with minimal modifications to the fast control system software. Modifications included network communication with the beam request software and simulation of timing system events that are not used in the GSI DDS. Motion monitoring and mitigation capabilities were integrated into the fast control system as well.

2.2.1.2. Memory and Treatment Plan Handling

Modifications were made to the treatment plan handling protocols in preparation for motion mitigation functionalities. First, the treatment plan structure has been changed from a single plan to a library of sub-plans which contain motion compensation. Plan libraries were created using the research treatment planning system at GSI, TRiP4D [26]. TRiP4D is an

extension of TRiP98 [27, 28] that considers temporal changes to patient anatomy during treatment plan creation. During treatment planning, conformal 4D-optimization is utilized to create a library of treatment plans. Each plan in the library is a separate 3D optimization, planned [29] on a geometrical PTV, created on the tumor volume found in each motion phase from the 4DCT. The 3D optimization is a cost function that minimizes the difference between prescription and planned dose for each beam spot. The particle intensities of every beam spot in each plan is then scaled down, weighted by the length of the motion phase [30], so that the total dose of the entire plan library is the prescription dose. The library of plans was then converted to a modified version of the CNAO treatment plan format that includes motion phase information for each beam spot. Additionally, each slice in each plan was padded to be the same size.

Second, four memory modules (NI PXI 6534 FPGAs), each designated to store delivery information for one iso-energy slice (IES), were replaced with one memoFPGA, designated to loading and storing the entire treatment plan before delivery begins. Before treatment, the plans are sent via a TCP-IP connection to the M-DDS and converted to synchrotron beam parameter codes for each IES (containing information on beam spot FWHM, energy, particle, particle rate) and FPGA IES files (SLD files), which are grids of raster points that are to be irradiated sequentially. The entire array of SLD files is then loaded onto the memoFPGA dynamic random access memory (DRAM) at the beginning of treatment. This allows for sending beam spots both sequentially and out of order to the other FPGAs without increases in spot switching time. Additionally, minimum IES switching time was reduced to 100 ms, allowing for the possibility of using the DDS with a cyclotron. The memoFPGA receives motion phase information from the motionFPGA, and has a central role in motion mitigation, as described below.

During treatment, the memoFPGA sends delivery information, spot by spot, to the other FPGAs. Additionally, delivery data is logged in two binary files: dose delivery data (DDD) files and motion mitigation data (MMD) files. Delivery data from the beamline detectors and scanning system is written into a new DDD file at the completion of delivering the IES, whereas previously, this data was written out into a new DDD file during each spill pause. In parallel, the MMS writes motion information every 50 ms and for each spot during delivery. At the conclusion of treatment, the motion signal, timing information, and motion phases are written into an MMD file.

2.2.1.3. Motion Mitigation Upgrades

The motion mitigation system (MMS) is an independent, optional component of the DDS that contains all functionalities for adapting the treatment delivery to the tumor motion. The flexibility of the MMS allows for adapting several motion mitigation strategies. The MMS is comprised of the motionFPGA (a NI PXIe-7857R FPGA), a motion detection device, the gating system and a portion of the memoFPGA. The MMS determines the real-time respiratory motion phase from the detected analog motion signal and controls treatment delivery sequence and progression. Existing treatment synchronization signals are used to synchronize the motion mitigation actions with the treatment delivery.

Upon plan loading, the number of motion phases and mitigation method are extracted from the treatment plan, and the MMS is set accordingly. Both amplitude-based and phase-based motion phase discrimination are available. The amplitude-based method involves discrimination of motion phases into fractions of the total detected motion amplitude, while the phase-based method discriminates motion phases into fractions of the total detected respiratory cycle duration. A ‘threshold gating’ mode is also available, where the delivery of beam spots is interrupted when detected respiratory motion is outside of a specified tumor position window. An analog motion amplitude signal is continuously acquired at 1000 Hz

and averaged to 50 ms for noise reduction. After the treatment plan is loaded and during a stable motion cycle, the motion signal is calibrated to the detected motion amplitude. For the phase-based method, the duration of a motion cycle is also measured. The motion phases are subsequently delineated. Additionally, lateral beam spot coordinates can be sent to the memoFPGA to make adjustments to the beam spot position for position corrections or for the beam tracking motion compensation strategy. During treatment, the motion phase is sent to the memoFPGA to redirect treatment progression.

The general motion-synchronized delivery concept implemented here was described by Graeff *et al.* [31] and modified to enhance the treatment-progression logic. Here, the motion phase is continuously sent from the motionFPGA to the memoFPGA. The beam spots within the plan corresponding to the identified motion phase are delivered sequentially until a motion phase change occurs. When the motion phase changes, the delivery is directed to the plan within the plan library corresponding to the new motion phase. The distribution of motion phases is represented in Figure 2.3. The beam spot that is closest to the current beam position is selected and the spot delivery progresses in sequence until a different motion phase is detected and the delivery is redirected again (Figure 2.4). Each delivered spot is masked and when the delivery is returned back to a partially delivered plan, the masked spots are skipped. For completely delivered sub-plan slices, the beam is gated until a new motion phase is detected. When the number of delivered spots matches the number of spots within the plan library for the current IES, the delivery progresses to the next IES. The same system also delivered static treatments, i.e., which were 4-D plans with only one motion phase. In the DDS, the motion phase was set to one, and, by default, the beam spots were delivered in their as-planned sequence. For testing purposes, an uncompensated delivery mode is available, where a static (one phase) plan is delivered to a moving target.

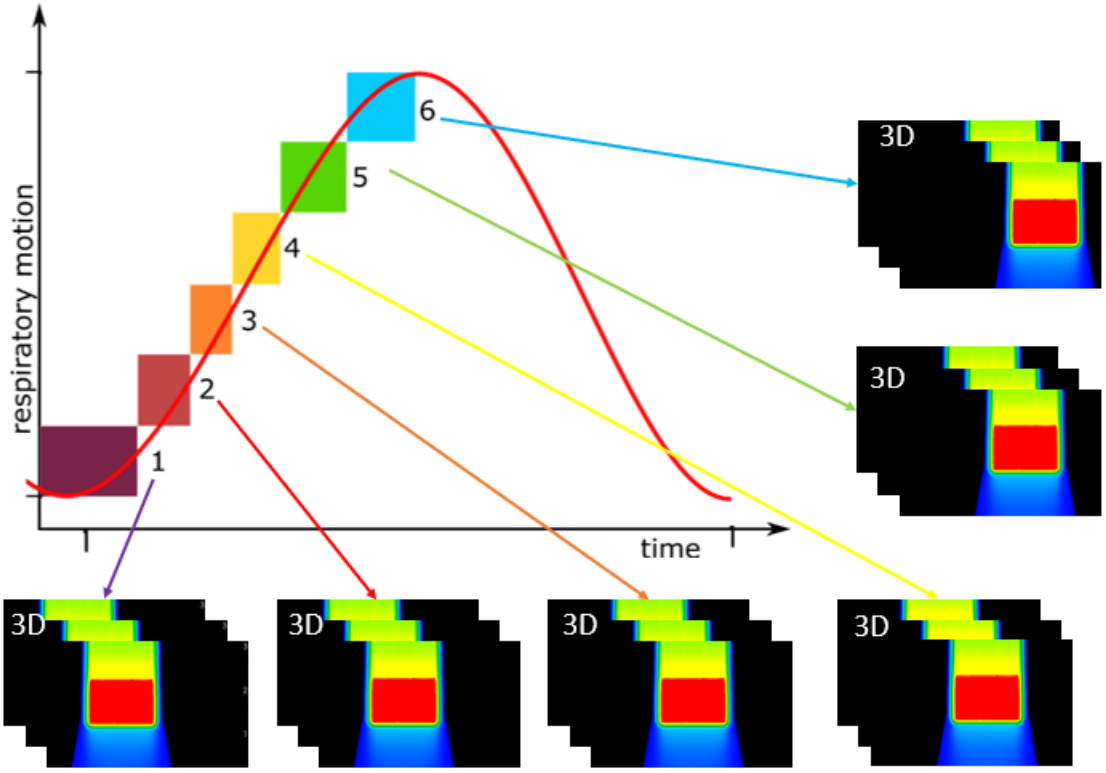

Figure 2.3. A schematic depiction of the treatment plan library for an amplitude-based motion. Each individual plan is optimized on the motion phase-specific PTV, in an independent 3D-optimization. The beam spots in all of those plans are then scaled down, such that their total dose is the prescription dose.

The MMS is structured as a state machine, running independently and in parallel with the main DDS. The transition between states is synchronized with DDS loading, treatment plan sending, treatment delivery and recording of delivery data, but the MMS remains independent from the DDS. At the completion of a treatment, the motion data, including the motion amplitude, phase beam spot count and timing information, is written into a motion mitigation data file (MMD), and the MMS transitions back to an idling state until the next treatment begins or until the MMS is signaled to shut down.

Additional gating capabilities were implemented for motion mitigation. This includes triggering delivery interruption under unexpected motion behaviour such as lateral shifts that are out of the amplitude range determined during calibration or sudden loss of motion signal. Rapid gating was also utilized in partially or fully delivered sub-plans and when ‘jumping’ to

the next undelivered beam spot. When gating, each FPGA enters and 'idling' state, where no beam spot information is sent and treatment information is logged every 50 ms. The gating functionalities have been experimentally verified at GSI and CNAO.

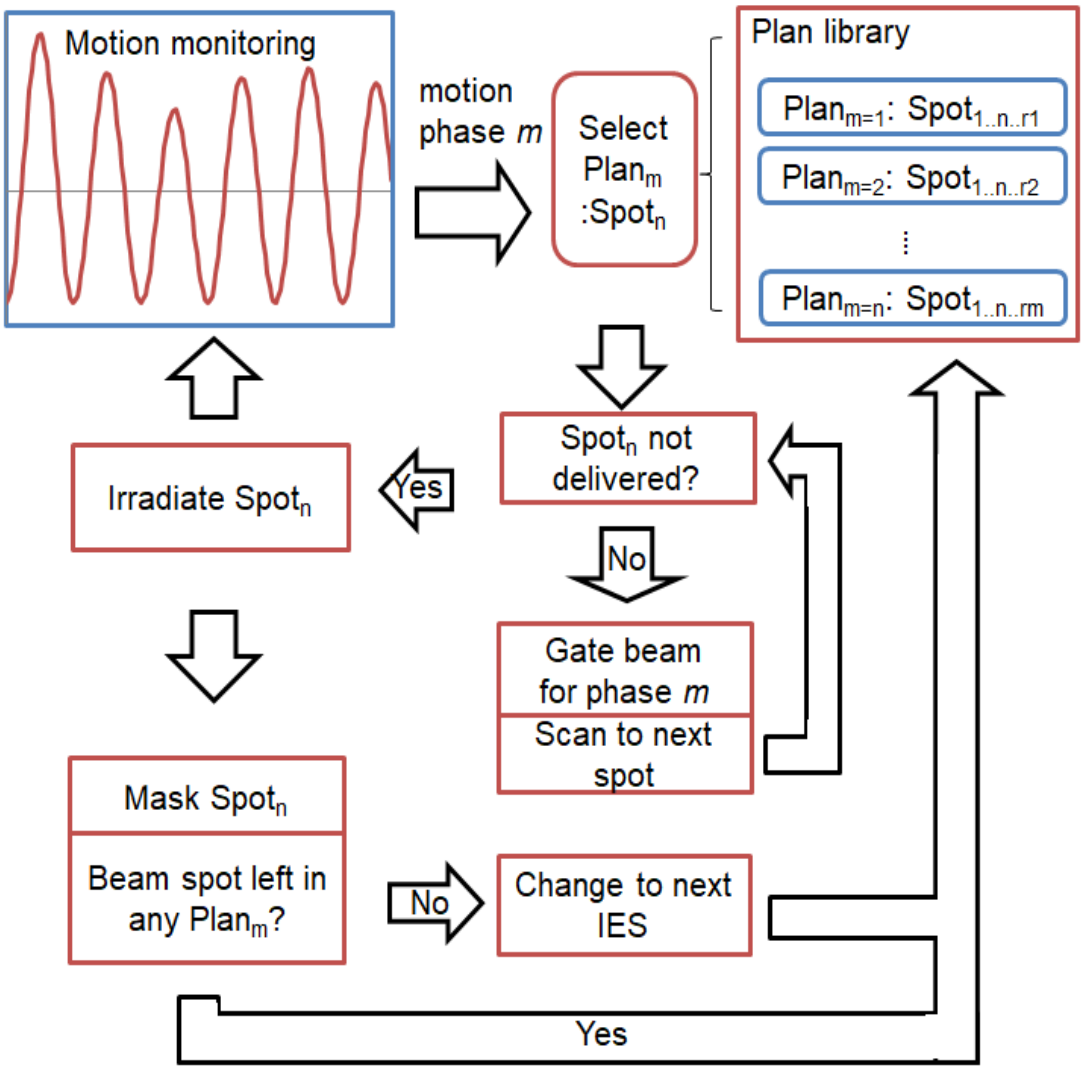

Figure 2.4. MMS logic schematic. The motion information directs selection of the plan from the library. Beam spots in the library are delivered in sequence until a different motion phase is detected and the delivery is redirected to another plan in the library. Delivered spots are masked and the delivery is gated when directed to a delivered portion of the slice. The plan progresses to the next energy layer when the number of delivered spots matches the number of spots within the plan library for the current IES.

2.2.2 M-DDS Verification Tests

The modularity and the functionality of the motion mitigation system was characterized and verified for functionality and performance through a series of offline (without beam) and online tests at CNAO. The purpose of these tests was to determine the feasibility of using the implemented M-DDS for 4D therapy in future clinical systems.

Offline and online tests were performed during several stages of development to test the functionality of the motion mitigation system. Specifically, we tested motion detection, motion phase transmission to the memoFPGA and motion-related gating. Experiments were performed by delivering simple spot patterns to radiochromic film (Gafchromic EBT3 ISP, Wayne, New Jersey, USA) (Table 2.1). Additionally, the capability to progress through multiple IES was verified online by delivering treatment plans with vertical lines each in separate IES for each motion phase. In addition to these verification tests, the motion mitigation capabilities were also studied experimentally.

Simple 2D and 3D geometries, such as squares and cubes, were designed for static deliveries and for 3, 6 and 10 amplitude-based motion phases. 2D plans were generated from a script, while 3D geometries were created with TRiP4D. The plan libraries were designed with 4D-optimization to target volumes [32, 33] which results in a conformal treatment plan for each motion phase. The degree to which the M-DDS can compensate for motion was investigated by delivering 2D geometries to single films and to the ionization chamber array detector behind 2 cm of water-equivalent (TE) plastic (RW3, LAP GmbH, Lüneburg, Germany) and 3D geometries behind 10 cm water-equivalent plastic to measure a 2D cross section through the center of each delivered volume.

Table 2.1. Summary of offline and online verification tests and relevant analysis tools for verifying implemented motion mitigation system functionalities.

Offline functionality tests		
Subunit	**Test**	**Analysis tool**
Motion mitigation system	Connection with moving platform	Observation of sinusoidal motion signal from OD laser in MMS
	Detection of motion	Observation of motion phases in fast control
	Sending of motion phases	Receiving phases in log files
Treatment plan handling	Loads entire plan libraries	SLD file analysis
	Sends single spots	DDD file analysis
	Sub-plan switching from motion phase changes	DDD file analysis
Online subunit tests: Delivery of ‘6 lines, each in 6 slices’ treatment plan		
Motion mitigation system	Motion phase changes	DDD file analysis
	Motion mitigation	Film analysis
	Gating related to motion handling	Film and log file analysis
Treatment plan handling	Plan loading	Plan accepted into DDS
	Non-sequential delivery	

2.2.2.1. Data Analysis

The quality of the delivered doses was assessed through gamma index analysis, homogeneity index and conformity number.

First, dose reconstructions were performed in order to compare the planned and delivered dose distributions. In order to do this, the ionization chamber array detector readout data was correlated with the delivered beamline detector data from DDD log files by matching the 100 ms frames of the ionization chamber array detector to the timestamps of the

delivery data. The correlated DDD data was converted to the TRiP4D treatment file format and the doses were reconstructed from these created treatment files. Reconstructed data was compared with the original treatment plans using an in-house developed tool to compute the gamma index [34] with a 3 %/ 3 mm criteria. Pass rates of > 90 % were considered acceptable.

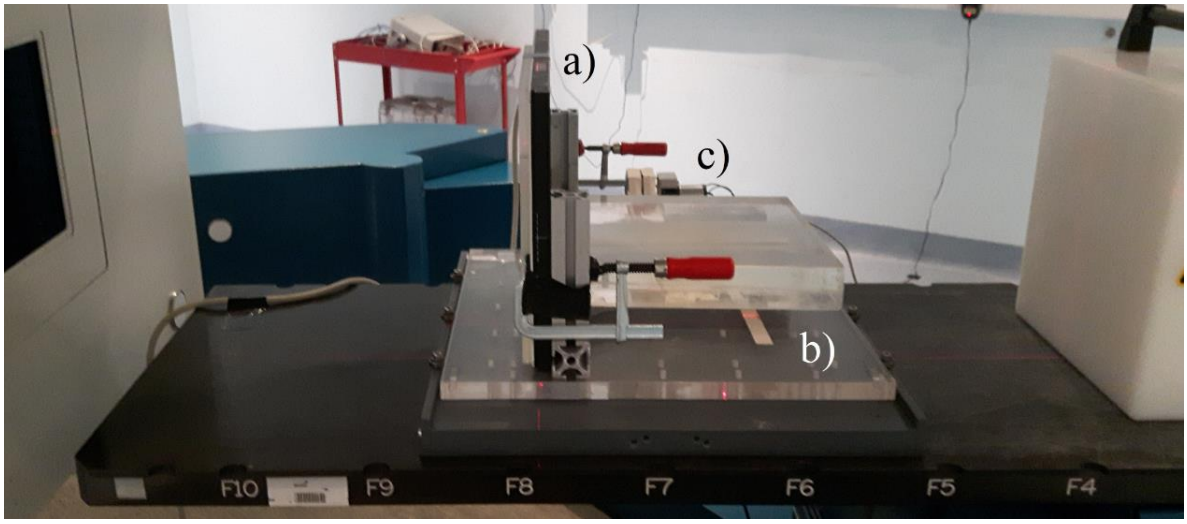

Figure 2.5. Experimental set-up used during measurements of dose distributions at CNAO. A a) 2-dimensional array of ionization chamber detectors is seen here, mounted vertically on top of b) a platform exhibiting 1-dimensional periodic motion. The motion is monitored with c) an optical distance sensor.

Second, radiochromic films were assessed to determine homogeneity index. All irradiated films were scanned in landscape orientation with a scanning digitizer (DosimetryPro, VIDAR System Corporation, Herndon, VA, USA) using 16 bit sampling and 300 dpi resolution. Calibration films were acquired at the beginning of each measurement period for eight particle fluences, from 2×10^5 to 4×10^7 particles/mm. Calibration curves were acquired from the calibration films and applied to all films using image analysis software (ImageJ version 1.52a, National Institute of Health, Bethesda, MD, USA). The homogeneity of the film deliveries was evaluated by measuring the dose distribution flatness within 70 % of the field size, using the equation $HI = 100 \times (D_{max} - D_{min})/(D_{max} + D_{min})$, where D_{min} and D_{max} are the minimum and maximum doses, respectively [35]. The dose

distribution homogeneity was assessed in 60 x 60 mm^2 uniform squares, delivered with 238.63 MeV/u carbon ions. HI of > 90 % were considered to have acceptable homogeneity.

Finally, the conformity of the homogeneous squares to the target area was assessed with the conformity number (CN), as described by van't Riet *et al* [36]. The CN was calculated from data for static and compensated measurements with the ionization chamber array detector. CN of > 60 % were considered conformal.

2.2.3 Critical Safety Testing

We performed critical safety tests at GSI and CNAO to verify that the motion mitigation strategy does not introduce safety risks to the DDS. Failure mode and effects analysis (FMEA) was performed to determine the highest risk safety errors [37]. Errors with a Risk Priority Number (RPN) above 100 were considered most critical. These high-risk errors included the failure to disrupt the beam during treatment errors and improper treatment verification. Potential causes of each error were identified through a fault tree analysis [37].

Treatment plan verification processes were altered with permanent corrective actions to prevent user errors, such as setting incorrect motion conditions, from occurring. Treatment plan verification was also tested for incorrect file format. Treatment plans that contained errors in formatting were loaded onto the DDS. For each error scenario, the DDS was expected to transition into a 'Setup Error' state upon plan loading, disabling progression to treatment.

Additionally, beam disruption error scenarios were investigated. First, delivery disruption triggered by loss of the motion amplitude signal was tested. For this test, a virtual switch was used to disable receiving motion phase signals from the motion detection unit in the MMS. The time delay in treatment interruption was measured and error recognition was confirmed. Phase shifts and changes in motion period are inherently handled by the M-DDS,

so only beam disruption when motion amplitude goes out of the expected range was tested. For this test, the motion amplitude was increased after the amplitude calibration was performed. The gating behaviour, when outside of the expected amplitude bounds, was then assessed.

2.3. Results

2.3.1 Results for Modular Motion-synchronized Dose Delivery System Design

The hardware and software design and motion mitigation functionalities were integrated into the M-DDS found at the GSI experimental therapy line and the CNAO research room according to the tests described in section 2.2. Memory and motion mitigation systems were confirmed to run as independent modules. A layer of interfaces between the FPGAs and peripheral components was developed that achieved interoperability with the system at CNAO. Interoperability and functionality with two extraction types were confirmed through experiments with the same dose delivery system at both GSI and CNAO. Following integration, the M-DDS performance was characterized.

2.3.2 Results for Motion-synchronized Dose Delivery System Performance Verification

2.3.2.1. Motion Mitigation System Verification Tests

The functionality of the motion mitigation was characterized in a series of offline and online signal transmission tests at CNAO and GSI. The MMS components of the M-DDS functioned at both centers without modification. The MMS was confirmed to measure motion amplitude, discriminate motion phases, and send motion phases for directing treatment delivery. The M-DDS was also confirmed to signal delivery interruption due to out-of-range motion. In addition to sub-system testing, separate integration tests were performed.

2.3.2.2. Integration Testing

The M-DDS delivered treatment plan libraries to moving and non-moving targets at both CNAO and GSI without modification, confirming the portability of the M-DDS between these centers. The FPGA for handling treatment plans (memoFPGA) was confirmed to properly handle up to 1 million beam spot plans of up to 300 IES per plan. The plan library format was accepted into the treatment control room at CNAO and loaded without error. MMD files were created and stored for all plans. DDD file analysis confirmed the functionality of the M-DDS, with and without the optional motion mitigation unit. No compromise to performance or significant increases in CPU consumption have been observed. Delivery efficiency was analyzed by assessing the beam spot progression efficiency for motion compensated plans compared to uncompensated plans (Figure 2.6). Duty cycles relative to static plans were determined to be between 80-95 % for all plans and total increases to treatment time were a factor 1.29 – 1.61 larger than for the static deliveries of squares, cubes and ellipses. Following integration testing, delivered dose quality was assessed.

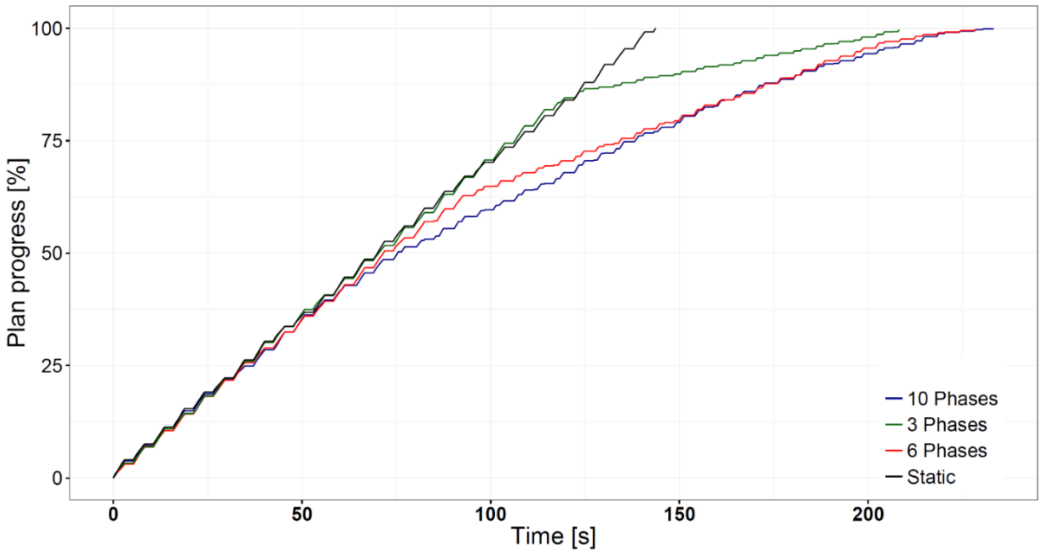

Figure 2.6. A comparison of particle counts delivered through time (s) for the delivery of an uncompensated static square, and 3, 6 and 10 motion phase compensation squares with dimensions of 60 x 60 mm^2. Plateaus in particle counts indicate spill pauses and delivered motion phases.

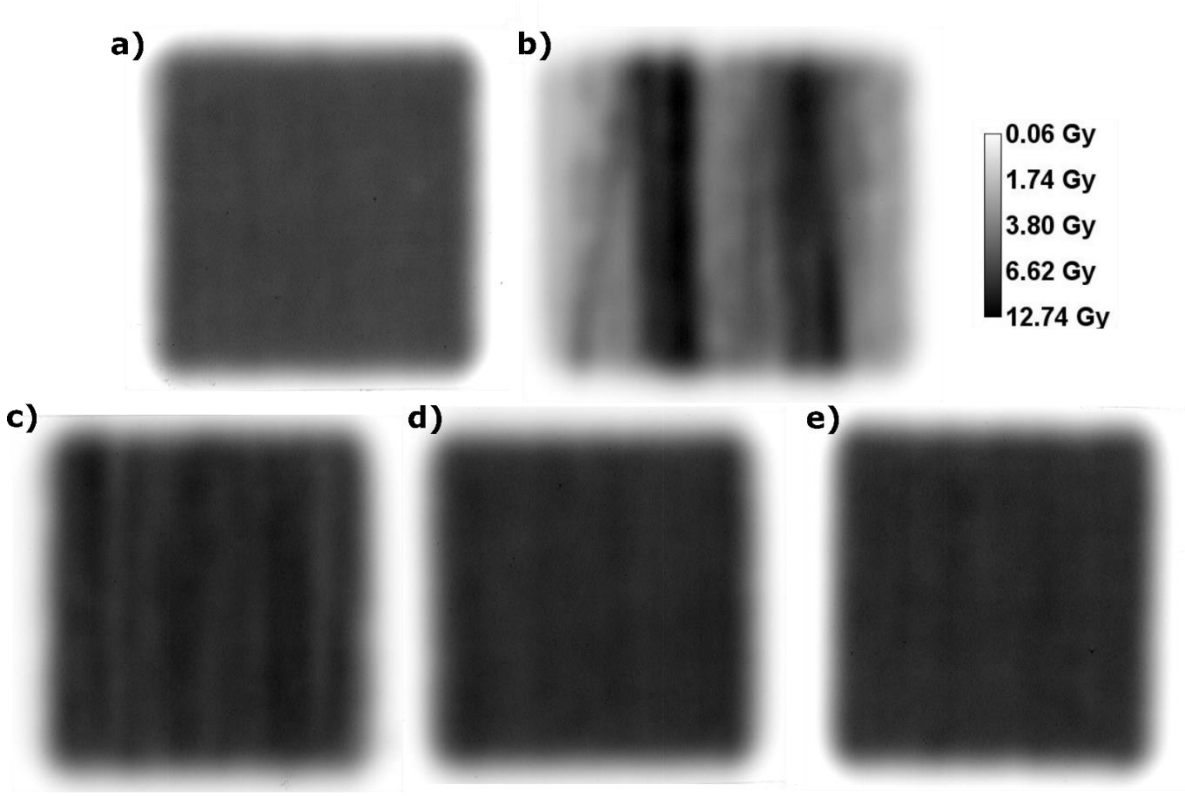

Figure 2.7. Cross-sections of dose distributions measured with EBT3 Gafchromic films at 10 cm depth for 60 x 60 x 60 mm^3 cubes delivered with 20 mm amplitude 1D motion, for a) static deliveries, b) uncompensated deliveries, c) 3 phase, d) 6 phase and e) 10 phase motion compensated deliveries.

2.3.2.3. Online Motion Compensation Tests

We assessed the extent of motion compensation by assessing the delivered dose quality for motion synchronized deliveries. The homogeneity of the motion compensated 60 x 60 mm^2 squares and 60 x 60 x 40 mm^3 cubes was calculated with EBT3 films using the homogeneity index. The HI was > 95 % for 6 and 10 motion phase squares delivered with 238.63 MeV/u carbon ions. The HI for 10 motion phase cubes was 95.2 % and the HI was 98.1 % for static cubes. HI, gamma index analysis and CN results are summarized in Table 2.2. For both the 60 x 60 mm^2 squares and 60 x 60 x 40 mm^3 cubes, the gamma index analysis resulted in pass rates of > 90 % for both 6 and 10 motion phase compensation. The dose distributions for static, uncompensated, 3 phase, 6 phase and 10 phase square profiles can also be seen in Figure 2.7. The CN indicated a high level of conformity for 6 and 10

motion phase plans. Low detector numbers in the IC detector array resulted in particularly high CNs for the cube deliveries. A comparison of measured IC detector array doses and planned doses for static, uncompensated, 3 phase and 6 phase compensation can be seen in Figure 2.8. In addition to assessing the degree of motion compensation, the functionality of critical safety features was also confirmed.

Table 2.2. Summary of gamma index pass rates, CN and HI from 3D and 4D treatments, delivered to simple phantoms. The gamma index analysis compared planned dose distributions to delivered doses with a criterion of 3 % / 3 mm. The HI measured particle fluence homogeneity within 70 % of the area of the delivered profiles on radiochromic films. The CN was calculated from the IC array detector. The gamma index analysis, CN, and HI were performed on 238.63 MeV/u 60 x 60 mm^2 squares at 20 mm amplitude of horizontal motion behind 2 cm of PMMA, and for 60 x 60 x 40 mm^3 cubes behind 10 cm of water equivalent plastic (RW3).

60 × 60 mm^2 square 238.63 MeV/u behind 2 cm RW3			
	Gamma pass rate	Conformity number	Homogeneity index
Static	100.0%	67.1%	95.1%
Uncompensated	44.0%	4.0%	47.6%
3 phase	80.0%	57.3%	88.5%
6 phase	94.0%	68.3%	95.8%
10 phase	96.0%	62.7%	97.5%
60 × 60 × 40 mm^3 cube behind 10 cm RW3			
Static	98.6%	98.8%	98.1%
Uncompensated	43.1%	24.7%	43.1%
3 phase	75.0%	49.6%	90.9%
6 phase	96.3%	85.2%	96.0%
10 phase	99%	100%	95.2%

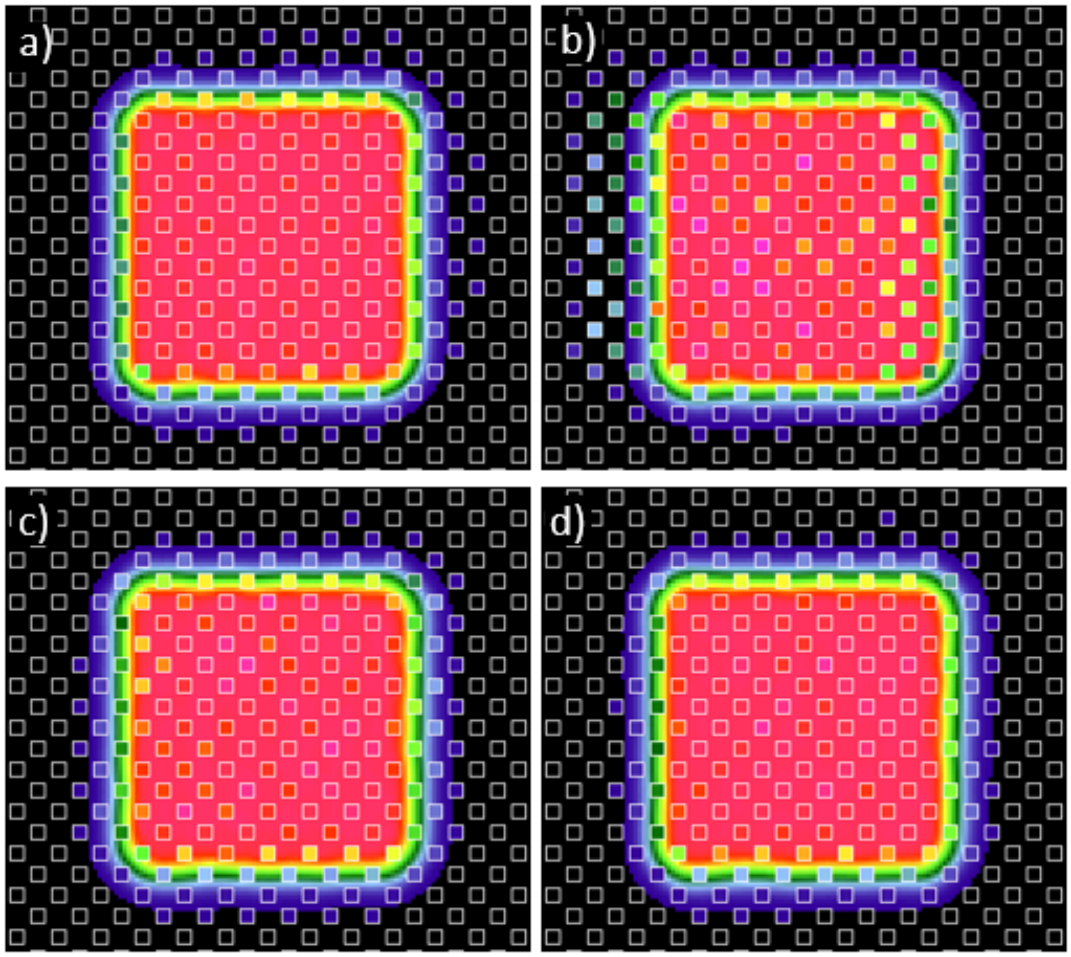

Figure 2.8. Cross-sections of dose distributions measured with the PTW Octavius IC array detector for 60 × 60 × 60 mm^3 cubes, delivered with a 20 mm amplitude of 1D motion (here represented in the squares) compared to planned dose distributions for a) static deliveries, b) uncompensated deliveries, c) 3 phases and d) 6 phases of motion compensation deliveries.

2.3.3 Initial Safety Assessment

We performed safety tests for high-risk safety errors at GSI and CNAO. Results of the safety tests are summarized in Table 2.3. During treatment plan verification error tests, the DDS identified the plan format errors and transitioned into a ‘Setup Error’ state, disabling progression to treatment.

Additionally, safety errors due to failure to disrupt beam delivery during treatment were also tested. A virtual switch, which manually disables receiving motion phase signals from the motion sensor in the MMS, was used, and the treatment plan progression was

interrupted. Beam disruption from movement outside of the expected amplitude bounds was automatically triggered from the MMS.

Table 2.3. Summary of critical safety tests performed at CNAO and the DDS response to the error conditions. These tests confirmed the safety of the motion mitigation additions to the dose delivery system.

Safety Test Description	**DDS response to error condition**
Idling during gating	No beam spots sent
Beam gate from out of range motion	Sets gate
Manual beam gate from MMS	Sets gate
Match motion phase in plan and MMS	Matched automatically from treatment plan
Phase or amp. based motion incorrect	Matched automatically from treatment plan
Load corrupt treatment file	Goes to error state
Motion not being monitored	Delivery gates until motion signal acquired
Baseline drift detection	Sets gate when out of amplitude range
Incomplete slice delivered	Aborts and stops treat

2.4. Discussion

We developed a modular motion-synchronized dose delivery system (M-DDS) for delivering motion mitigated ion-beam treatments with the raster scanning technique. Specifically, we developed the M-DDS, as an extension of the DDS, which is in clinical use at CNAO for static treatments. The major finding of this study is that the M-DDS demonstrated acceptable dosimetric performance and portability between two ion therapy centers, GSI and CNAO.

The implication of this finding is that the fast control portion of the M-DDS is a portable and modular design, which could be utilized at multiple centers with a similar treatment control system. This, in turn, could facilitate future research on motion mitigation, including sharing of technical methods and pooling of data from multi-institution clinical

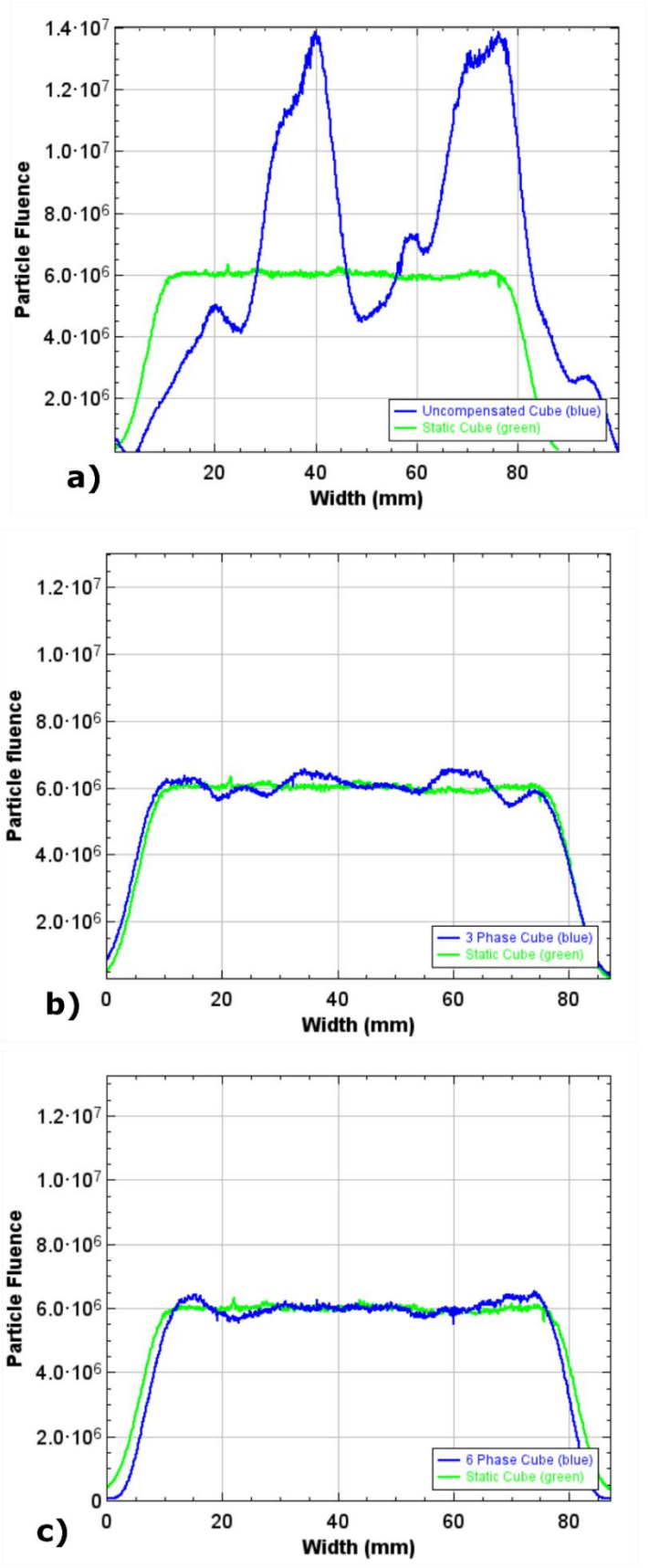

Figure 2.9. Homogeneity profiles comparing 60 × 60 mm^2 a static cube (green) delivery to a) an uncompensated cube delivery, b) 3 motion phase delivery, and c) 6 motion phase delivery.

trials. The presented design is not a singular solution to motion mitigation, but can be used in conjunction with other mitigation strategies, such as beam tracking or rescanning, to provide a more comprehensive solution to conformal lung cancer therapy. With further study, this design can be expanded to include real-time corrective beam tumor tracking with optical motion sensors [24].

This is the first implementation of a dose delivery system for conformal, motion-synchronized delivery of scanned ion beam plans. The results of this study are coherent with previous works in developing motion-synchronized dose delivery at GSI and comparable to the system at the National Institute of Radiological Science (NIRS) [31, 38]. At GSI, sectored target delivery and multi-gating with tumor tracking were employed to motion-synchronized conformal deliveries [31, 39]. In these studies, single IES plans could be delivered with gamma index analysis results from 79.6 % to 94.6 % compared to static delivery. For a similar experiment in this study, gamma index analysis resulted in 96.0% pass rates. In all cases, a criteria of 3% / 3mm was used. The implementation of the motion mitigation strategies was spread throughout the entire treatment control system, resulted in timing and delivery complications and was not deemed a clinically viable solution. At NIRS, phase-controlled rescanning is utilized to adapt the rescanning duration to the gating duration [13]. This strategy is combined with online tumor location measurements via x-ray fluoroscopy, resulting in homogeneous irradiations [38]. The NIRS strategy uses a single motion state, larger beam-gating window and utilizes motion-synchronization only for more effective rescanning of statically planned (3D) treatments. Thus, because the present approach considers multiple motion states, in theory it can provide superior dosimetric performance.

Our study has several notable strengths. A key strength is that the FPGA hardware and software structure is commercially available, and is based on a clinically certified (LabVIEW) software. The use of commercial products allows for hardware and software

updates and maintenance with replacement of standard parts. Additionally, the architecture of the M-DDS is highly modular and expandable, which allows for straightforward implementation of additional motion mitigation capabilities: all motion mitigation capabilities will continue to be contained within the motionFPGA to maintain a modular design.

An additional strength of this study is that we validated our work experimentally using a scanned carbon ion beam, a moving phantom and several detectors, including a time-resolved ionization chamber array detector and films. Our experimental results have indicated that the M-DDS can deliver conformal treatments by synchronizing real-time tumor motion to the ion beam scan path. Effective motion compensation was possible with 6 motion phase plans for an amplitude of 20 mm. Gamma index analysis revealed acceptable dose distributions for 6 and 10 phase geometries which had > 90 % pass rates. Similarly, the CN were within clinically acceptable standards of > 60% for 6 and 10 phase plans and the HI produced similar homogeneity for static and 10 phase deliveries. Further, the safety of the motion mitigation additions to the DDS were confirmed through critical safety tests. Results of verification tests have indicated that the proposed motion synchronized treatment strategy can deliver treatments to clinically acceptable accuracy.

A final strength of this study was that 3D dose distribution data was collected with radiochromic film stacks and the ionization chamber array. The films exhibited quenching which is typical for carbon ions and, therefore, could be compensated for during analysis. Additionally, though the longitudinal film spacing reduced resolution to 1 cm in depth, the direction of motion was in the horizontal lateral direction, so distribution with depth were less critical for this study and 1 cm resolution was deemed acceptable. In further studies, higher resolution 3D dose distributions could be acquired with a 3D dosimetry system.

One limitation of our study is that the current method assumes that respiration patterns and tumor position do not differ significantly from those seen during 4DCT scans used for creating treatment plans. Deviations from expected tumor locations are to be expected and must be compensated by an enlarged treatment field, counteracting the desired conformity [40]. In further studies, deviations from expected tumor motion will be studied and appropriate compensation, including corrective tracking, will be introduced [41]. The updated M-DDS and continued collaboration with CNAO will allow for integration of further motion mitigation into the M-DDS and, eventually, integration of the M-DDS into the clinic.

Another limitation was that a comparatively simple experimental setup, with only one-dimensional regular motion patterns was used. In further studies, more complex experiments will include irregular, 3D breathing traces. More precise, 3D dose measurements will be acquired using a 3D dosimetry system with a higher resolution IC detector array or with gel dosimeters [42]. Finally, compensation for tissue heterogeneities have not been considered yet and the delivery results in lung and bone equivalent materials has, therefore not been determined. Studies are under-way at GSI and CNAO to address additional layers of complexity in respiratory motion mitigation, such as baseline drifts, irregular motion and position corrections. Additionally, the DDS will be assessed for motion compensation through heterogeneous density phantoms and through multiple depths. Additional motion handling techniques will be implemented into the DDS and compared.

2.5. Conclusions

We developed a motion-synchronized dose delivery system for scanned ion beam radiotherapy. This work has demonstrated that it is possible to deliver conformal, motion compensated dose distributions to moving targets. The M-DDS provides dose distributions of > 90 % gamma index pass rates. Importantly, the M-DDS provides a solution for motion

mitigation studies at both a research and a clinical center, providing the possibility for testing a broad variety of motion mitigation strategies while maintaining clinical safety standards.

Chapter 3. A Facility for the Research, Development, and Translation of Advanced Technologies for Ion-beam Therapies

3.1. Introduction

External-beam radiation therapy is a safe and non-invasive treatment for a wide variety of malignant diseases. The objective is to sterilize the tumor while sparing surrounding healthy tissue. Most treatments utilize photon beams, yet beams of protons and heavier charged particles are of increasing interest to treat radiation resistant tumors and in sites where radiation damage to healthy tissues is of concern [43-45]. Synchrotrons and cyclotrons produce narrow ion beams that are magnetically scanned laterally and modulated in penetration range to deliver highly conformal dose distributions [46, 47]. Research with ion beams for therapy includes advanced technologies, such as Flash [48], radioactive ion beams (RIB) [49], mixed species of ion beams [50], and advanced motion mitigation strategies [14, 51]. Most research on these technologies have higher technical demands than those of conventional ion therapy treatments, and, in some cases, go beyond the capabilities of current medical accelerators. Therefore, research on these topics is commonly conducted at dedicated accelerator research laboratories that can provide dedicated beamtime for experiments, specialized technical support teams, and the possibility to modify beamlines and safety systems. Typically, this type of research is more difficult, or even impossible, to conduct at a clinical facility that is mainly utilized to treat patients. Currently, the pace of progress of research is constrained by the scarcity of accelerator research facilities, as well as limitations in their capabilities and capacities to support certain research activities.

Currently, there are 92 proton therapy centers and 14 heavy ion therapy centers

---

This chapter was previously published as “Lis M, Newhauser W, Donetti M, Durante M, Weber U, Zipfel B, Hartmann-Sauter C, Wolf M and Graeff C 2021 A facility for the research, development, and translation of advanced technologies for ion-beam therapies Journal of Instrumentation 16 T03004.” Reprinted with permission of IOP Publishing.

worldwide [52], with only a few capable of supporting research that relies on the delivery ofbeams with characteristics that are radically different from those currently used in clinical practice. Thus, beams with potentially paradigm-shifting characteristics are scarce, which constitutes a gap in the needed research infrastructure. For these reasons, as well as the difficulty of translating new treatment paradigms to clinical practice, it is imperative to have research facilities that support research, development, and clinical translation efficiently. Ideally, such facilities can mimic the characteristics of current clinical treatment systems [53], but also offers enhanced characteristics, additional capabilities for experimentation, and allows for rapid system modifications. In practice, several facilities approach this ideal [54-58]. One of these, the radiotherapy research facility at GSI (frequently denoted as Cave M), is the focus of this report. Construction of a predecessor therapy beamline was completed in 1996 [59]. In 2008, after the successful technology transfer and commercialization of the GSI therapy systems, patient treatments at GSI ceased and were resumed at a replacement facility in Heidelberg [58]. Currently, GSI is modernizing and upgrading several of its research facilities within the Facility for Antiproton and Ion Research (FAIR) [60, 61] project. This includes significant upgrades of the SIS-18 synchrotron, including increased beam intensity, faster ramping and improved beam extraction. The modernization of Cave M [46, 62], which began in 2016 and is ongoing, is reported for the first time in this manuscript. The facility opened in 2020 for users within the Biophysics Programme Advisory Committee (BioPAC) and the European Space Agency (ESA).

The objective of this work is to describe the general design, features, and selected preliminary performance characteristics of the modernized Cave M. This includes beam monitoring and delivery systems, peripheral components of the beam delivery system, and corresponding software to facilitate research, testing, and translation of new devices and technologies. We provide readers with an update on the performance specifications and

general characteristics of the beamline, as Cave M is now available for users. The performance of the treatment control system (TCS) components was characterized through beamline component tests and end-to-end tests.

3.2. Methods

In the following sections, we describe the layout, general specifications, and performance of beamline components in Cave M. The accelerator and beamlines are briefly reviewed here for the convenience of the reader. This includes relevant upgrades to the synchrotron, beamline components (such as the beam line detectors, power supplies for scanning magnets, interfaces to the timing system, beam request and scanning magnets, and the gating system) and the hardware and software of the dose delivery system (DDS). Additionally, we report selected preliminary performance characteristics of the beam delivery system for radiotherapy research.

3.2.1 SIS-18 Accelerator and Beamlines

Ions entering Cave M are accelerated in the synchrotron (Figure 3.1). The SIS-18 can accelerate ions ranging from hydrogen to uranium, with energies from 0.1 to 2 GeV/u for light ions and up to 4.7 GeV/u for protons [63]. It alternates between accelerating and spilling the beam, where each spill is the extraction phase for one bunch of accelerated ions. During the GSI pilot project, carbon beams of up to 2 × 108 ions per spill were available and slow extraction was utilized to deliver beams with 2.2 s spill durations and 2.2 s pauses between spills. In addition to the slow extraction method [54], fast resonance extraction is also available, which allows for delivering high intensity particle beams, accumulated in several beam bunches, in a single burst, usually on the order of 1 μs spill length [64]. The beamline was previously commissioned during the pilot project to deliver 80 to 430 MeV/u carbon ions to clinical safety standards [54].

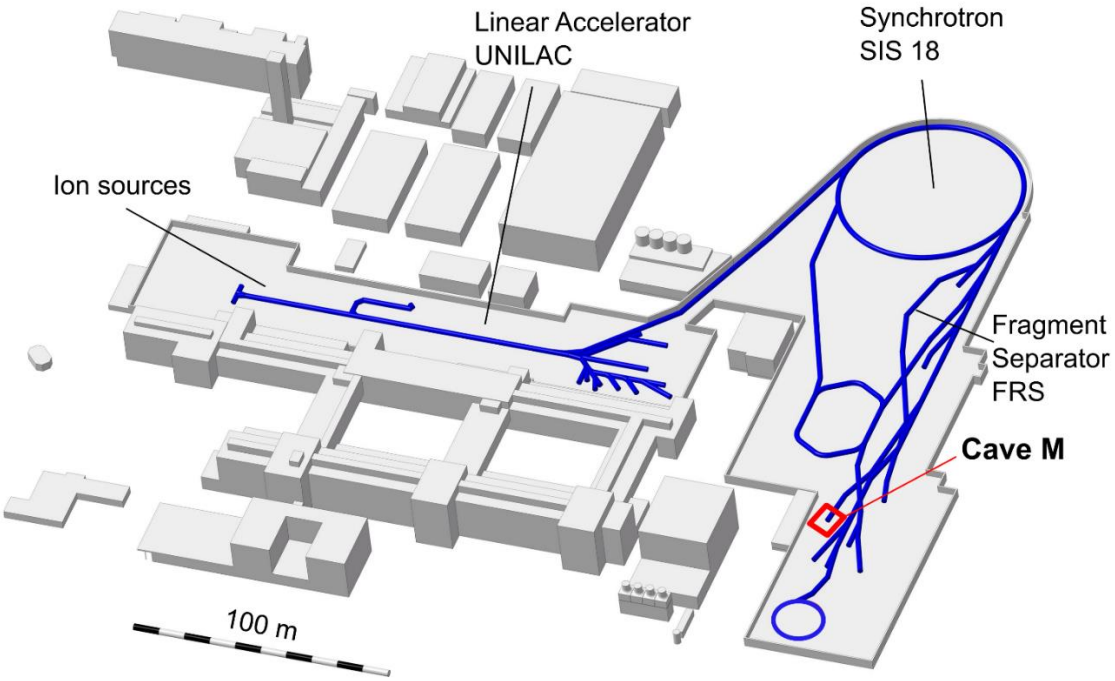

Figure 3.1. The layout of the accelerators and beamlines at GSI [63], including the ion sources, the universal linear accelerator (UNILAC), the synchrotron, the FRagment Separator (FRS), and the radiotherapy research facility (Cave M).

As part of FAIR Phase-0, the synchrotron has undergone several modifications. Spill pauses have been decreased to < 1 s, and spill duration can vary between 0.5 s and more than 10 s, with full cycle times of up to 20 s. Beam intensities of up to 1011 ions/spill have been achieved for proton and carbon ion beams. The acceleration and spill cycle patterns currently must be fixed during the beam tuning process, although we anticipate variable capability will become available in the future. Additionally, radio-frequency knockout extraction was added to the synchrotron extraction line and tuned, allowing for fast beam gating. Beam specifications and limitations, including radioprotection limitations are summarized in Table 3.1 [63]. For experiments requiring other ions, beam intensities or energies, the high-energy beamline (Cave A) and the Atomic Plasma Physics and Application (APPA) beamline are available. The main control system for this accelerator monitors and operates the major beam delivery components and the tuning of beam optics [61]. The spill cycle and beam parameters

are tuned from a beamline model and optimized manually via the main accelerator control system (ACS) [65] before beam delivery begins.

The original, Versa Module Eurocard (VME) based dose delivery system hardware of the ACS has been replaced with a control system with modern architecture. This architecture is also used at the Large Hadron Collider (LHC) and includes the LHC Software Architecture (LSA) based settings management system and a new timing system based on the White Rabbit framework [66].

Table 3.1. Summary of the current SIS-18 accelerator specifications for the ion-beam therapy research facility (Cave M), after FAIR Phase-0 upgrades.

Ion species	H – Fe*
Ion energies	100 MeV/u - 2 GeV/u for light ions*
Spill duration (slow extraction)	1 - 20 s
Emittance	1π - 20π mm mrad
Intensity variation	10^3 to 10^{11} ions / spill for p^+ and C^{6+}*
Maximum rigidity in SIS-18	18.5 Tm
Maximum rigidity to reach Cave M isocenter	11.8 Tm
Beam diameter	Typically 2 – 10 mm FWHM in air at isocenter

*Stated ranges conform to the radioprotection limits due room shielding in Cave M as well as beam scanning capabilities.

3.2.2 Beamline Components

One branch at the SIS-18 synchrotron facility is the Cave M beamline. This is a horizontal beamline that is equipped with components for directing the beam and magnets for focusing the beam, as well as the radiofrequency knockout (RFKO) system. An alternative beam path is also available, which traverses the FRagment Separator (FRS) and branches into Cave M, can be used to deliver radioactive ion beams. Figure 3.2 shows the layout of both of these beamlines, from the synchrotron to the nozzle, located within the therapy room.

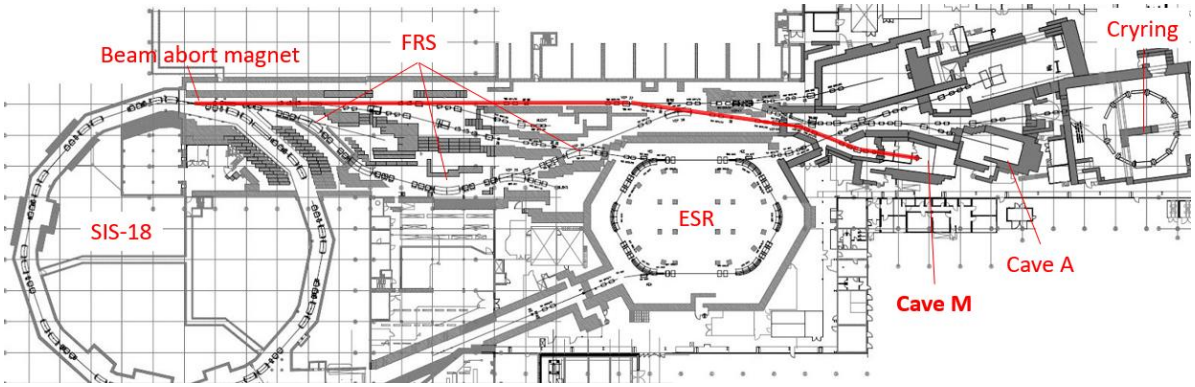

Figure 3.2. Layout of the beamline from the SIS-18 accelerator to the ion-beam therapy research facility (Cave M). Two beamlines branch out from the SIS-18, including the main line (indicated in red) and a secondary line that traverses the FRagment Separator (FRS) to deliver radioactive ion beams. Other notable beamlines include the cryogenic storage ring (Cryring), the heavy ion storage ring (ESR), and the high-energy beamline (Cave A).

3.2.3 Treatment Delivery Elements

Several major beam delivery components are used to monitor and control the delivery of treatment beams. These include orthogonally oriented two dipole magnets for pencil beam scanning, three beam-position monitoring detectors, two transmission-type ionization chambers to monitor the beam current, and a ripple filter [67], each located in the beam nozzle (Figure 3.3). These components are controlled by a DDS implemented with field programmable gate arrays (FPGA). To preserve the sharp lateral penumbra of the beam, the material through which the beam traverses in the nozzle was minimized. Specifically, the total water-equivalent path length (WEPL) of the components in the beam, excluding the ripple filter, is only 1.71 mm.

During beam delivery, these components are controlled and read out by a TCS. The real-time VME treatment control system (composed of control and readout module (SAM) digital signal processors) used previously [62], was no longer compatible with the accelerator and was replaced. The replacement TCS was adapted from the clinical DDS at the National Center for Oncological Hadrontherapy (CNAO), as described by Giordanengo *et al*. [25]. A research version of the TCS is found at both GSI and CNAO, and consists of a peripheral component interconnect (PCI) eXtensions express (PXIe) crate (National Instruments,

Austin, Texas) and FPGA cards. A description of the DDS used in this work was reported by Lis *et al*. [51]. Figure 3.4 shows components located at the end of the beamline.

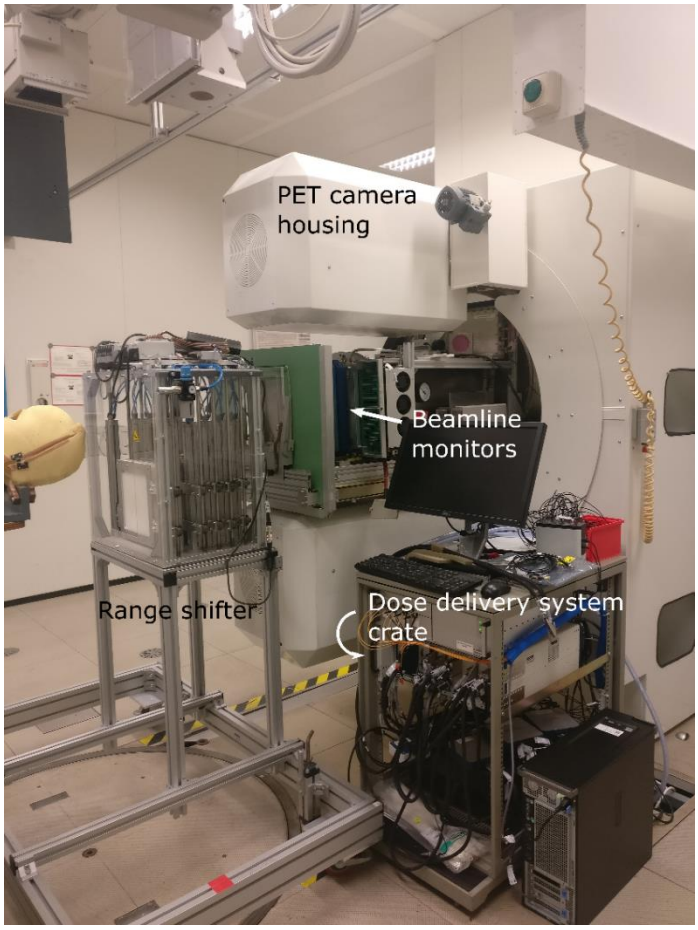

Figure 3.3. The radiotherapy research facility (Cave M) beam nozzle. Beam nozzle elements include the exit window to the vacuum chamber, five beamline monitors and positron emission photography (PET) camera. The PET camera has been removed and will be replace with other online beam monitoring technologies. The dose delivery system is located behind the beam nozzle (not shown).

All beam deliveries are made with their centroid location relative to the beamline's isocenter, which is localized with five positioning lasers mounted in the irradiation room. The maximum field size at isocenter is 20 × 20 cm^2. The coordinate systems were based on the recommendations of the International Electrotechnical Commission (IEC) (IEC 61217, 1996).

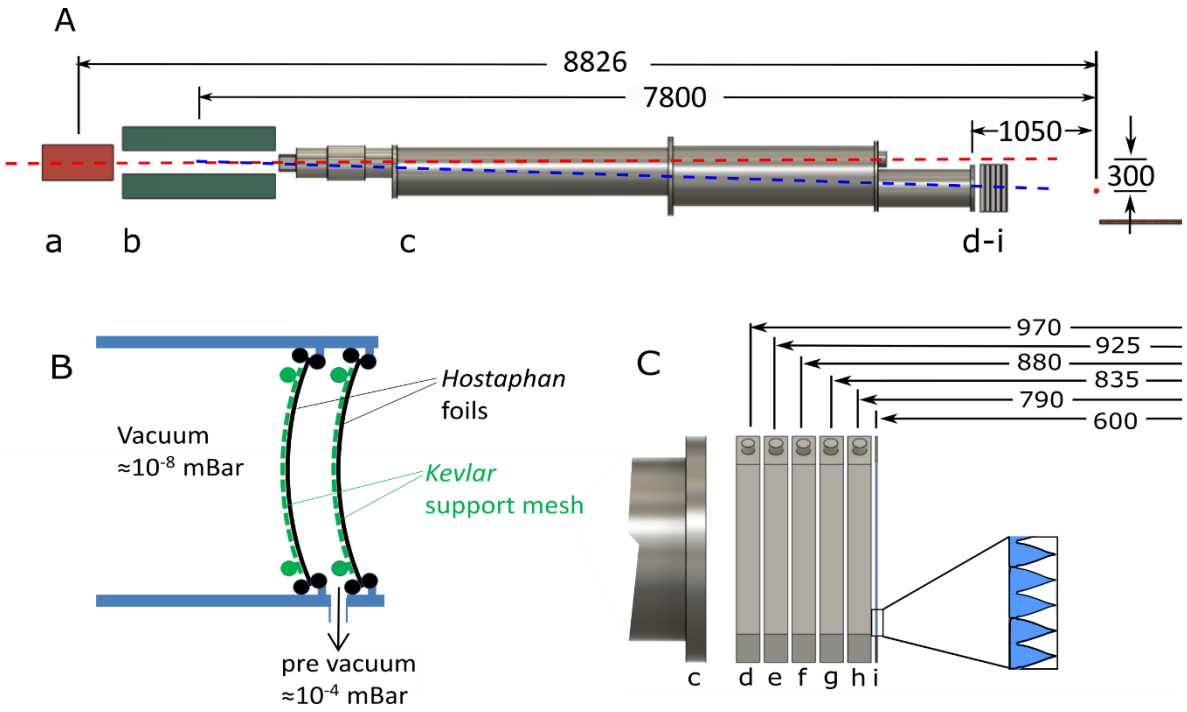

Figure 3.4. A) A schematic of the beam nozzle for ion-beam therapy research at GSI. The nozzle contains several beamline elements, including a) horizontal and b) vertical scanning magnets, c) the vacuum tube, d-i) five beam monitors and a ripple filter. All distances are relative to the isocenter position (indicated with a red dot). The patient couch is movable and found past the isocenter position. B) A schematic representation (not to scale) of the exit window design. The exit window contains a double layer of polyester film and support mesh. C) A close up of the exit window, beam monitors, including two position detectors (d) MWPC1 and h) MWPC2), and three transmission-type ionization chambers (e) IC2, f) IC1 and g) IC3), and i) a ripple filter, including distances from isocenter (in mm). The isocenter location is marked with a red '×'.

3.2.3.1. Treatment Control System

The current TCS runs on the Windows operating system (version 7; Microsoft, Redmond, Washington) and is based on real-time software (LabVIEW version 16.0; National Instruments, Austin, Texas). The TCS can also run on another commercial, real-time operating system (NXG Real-time Module LabVIEW; National Instruments, Austin, Texas), which is used in clinics. The architecture of the TCS closely resembles the version reported by Giordanengo *et al*. [25]. The delivery control crate comprises eight PXIe field programmable gate array (FPGA) modules: six PXIe-7821R cards, which we labeled memoFPGA, intFPGA, scanFPGA, pos1FPGA, pos2FPGA, and GSItimingFPGA and one PXIe-7820R card, which we labeled timingFPGA. These are dedicated to controlling

treatment slice loading and voxel sending, measuring the number of particles delivered, directing the beam spot, measuring beam spot position, acting as a timing system interface and synchronizing DDS operations with synchrotron operations, respectively. Additionally, there is one PXIe-7857R card, which serves as the motion control module, which will be referred to as motionFPGA. Detailed descriptions of the TCS can be found in the work by Lis *et al*. [51] and Giordanengo *et al*. [25].

3.2.3.2. Beam-abort and Beam-gating Systems

Beam delivery can be stopped for two reasons. During the course of a treatment, the beam is temporarily stopped at the end of an iso-energy slice (IES) or the end of treatment, once all beam spots have been delivered. Additionally, if abnormal conditions arise, the delivery may need to be prematurely and irreversibly terminated. Cave M has a beam abort system to perform these “treatment control” and “safety” operations.

During normal irradiations, the TCS uses the beam abort system for both of these operations. At the end of an IES, the beam is temporarily aborted, enabling the TCS to prepare delivery for the next IES. At the end of a treatment, the beam is permanently stopped. Additionally, the beam abort system is activated during abnormal and unsafe conditions, such as steering magnet failure. In this case, an interlock is set and the beam is also permanently and irreversibly aborted.

The beam abort system utilizes a fast quadrupole magnet, located at the SIS-18 extraction channel (Figure 3.2). The magnet rapidly shifts the beam tune towards resonance, destabilizing the particles and pushing them out of the beam path. The beam is then dumped in the synchrotron, so that recovery of the spill is not possible. Cave M also contains a beam gating system. The beam gating system is used for rapid, temporary beam interruption during the course of a spill. One example is beam gating synchronously with organ motion.

Beam gating is performed using RFKO extraction which is now utilized for rapid beam interruption and recovery and can also be used for beam abort functionality. In order to rapidly gate beam delivery, RFKO extraction is momentarily interrupted by switching the RFKO exciter off and then on again to resume the extraction. In addition, a frequency shift is introduced on a synchrotron cavity, moving the beam out of tune and effectively preventing extraction. This allows for beam gating and recovery multiple times during a spill, without requiring a fast kicker magnet in the beam extraction junction, as present in most clinical facilities. In contrast to fast kicker magnets, frequent and rapid gating with RFKO does not pose a risk of gating failure due to overheated power supplies for the magnets. On the other hand, RFKO beam pauses cannot fully block the beam and a small number of particles will leak through (as seen in Figure 3.8). During normal operation, the DDS triggers both systems automatically, as described in section 3.2.7.1. The abort system can also be triggered manually to gate the beam and pause the delivery.

3.2.3.3. Scanning Magnets

The scanning magnets in Cave M function by steering a pencil beam to each spot position via the raster scan technique, as described by Haberer *et al*. [46]. The center of the horizontal (X) and vertical (Y) magnets are located 8 826 mm and 7 800 mm from the isocenter, respectively, as seen in Figure 3.4. The scanning magnet power supplies and calibration were retained without alteration as originally installed in 1995. Table 3.2 lists selected characteristics of the scanning magnets and power supplies.

The communication interface for the scanning magnet power supplies was also redesigned. The scanning magnet power supply set values are communicated via a digital serial optical fiber cable and are sent at 20 Mbit/s with 20-bits per set value. The conversion of the spot position from lateral position (mm), from treatment plans, to power supply set values (current) for the scanning magnets are calculated using an analytical calibration

formula. Parameters used in the conversion formulas are stored in files that are loaded during DDS configuration and transmitted to the power supplies through the scanFPGA module of the TCS. The equations for this conversion are as follows:

$$X(\mathrm{mm}) = \frac{I_x - I0_x}{F_x(E)} + X0$$

$$Y(\mathrm{mm}) = \frac{I_y - I0_y}{F_y(E)} + Y0$$

where I_x and I_y are deflection currents, $I0_x$ and $I0_y$ are energy dependent correction factors, F_x and F_y are energy dependent rigidity correction factors, and X0 and Y0 are magnet offset correction factors. The GSI scanning magnet power supplies are unidirectional, with currents of up to 400 A. The nominal horizontal beam scanning velocity in the isocenter plane is 27.5 mm/ms for 430 MeV/u carbon beams. The beamline is vertically inclined by -2.203° and horizontally by 0.649°, accommodating the unipolar scanning magnets. This was designed as a safety feature for therapy, so that the beam will pass 300 mm above the isocenter and thus miss the location of a patient in the event of a scanning magnet failure. The vertical magnet strength limits the beam rigidity that can hit the isocenter to $B_\varrho < 11.8$ Tm, and to $B_\varrho < 8.9$ Tm for the maximum scan field of 200 × 200 mm^2 at isocenter.

Table 3.2. Specifications of the scanning magnets and their power supplies used in the GSI radiotherapy research facility (Cave M).

Characteristic	**Unit**	**X magnet**	**Y magnet**
Magnet gap	Mm	130	170
Magnet effective length	Mm	531	1209
Overall length	Mm	600	1290
Max deflection angle	°	1.45	3.30
Maximum field strength	T	0.38	0.38
Coil resistance	mΩ	63	154
Coil inductance	mH	9.2	33
Maximum current	A	400	400
Maximum voltage	V	± 368	± 330
Current ramp rate	kA/s	± 40	± 10
Scan speed for 280 MeV/u for C^{6+}	m/s	35	17
Power supply polarity		Unipolar	Unipolar

3.2.3.4. Exit Window

The exit window (Figure 3.4c) is found at the end of the evacuated segment of the beamline, which encloses a vacuum, typically at 10^{-8} mBar. The usable area of the exit window measures 210 × 210 mm^2, as required to create large enough lateral area for therapy. The inner layer of the vacuum window is composed of 100 μm, 14 g/m^2 polyester film (HOSTAPHAN RN 100; Mitsubishi Polyester film GmbH, Wiesbaden, Germany) that is supported by a 120 μm thick, 58 g/m^2 high-strength synthetic fiber mesh (Kevlar 49 Style 120; Fa. Cramer & Co, Heek, Germany), as seen in Figure 3.4b. Behind these materials, there is a second layer of polyester film and high-strength synthetic fiber, with the same properties, which is spaced at a few mm apart from the first layer, and contains pre-vacuum. The second layer serves as a therapy safety feature and creates a tighter vacuum. The front face of the exit window is located 1050 mm from isocenter.

3.2.3.5. Nozzle Detectors and Readout Algorithms

Five detectors are mounted in the nozzle (Figure 3.3). Three of these detectors are parallel plate ionization chambers – IC1, IC2, and IC3 – and are found 880, 925, and 835 mm from the isocenter, respectively. The ICs are $ArCO_2$ gas filled (80 % Ar and 20 % CO_2 by mass) ICs, which provide the beam intensity signal (a current that is proportional to particle rate). The remaining two detectors are position sensitive multi-wire proportional chambers (MWPC), which provide beam spot position information. The two MWPC detectors, denoted by MWPC1 and MWPC2, are located 970 mm and 790 mm from isocenter, respectively. Three of these detectors (IC1, IC2, and MWPC1) are currently used for beam monitoring. IC3 is used by the ACS for beam diagnostics and its signal is digitized independently of the DDS by a current to frequency converter. These detectors have been retained without modification from the original Cave M facility, where redundant dose and beam position

monitors were installed to fulfill the safety requirements for patient therapy; however, the electronic readout systems for these instruments were replaced.

The ICs have 210 × 210 mm^2 large area anodes and cathodes of 54 µm thick nickel coated polyester mesh. The two cathode planes are symmetrically arranged around the anode, with 10 mm gaps in between. The ICs are housed in an aluminum frame with 25 µm metallized plastic windows. Both ICs operate at a potential of 1.8 kV.

The IC1 current is read out by a fast current-to-voltage amplifier (DLPCA-200; FEMTO, Berlin, Germany) and the output voltage (-10 V to 10 V) is sampled by a 14 bit analog to digital converter (ADC) card (NI PXIe-5172 FPGA). The ADC card digitizes at 125 MHz rates, which is down-sampled to 1 MHz. The current from IC2 is read out with an application-specific integrated circuit (ASIC) chip (TERA09; DE.TEC.TOR Srl, Torino, Italy). This chip based on the TERA06 and TERA08 [68] chips, developed at the University of Torino, which are used at CNAO and MedAustron [69] respectively. As is done at CNAO, the second IC detector's counts are scaled down by a factor (G_{rel}) of 1.1: without this scaling factor, both ICs would alternate in signaling beam spot progression. Additionally, IC2 serves as a redundant detector in the case of IC1 failure.

The ASIC chip contains 64 charge-to-frequency converter channels [70]. The charge collected in the second ionization chamber (IC2) is accumulated by one of the 64 channels of the ASIC chip and converted to counts. The 32-bit charge counter of these channels is read out with 1 MHz rate by the intFPGA, at the same rate as for the ADC card from IC1.
The currents from all of the wires of each the MWPC position detectors are read out with four ASIC chips. A modular board has been designed for the position detector readout, containing up to 4 TERA09 chips. This board reads out the signals from the MWPC, which contains 224 wires in the X-plane and 224 wires in the Y-plane. Each wire is electronically

connected to a neighboring wire for noise reduction. The wires within the MWPC are each 50 µm diameter with 1 mm spacing between wires.

A gas electron multiplier (GEM) strip chamber detector [71, 72] is under development as the new, primary position detector. MWPC2 has been previously used as a redundant position readout for safety purposes during radiotherapy. For diverse and redundant readouts, one MWPC will be maintained. It is anticipated that the GEM detector will be considerably faster than the MWPC as it amplifies the fast electron signal by a factor of 10 to 100 through the gas amplification at the GEM layers while suppressing the slowly drifting positive ions. The GEM design has 256 strips per plane with a 1 mm pitch and requires one readout board per plane. Comprehensive tests on this detector are planned for 2021.

The IC counts are read out by the intFPGA, and when the set number of counts is reached, a signal is sent to the DDS controller to progress to the next beam spot. Particles numbers for each beam spot (extracted from the treatment plan) are converted to IC counts through the following equation:

$$\mathrm{Counts} = \frac{\mathrm{P} \times \mathrm{G_{Rel}} \times \mathrm{F(Xb, Yb)}}{\mathrm{k(E)} \times \mathrm{k_{TP}(T, P)} \times \mathrm{k_{QAfit}}}$$

where P is the number of particles, G_{Rel} is a ratio of the relative gain between the two ICs, F(Xb, Yb) is a spatial uniformity correction lookup table, k(E) is an energy-dependent conversion factor, k_{TP} is the temperature and pressure correction and k_{QAfit} is a correction factor derived from daily quality assurance measurements.

The MWPC detector is read out by the pos1FPGA, which analyses the signal distribution from all wires and determines the relative lateral beam position and spot size of each beam spot by calculating the center-of-mass and standard deviation [33] with the following equations:

$$\mathrm{X_{Pos}(FPGA\ units)} = \left(\frac{\mathrm{Kx_{Pos}} \times \mathrm{Xb} - \mathrm{X0_{Pos}}}{\mathrm{pch_{Pos}}} + \frac{\mathrm{NchX_{Pos}} - 1}{2}\right) 100$$

$$Y_{Pos}(\text{FPGA units}) = \left(\frac{Ky_{Pos} \times Yb - Y0_{Pos}}{pch_{Pos}} + \frac{NchY_{Pos} - 1}{2}\right) 100$$

where Kx_{Pos} and Ky_{Pos} are constant conversion factors for converting between mm and relative units used internally by the FPGA, $X0_{Pos}$ and $Y0_{Pos}$ are the offset of the position detector in the X and Y directions, respectively, pch_{Pos} is the pitch of the detector, $NchX_{Pos}$ and $NchY_{Pos}$ are the number of channels of the position detector, X_{Pos} and Y_{Pos} are the X and Y coordinates (in detector units) of the position detector, and Xb and Yb are the IEC coordinate X and Y positions (in mm) of the isocenter, respectively. The first term in the parentheses of the two equations converts the isocenter position into detector units, and the second term shifts the value to the expected multi-wire number. These values are scaled by × 100 for sub-millimeter position sensitivity. The pos1FPGA also provides position feedback to the scanning system for lateral position control of the beam.

3.2.3.6. Ripple Filter

A ripple filter is placed within the beamline, located 600 mm from the isocenter, to broaden the Bragg peak maximum region of ions to more than 2 mm. Two ripple filters are available, which are composed of 2 mm thick and 3 mm thick polymethyl methacrylate (PMMA) plates with a periodic structure of fine grooves with a well-defined ridge shape. The 3 mm ripple filter is mainly used during carbon ion therapy experiments. The design of the ripple filters was reported by Weber and Kraft [67].

3.2.3.7. Range Shifters

A portable binary range shifter is available to shift the beam penetration range. Following the upgrade of the SIS-18 ACS, treatment directed energy variation, performed by the synchrotron, was eliminated. This lost functionality provided 250 beam energy steps. In future phases of the FAIR upgrades, this capability will be restored; however, in the interim, the binary range shifter is available to shift the particle range and deliver dose volumes. The

range shifter is composed of 10 precisely cut polyethylene (PE) plates, each roughly doubling in size, to vary the WEPL delivery depth up to 100.2 mm. The plates are 0.063, 0.125, 0.235, 0.474, 0.951, 1.90, 3.80, 7.69, 15.46, and 30.91 mm water-equivalent thickness (WET). An additional 38.6 mm WET block can be added for additional depth. The range shifter is placed behind the ripple filter, with the thickest plate as close to isocenter as possible. Further details were reported by Simeonov *et al*. [73].

3.2.4 Motion Mitigation System

The motion mitigation system is an optional unit, used for motion mitigation studies. The motion mitigation capabilities are produced by two FPGAs, motionFPGA (PXIe-7857R, National Instruments, Austin Texas), and memoFPGA (PXIe-7821R, National Instruments, Austin Texas), which monitor target motion and redirect delivery to the measured motion position, respectively. The motionFPGA contains both analog and digital I/O and can be adapted to a variety of detection systems that deliver diverse forms of data, such as position in space, 1D motion traces, or externally pre-computed motion state information. Implemented motion mitigation strategies include conformal motion-synchronized dose delivery, gated delivery, and internal tumor volume [74] rescanning treatments. Tumor tracking, as described by Saito *et al*. [75], will be implemented for further motion mitigation studies. More information on the motion mitigation system was reported by Lis *et al*. [51].

3.2.5 Timing System and Beam Request Processor

The timing system is used to synchronize beam delivery to the accelerator spills. Timing signals are sent from the timing system interface (timingFPGA) and used within the other FPGAs to synchronize beam delivery signals between the FPGAs. An additional software layer has been added to the timing system interface to allow for communication between the beam request processor of the synchrotron and the DDS while maintaining the

timing events from the implemented DDS. This layer is located in the GSItimingFPGA and serves as a compatibility layer to allow the rest of the DDS to be used at multiple centers without modification. Spill patterns are pre-set by the ACS during machine tuning, along with other machine parameters, such as focal spot size and particle intensity, and only signals for the start and end of treatment are sent to the central accelerator during delivery.

The developed beam request software communicates beam progression signals with the ACS. Signals are sent via a transmission control protocol (TCP) to the ACS, which triggers the beginning and end of beam delivery with the 'Start Treat' and 'End Treat' signals. Spill patterns from pre-set beam parameters (spot size, energy, particle flux) are delivered until the 'End of Treatment' signal is received. For each spill, synchrotron timing events trigger the stop and start of a spill through the 'Begin Extraction' and 'End Extraction' signals. These external signals trigger 'BeamOn' and 'BeamOff' signals internally to synchronize the DDS FPGAs during delivery. 'NextCycle' and 'RepeatCycle' signals are generated from the DDS to signal the accelerator to repeat a spill or transition to the next energy, respectively. At the end of an IES and in between spills, the fast-extraction-stop quadrupole magnet is activated until the end of that spill, as seen in Figure 3.5. Additionally, in physics mode (beam delivery without a treatment plan) the beam request system interface can request one beam spill, 'Trigger Request', or a repeating pattern of spills, 'Continuous request'. During plan delivery, these modes are disabled and the beam request begins automatically once a treatment plan is loaded and sent. As described in section 3.2.3.7, only single energies could be pre-set with the current ACS. However, the existing CNAO beam parameter code protocols (so-called CycleCodes) are still maintained, anticipating for future multi-energy switching capabilities at GSI. These CycleCodes [25] are hexadecimal codes that represent accelerator energy settings for each IES. To deliver 3D volumes at GSI, the

CycleCodes were converted to settings for the binary range shifter, allowing range modulation.

Figure 3.5. Timing events from the accelerator, where 'Begin Extraction' triggers the beginning of a spill, 'End Extraction' triggers the end of a spill, and both 'End Extraction' and 'End of Slice' signals turn on the 'Beam Abort' signal until a spill is completed or at the end of a treatment. These signals are recorded along with motion phase changes and can be used to reconstruct delivered doses from delivery log files.

3.2.6 Pre- and Post-treatment

Treatment plans are created through two methods: simple, mono-energetic rectangular plans with homogenous fluences are generated from a plan creation tool, while 3D geometries are created with the research treatment planning system at GSI, TRiP4D [26]. TRiP4D is an extension of TRiP98 [76, 77] that considers temporal changes to patient anatomy during treatment plan creation. The plans and, in the case of motion-compensation deliveries, plan libraries were designed with 4D-optimization to target volumes [29], which results in a conformal treatment plan. Robustness has also been incorporated, allowing for minimizing the effects of delivery degradation due to range uncertainties, patient set-up errors and uncertainties in anatomy changes due to respiratory motion [78]. TRiP4D has been optimized for carbon, oxygen and helium ion beams, but can be extended to include additional ions. Additionally, the DDS has been designed to accept Digital Imaging and Communications in Medicine (DICOM) standard and VOXELPLAN format [79] treatment plans and can easily be modified for additional plan format options.

During delivery, the data from the beam monitors and scanning magnets for each delivered spot is logged into binary dose delivery data (DDD) log files. For motion-

synchronized deliveries, detected motion is logged into binary motion monitoring data (MMD) files. These files can be fed back into TRiP4D for 3D and 4D dose reconstructions.

3.2.7 Description of Verification Tests

Online and offline tests were performed during several stages of development to verify the functionality of each subsystem. The offline subunit tests are summarized in Table 3.3. Signal transmitting and receiving, as well as the correct calibration of the scanning magnets and beam line detectors was confirmed through measurements with dedicated testing software. Timing events, treatment progression and beam request functionality were confirmed on a digital oscilloscope (R&S RTB2004; Rohde & Schwarz, Munich, Germany) and through timing system log file analysis. Subsequently, the integrated functionality of each sub-system was also confirmed offline by delivering treatments to completion with simulated beam signals and then assessing accuracy in DDD files and treatment logs.

Online subunit tests were performed to visualize the performance of each beamline component and end-to-end tests were performed to test the entire TCS during delivery (Table 4). The beam output, or the absorbed dose to water at isocenter, was measured with a farmer type ionization chamber and an electrometer (Unidos E, PTW, Freiburg, Germany). Additionally, each batch of radiochromic films (Gafchromic EBT3; ISP, Wayne, New Jersey) was calibrated by delivering a pattern of eight squares of increasing particle fluence to a film placed behind 2 cm of PMMA plastic [80]. A calibration curve, converting optical density values to particle fluence was then applied to each film, using an image analysis software, (ImageJ version 1.52a; National Institute of Health, Bethesda, Maryland). A 60×60 cm^2 square profile was delivered three times to a 2D ionization chamber array detector (Octavius VDR 1500; PTW, Freiburg, Germany) to measure the absolute dose and delivery constancy (calculated with standard deviation of the absolute dose measurements). Experiments were performed by delivering simple geometries and spot patterns to the detectors. Additionally,

cubes and ellipsoids were delivered to confirm the performance of the range shifter and the capability to deliver multiple depth plans uniformly. In addition to online performance verification tests, the performance of individual beamline components was also studied experimentally.

End-to-end tests were performed, including field homogeneity, beam reproducibility, dosimetric precision and delivery speed. Field homogeneity tests were performed by delivering a uniform 60 × 60 mm^2 square field to radiochromic films, placed behind 2 cm of PMMA plastic. The homogeneity was calculated with the homogeneity index (HI), using the equation $HI = (H_{max} - H_{min}) / (H_{max} + H_{min}) \times 100$ [25]. Reproducibility measurements were performed by delivering the same square field multiple times to a farmer type IC chamber. Additionally, 3D dosimetry was performed to measure doses across a uniform square volume. The HI was measured across several depths. Treatment delivery speed was assessed by delivering a square shaped plan with ramped particle intensities for each line, starting at 500 000 particles per beam spot and decreasing to 100 000 particles per beam spot. The 2D ionization chamber array detector was used for several measurements, including uniformity measurements, and is a standard tool for experiments in Cave M.

Table 3.3. Summary of offline subunit verification tests and the relevant analysis tool for each portion of the dose delivery system and integration tests to the beamline components. SLD refers to slice file data and DDD refers to the dose delivery data.

Subunit	**Test**	**Analysis tool**
Beam request	Triggers a single spill	Virtual beam spill visualized on oscilloscope
	Continuous beam request sent	A series of spills visualized on oscilloscope
	Triggers start and end of treatment	A series of spills visualized on oscilloscope
Timing system	Timing events sent to other FPGAs	Timing log file analysis
Range shifter	Triggers correct change total thickness	Set manually and confirm total thickness
	Delivers simple plan of several depths	Confirm CycleCodes and depths correspond
Beam abort	Boolean trigger from application	Visualized on oscilloscope
Scanning magnets	Communication with power supplies	Visualized on hall probes
	Coordinates correct	Set values with an application
	Power supply calibration - spot position correct	Set values with an application
Ionization chambers	Simulates signal to amplifier	Observe signals
	Signal counts calibration	Treatment log file analysis
	Signals spot and spill progression	Observation in DDD files
	IC1 as dominant detector	Observation in DDD files
Motion mitigation system	Connection to external motion signal	Observation of motion signal from motion sensor in the motion monitoring system
	Detection of motion	Observation of motion phases in the DDS
	Sends of motion phases	Receiving phases treatment in log files
Multi-wire position chamber readout	Spot position as expected	Set values with an application
Treatment plan handling	Loads entire plan libraries	SLD file analysis
	Sends single spots	DDD file analysis
	Sub-plan switching when motion phase changes	DDD file analysis

Table 3.4. Summary of verification tests performed at GSI. The described treatment plans were designed to test individual functionalities.

Plan	**Subsystem/system**	**Test**
8 spots in 1 slice	Beam request	Delivery completion
	Scanning	Spot position in correct location
	Scanning, position detectors	Correct orientation
	Detectors	Multiple spots delivery
	Gating system	End-of-treatment beam abort
5 spots in 5 slices	Scanning magnets	Spot position accuracy
	Timing system	Synchronized delivery of multiple spills
	Beam request	Slice change when triggered
	Gating system	End-of-spill beam abort
6 lines, each in 6 slices	Gating system	Gating related to motion handling
	Treatment plan handling	Capability to deliver plan non-sequentially
25 spots plan at various depths	Range shifter	Beam spot size and shape at different depths
Uniform squares	End-to-end	Beam reproducibility
	End-to-end	Uniformity at several depths
Ramp square	Scanning magnets	Scanning magnet speed limits and accuracy

3.2.7.1. Beamline Component Tests

The effect of the range shifter on the beam spot profile was characterized by delivering 25 beam spots, each to a different range shifter depth, varying from 0 to 100.18 mm. To perform this, a 25 beam spot grid plan was delivered to a radiochromic film. The film was calibrated in the image analysis software, by applying a gray-value to particle fluence correction, and corrected for the linear energy transfer (LET) dependence response for C^{6+} . To determine the beam spot sizes, the full width half maximum (FWHM) was determined and the beam spot profiles were fit to double Gaussian functions. This data was used to update TRiP4D for deliveries using the range shifter.

The functionality of the MWPC was tested by delivering single beam spots and correlating the positions and fluence profiles measured in the detector with spot positions found in the DDD files and the profiles measured with a digital oscilloscope card (PXIe-5172; National Instruments, Austin, Texas), respectively. Additionally, the speed of the beam spot position readout was characterized by calculating the internal deadtime and comparing the determined position with the delivery duration.

The readout for IC1 was tested by delivering a 2.5 Gy square-shaped plan to a calibrated farmer chamber (PTW 30010; PTW, Freiburg, Germany). The calibration of the beamline IC chambers was calculated and confirmed using an in-house developed software. The functionality of the redundant readouts of IC1 (ADC) and IC2 (TERA09) was confirmed with C^{6+} beams by evaluating the difference in electric charge between measured beam spot counts and planned beam spot counts matched for both ICs. Additional validation testing studies are ongoing.

Tests were also performed to determine the maximum delivery speed. Delivery speed is limited by scan speed and position-detector-readout speed, which dictates the minimum particle number when creating treatment plans. Two square fields, each with increasing particle numbers for each row of the treatment plan in either the horizontal or the vertical direction, were delivered with carbon ion beams. The actual beam spot positions in the DDD log files were compared to expected positions in the slice delivery (SLD) files. Position accuracy was calculated by calculating the distance to agreement for each spot.

The performance of the fast (RFKO) gating system and the beam abort system was benchmarked. Two types of tests were performed manually to characterize the DDS response to anomalous losses of beam. First, the functionality of both the quadrupole beam abort and the RFKO gating system was tested by connecting the trigger line of the quadrupole magnet extraction and, respectively, the RFKO system, to the timingFPGA and manually triggering

beam disruption with a virtual Boolean switch. Subsequently, the speed of both modes of beam disruption and recovery were assessed to determine the rapid gating performance capabilities of the gating system during treatment deliveries. These tests were performed by manually triggering the RFKO extraction off and on in the same manner, while measuring the particle fluence (in μs) for single spills. The digital oscilloscope card was used to measure the particle intensity at 1.25 MHz.

3.3. Results

Tests to confirm the functionality and reliability of Cave M were performed and are reported here. Preliminary tests for each beamline component were performed offline (without beam) and online, using the available ion beams (Ar^{+18} and C^{6+}). Successful signal transmission, reception and proper calibration were confirmed for each sub-system through the analysis tools described in Table 3.3. The hardware and software to the beamline components have been successfully integrated into the experimental therapy beamline at GSI. The pass/fail tests described in Table 3.4 all passed. Further results for tests on beam spot size and shape at different depths, beam reproducibility and uniformity, spot position accuracy, gating and beam abort tests are presented below.

Beamline component functionality tests (see section 3.3.2.7.1) were performed successfully and test case plan libraries were delivered to completion. Timing system events, including ‘Start Treat’, ‘End Treat’, ‘Start Extraction’, and ‘End Extraction’ were confirmed to be transmitted to the beam request processor. The scanning system and detector systems were found to be properly calibrated and in the correct orientation. At the time of writing, signal degradation due to noise has limited the position detector readout speed, and the ASIC readout cards are being redesigned.

The beam spreading when using the range shifter was characterized for C^{6+} and p^{+} beams by delivering 25 spots at 25 different range shifter settings (Figure 3.6). The beam spot

FWHM for each range shifter depth varied from 3.15 to 7.15 mm for C^{6+} and 8.0 to 19.4 mm for p^{+}, corresponding to the range of 0 to 100.8 mm in water. FWHM for each energy step was interpolated with a linear fit curve and resulting beam spot sizes for each energy step were used during log file based dose reconstructions. The base data of TRiP98 will be updated accordingly.

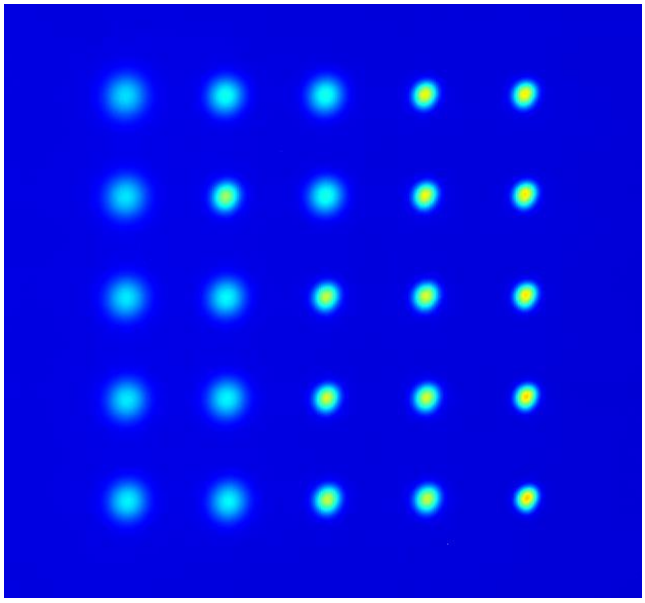

Figure 3.6. Beam spot sizes for 25 range shifter settings, delivered with carbon ion beams.

The calibration of the beamline IC chambers and redundant readout functionality was confirmed. Beam position detection accuracy was assessed by comparing measured beam spot positions on a radiochromic film with planned positions. Accuracy was found to be within 1 mm in the horizontal and vertical directions. High noise due to the design of the position detector readout remain, and portions of the board are being redesigned.

The scanning direction and calibration was confirmed by manually setting the magnet set values to various positions. Without position feedback, the scanning magnet set values were found to be accurate within 1 mm, and maximum deviations were found to be 0.99 mm ± 0.1 % and 0.99 mm ± 0.06 % for the vertical and horizontal scan directions, respectively, as seen in Figure 3.7. The scanning magnet accuracy was 0.5 mm for the ramp square delivery. The accuracy of delivery is expected to increase once position feedback from

the position detections to the scanning magnets is in place. Minimum detector counts are currently set to 20 000 particles per spot for faster delivery: lower-weighted beam spots can create a bottle-neck in irradiation speed due to limitations in measurement precision.

The usable maximum energy is limited by ion species and by scanning magnet strength. The maximum energy to deliver ions to isocenter and across a 10 × 10 cm^2 scan field were calculated for various ion species and are summarized in Table 3.5.

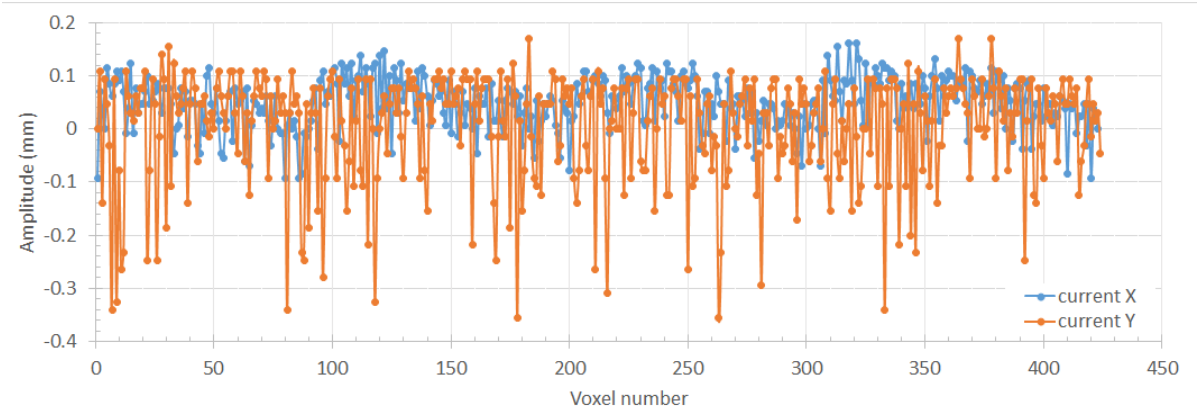

Figure 3.7. Beam spot position accuracy for a cube plan delivery, delivered with 240 MeV/u carbon ions, using the range shifter. The difference between planned and recorded current values in the X (orange) and Y (blue) directions are indicated.

Table 3.5. Maximum energies for various ions, with respect to scanning magnet limitations.

Ion	**Delivery to isocenter**	**Delivery across 10 × 10 cm^2 scan field**
P^{+}	2 000 MeV	1 850 MeV
Fe^{26+}	950 MeV/u	575 MeV/u
C^{6+}	1 100 MeV/u	680 MeV/u

The functionality and performance of the beam abort and beam gating systems was confirmed. The beam abort system was activated when triggered, including at the end of each slice and until the completion of each spill, as expected. RFKO gating tests for multi-gating capabilities determined that reduction to 5 % of the full beam intensity was achievable within 2 ms, and full beam disruption, to 1 % intensity, was achievable within 20 ms, as seen in Figure 3.8. The minimum gate duration was determined to be 10 ms. Further RFKO tuning will be performed to improve beam gating speeds. The beam ramping was optimized to

achieve these results. These rates were sufficient to conduct motion-synchronized irradiations. Comparable clinical fast gating systems, such as that at CNAO, are capable of complete beam disruption within 150 µs.

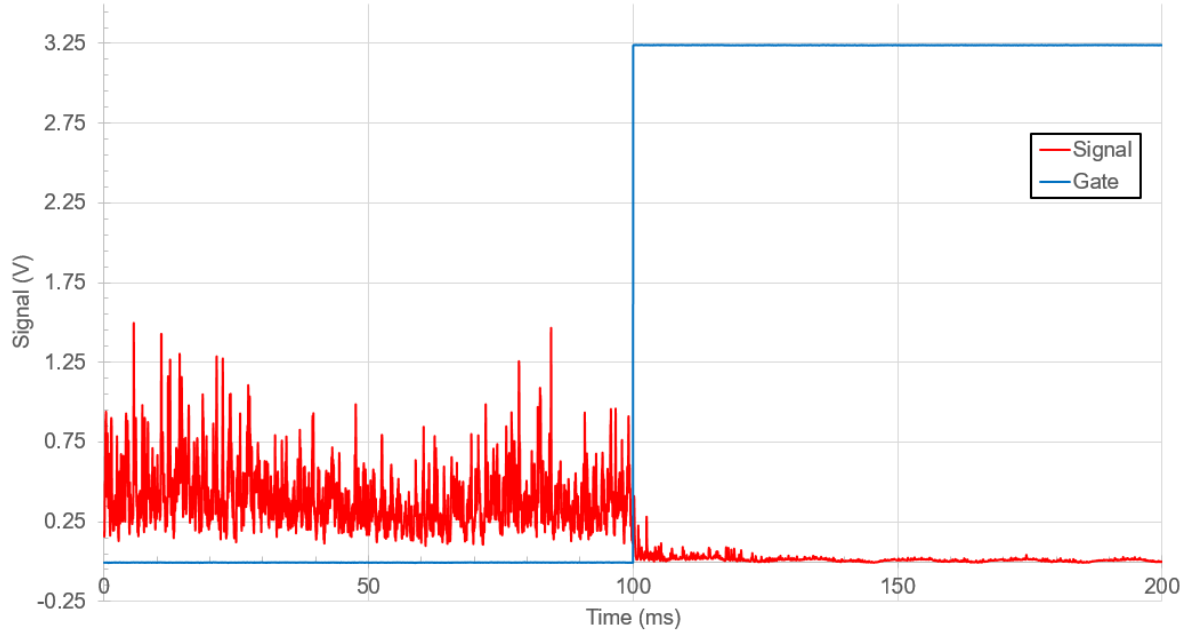

Figure 3.8. Beam gating by halting the radiofrequency knockout extraction. The beam intensity was measured at 1.25 MHz using the beam nozzle IC (red) and readout by an amplitude to digital converter (ADC) oscilloscope card. Particle intensity is shown before and after activating the beam gate signal (blue).

Dosimetry was performed prior to performing other beam deliveries. Absolute dosimetry measurements with a farmer chamber resulted in a dose reproducibility of ± 1.07 % for 2.5 Gy deliveries, where standard deviations of < 3 % are considered acceptable. Field homogeneity of a square, delivered to a depth of 20 mm into PMMA was within 4.9 % in the horizontal direction and 4.7 % in the vertical direction (Figure 3.9a). Gamma index analysis pass rates for cube deliveries, comparing measurements with the 2D IC array detector to log file dose reconstructions, were found to be 100 %. Time to deliver the cube was 423 s. The slight misalignment between the two data sets in Figure 11b may be due to limitations to the resolution of the 2D IC array detector and imperfect tuning of the beam spot prior to experiments.

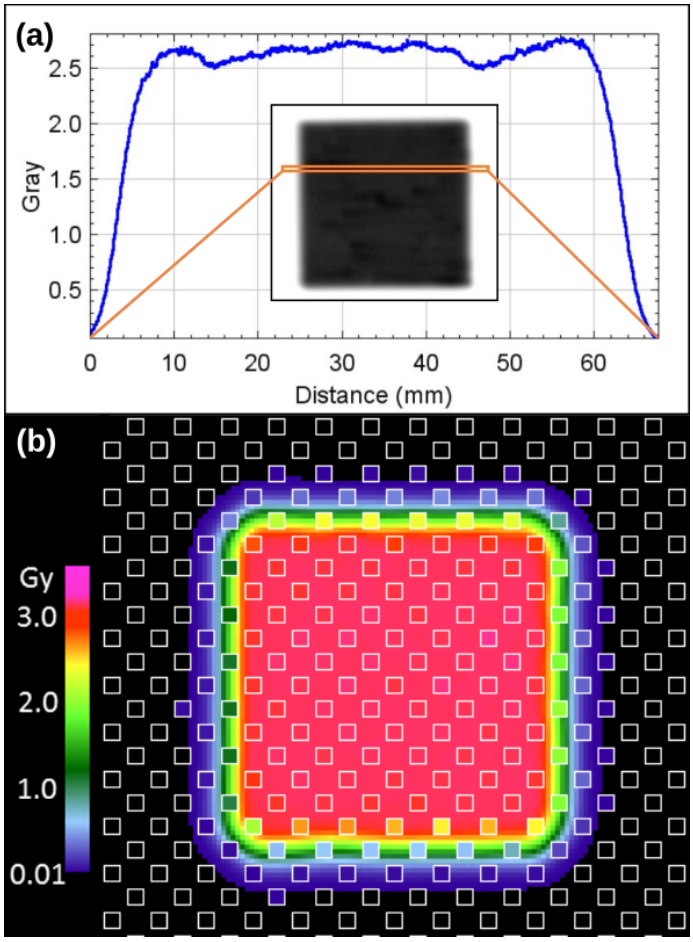

Figure 3.9. Uniformity measurements of a 60 × 60 mm^2 square, placed behind 20 mm of PMMA plastic, measured with a (a) radiochromic film and the horizontal uniformity profile; b) measurements of a 60 × 60 × 60 mm^3 cube, reconstructed from delivery log files and overlaid with the respective 2D ionization chamber array detector measurement (white boxes).

3.4. Discussion

We have re-designed and upgraded the GSI radiotherapy research facility (Cave M) during the FAIR shutdown period from 2016 to 2018. We designed the beamline to maintain clinical specifications and have adapted and extended a clinical dose delivery system (DDS) from CNAO, for 4D capabilities, to allow for experiments in clinical-like conditions. Tests have been performed to confirm functionality and consistent performance of the beamline elements and the DDS. The presented information is also intended as a reference for external users to determine the possibility of conducting research at GSI and applying for beam time through the GSI BioPAC [81]. The major finding of this study is that the updated Cave M has

been successfully characterized and is now available for users. The new DDS was used to perform the first experiments on biological samples, including uniform spread-out Bragg peak irradiations of culture flasks with protons and carbon ion beams, and online microscopy experiments with protons, carbon and iron ions.

The implication is that researchers may exploit this new research infrastructure to pursue new avenues of research. Cave M has been developed in such a matter that continuous upgrades will allow for performing innovative clinical research, beyond the capabilities of current medical accelerators. This will allow for testing innovative new therapy methods in conditions beyond the limitations of clinical lines, but is not limited to therapy research. GSI offers multiple modes of beam extraction, including fast extraction, slow extraction and radiofrequency knockout extraction, and a broad range of beam energies, which allows for testing novel delivery methods. High dose rates and a broad range of particle energies will allow for studying Flash therapy [48]; multiple ion sources allow for mixed beam irradiations [82]; the alternative beam path, through the FRS allows for radioactive ion irradiation [49]; rapid gating and position feedback will allow for testing motion mitigation strategies, including tracking and conformal, motion-synchronized delivery [31, 51, 83]. The Cave M layout is not the final design, but the current stage in the continuous upgrades as part of FAIR-GSI phase-0. With further upgrades, additional capabilities will be possible, including dynamic intensity control [84] and fast beam energy switching.

This work presents, for the first time, on the upgrades to the original Cave M design, including a comprehensive description of the updated beamline and the TCS for delivering arbitrary dose volumes. The results of this study are comparable to performance specifications of clinical accelerators, such as CNAO [35, 85] and NIRS [86]. At CNAO, commissioning results revealed that all beam spots could be delivered within < 1.5 mm of the expected positions (without position feedback) and with particle fluence accuracies of

< 2.5 %. The resulting dose distributions were 100 % gamma index pass rates for 3 %/3 mm criteria when delivering a representative patient plan [35]. The time to deliver a 60 mm diameter sphere, with carbon ion beams, at CNAO was found to be 223 s, excluding the time required to prepare the accelerator before treatment. At NIRS, commissioning results found that the difference between measured and expected beam spot positions was < ± 0.3 mm. Measured doses were within ± 2 % of the expected dose [87]. Typical delivery times are not noted in the literature, however particle intensity and scan speed limits suggest around × 10 faster deliveries [88]. Our results reveal a particle position accuracy of < 1 mm, a particle fluence accuracy of < 1.07 %. The time to deliver a 60 × 60 × 40 mm^3 cuboid was found to be 423 s. By increasing particle fluences during delivery, delivery speeds at Cave M can be theoretically increased by a factor of 10. In order to perform Flash experiments with proton and carbon ion beams, particle rates of 1013 s^{-1} and 1010 s^{-1}, respectively, will be required [48]. With the continued FAIR upgrades to the SIS-18, these rates will be achievable. Beam nozzle intensity and position monitors are in principle compatible with Flash dose rates, but research into optimal dosimetry is ongoing.

This work has several strengths. First, a majority of the features of Cave M that were developed for clinical use during the pilot project are maintained, and the DDS has been adapted from the clinical ion therapy facility CNAO. This is a major advantage because the beamline components were designed to clinical standards [25, 54], and the beamline is structured so that beam monitoring components can be inserted. Further, a majority of the safety interlocks are already in place, so as each upgraded element was implemented, and as new therapy methods are developed, the safety and beam monitoring strategies can be directly developed as well. Another strength is that a broad variety of tests were performed to validate that we have met design specifications in these upgrades. This study was performed on multiple ions, at multiple particle intensities, and each component was tested extensively

offline before performing online and end-to-end tests. Though the tests described here are not exhaustive, they represent many tests that are required to confirm the performance of the facility for radiotherapy research studies. Finally, several of the updated components, including the DDS and the ASIC readout chips, are commercial components. This ensures the reliability of these components, allows for straightforward updates and modifications, as well as documentation on the hardware and underlying software and technical support.

One limitation of this work is that we do not give an in-depth description of each component of the beam delivery system. Here, we provide only brief summaries and example test results. This is not a major limitation because detailed accounts and exhaustive tests will be provided in other studies. Another limitation is that this study has been written at a time when some beamline components are in the preliminary stages of testing or are still being developed. The readouts for the MWPCs and GEM detectors have not been fully implemented, so online beam position was not available, and the RFKO gating system has not been fully tuned. These components are expected to be available in the next couple of years. This is not a major limitation, as the accuracy of the scanning magnets allowed for delivering beam spots within ± 1 mm of the planned position without positions detector feedback. Further, the beamline detectors have been confirmed to deliver accurate irradiations, as the beamline detectors have been previously used for therapy and only their readouts have been modified. Additionally, only single energies are available for experiments and a range shifter is used to deliver tumor volumes. The range shifter produces significant particle scattering, due to the air gaps between each plate. Multiple energy deliveries are not anticipated at this time, but a new range shifter will be developed to reduce beam scattering. However, this is not a major limitation, as delivering dose volumes is still possible, and increases to the beam spot size for each range shifter setting has been measured and implemented into the treatment planning system. Finally, the delivery system also can already

deliver full treatments to the requirements of most users, and updates on the status of development can be provided.

Cave M is now available for pre-clinical research experiments. Prospective users should be aware of the current status, limitations, and the planned future upgrades. The online positron emission tomography (PET) camera that was used during the GSI pilot project is currently not functional. The entire system for the online PET system [89] has been removed and the PET imaging components have become outdated. The PET system will be replaced for the study of radioactive beams within the ERC Advanced Grant – BARB [90]. In the future, a hybrid monitor for prompt gamma ray imaging and PET will be used for online beam monitoring of the secondary particles of four beta emitters (C-10, C-11, O-14, and O-15). These aspects may be potential obstacles for users in the near term and should be available in the coming years. Interested users should contact the Biophysics department at GSI for the beamline status.

In the future, the beamline components will undergo several more updates to increase delivery speed. New power supplies for the scanning system will be implemented, which can double the scan speeds. Additionally, the two scanning magnets will be updated to three smaller and faster ones. The current magnet system, a very large vertical scanner, will be divided into one dipole, responsible for tilting the beam into the isocenter, and one scanning magnet, responsible for directing the beam during treatment. The scanning magnet will be considerably smaller due to the smaller scanning angle. Both scanning magnets will be controlled by bipolar power supplies, and will be designed for a smaller inductivity, allowing for faster operation. The new system can be used later for the scanning system at the FAIR BIOMAT beamline [74], as the size of the magnet allows for scanning higher energy ions. The intensity control loop will be characterized and calibrated to achieve a stable and constant extracted intensity. Additionally, new detectors, including the GEM position

detector, will enhance precision and beam intensity and position measurement speed. Finally, ongoing updates to the SIS-18, in preparation for the FAIR project, aim to increase the maximum beam intensity for all ions.

The adapted DDS has also been updated, as described by Lis *et al*. [51]. Modifications have been made from the original DDS design [25] to repackage the system as a fully modular design, with integrated motion detection and motion-synchronized delivery capabilities. This upgrade, including several significant changes and upgrades to the hardware and software of the DDS, is an example of how we envision the future use of Cave M: as a testing facility for pre-clinical research on delivery strategies that require intervention with the accelerator line and would provide undue risk if performed in clinical environment, but are posed to produce major advances in radiation therapy if thoroughly investigated and vetted before being implemented to clinic practice.

3.5. Conclusion

The ion-beam therapy research facility described in this study has been updated for performing experiments under clinic-like conditions. Cave M has re-opened in 2020 to external users. The layout and specifications for each beamline component have been described. The performance testing results confirm that each component performs to clinical specifications. Cave M will provide for a near-ideal infrastructure and environment for research on novel radiation therapies with heavy ion beams.

Chapter 4. A Modular System for Treating Moving Anatomical Targets with Scanned Ion Beams at Multiple Facilities; Pre-clinical Testing for Quality and Safety of Beam Delivery

4.1. Introduction

Quality, safety and radioprotection are integral parts of radiotherapy facilities [91]. Radioprotection and area monitoring systems are designed to protect staff under the principles of justification, optimization and limitation [92]. During regular operation, the critical safety operations of each accelerator are regulated by the main treatment control room and, for redundancy, by independent safety interlock systems [93]. Medical systems used for radiotherapy, including accelerators, treatment control systems, and safety systems, typically take into account safety considerations during the design, construction, preclinical, and clinical phases. In addition, safety is considered in regulatory processes, e.g., in the USA, the 510k premarket clearance by the Food and Drug Administration (FDA) (21 C.F.R. § 807.81-807.97). Once in clinical use, exhaustive safety and quality assurance testing must be periodically performed. Quality management has been an integral part of modern radiotherapy and is essential for safe and effective treatments. Organizations such as the American Association of Physicists in Medicine (AAPM), American College of Radiology (ACR), the American Society for Radiation Oncology (ASTRO), the International Atomic Energy Agency (IAEA), and the European Society for Radiology and Oncology (ESTRO) [94] have established safety standards and guidelines [95]. Radiotherapy device manufacturers and therapy centers typically agree upon test procedures as part of the acceptance testing process and guidelines are published for verifying the performance and safety of radiotherapy equipment during commissioning and periodic quality assurance testing [96-100]. Beam commissioning and QA standards have been established for proton

---

This chapter was previously published as “Lis M et al. (2021) A Modular System for Treating Moving Anatomical Targets with Scanned Ion Beams at Multiple Facilities: Pre-Clinical Testing for Quality and Safety of Beam Delivery Frontiers in Oncology 11” Reprinted by permission of Frontiers.

beams in the AAPM Task Group 224 report [101] and are being established for ion beam therapies through the PAR-13-371 National Cancer Institute (NCI) grant [102]. As the complexity of modern treatment planning and delivery technologies, such as scanned ion beam therapy, has increased, additional consideration of safety is necessary. There is typically a lag between implementing modern therapies into the clinic and developing consensus safety guidelines for these therapies. The AAPM's Task Group 100 (TG-100) wrote a report [103] on an analysis methodology that aims to reduce this lag. The report is a framework to prospectively assess all aspects of workflow for possible critical safety errors in existing and new therapy methods [103, 104].

Broadly, the methods of safety analysis and risk mitigation are mature, rich, and generally applicable. Several major analysis strategies have been applied to clinical radiotherapy. For example, the AAPM and the Joint Commission on Accreditation of Healthcare Organizations (JCAHO) recommended the failure modes and effects analysis (FMEA), adapted from aviation safety to radiotherapy, as a general guidance for performing safety analyses [105]. Additionally, guidelines have been developed by groups such as the 'Accidental and unintended exposures in radiotherapy' (ACCIRAD) project of the European Commission (EC), the Radiation Oncology Incident Learning System (RO-ILS; ASTRO, Arlington, VA), which are based on pooled data on reported adverse events [106, 107]. Many photon therapy clinics have adopted these methods [108, 109], while others have developed their own variations [110]. However, knowledge of the safety of emerging radiation therapy technologies is inherently incomplete. Furthermore, emerging technologies have been identified as a common source of delivery errors [111]. It is not yet clear how best to address the safety of emerging technologies, particularly for systems that treat moving tumors. It has been suggested that developing and simultaneously performing quality assurance during clinical trials of emerging technologies decreases safety errors [112]. Prospective analyses,

such as FMEA, could be a useful tool for emerging technologies [113], including conformal ion therapy for treating moving tumors [29]. Though several motion handling strategies with ion beams exist [114-117], few of these motion handling strategies are integrated into their beam delivery systems [38]. Relatively less is known about the safety risks of a modular motion-synchronized dose delivery system (M-DDS) for ion beam therapy [51], and no comprehensive assessment of the safety of a dose delivery system with integrated motion compensation has been reported in the scientific literature.

The purpose of this study was to apply an established method to analyze safety risks from a novel, modular, motion-synchronized dose delivery system for scanned ion beams. The system is in the late stages of preclinical development and testing. Here, we focused on the beam delivery process, identified potential motion-related errors, and implemented corresponding solutions. The performance of the M-DDS has been previously described by Lis *et al*. (2020). Where relevant, we developed and performed sample commissioning-style tests and quality assurance (QA) tests. These results provide information for subsequent clinical safety assessments of a novel, modular motion-synchronized dose delivery system in development.

4.2. Materials and Methods

This work describes a safety assessment of a dose delivery system (DDS) that is undergoing pre-clinical testing at two ion therapy centers. The M-DDS is an extended version of a clinical products used at the National Center for Oncological Hadrontherapy (CNAO) and MedAustron that have undergone full safety certification. The two most important extensions to the DDS were to make it portable and to allow for motion mitigation by synchronizing beam delivery to anatomical motion. The performance of the prototype motion-mitigation DDS was previously demonstrated, including preliminary tests such as the delivery of conformal, motion-synchronized beams [51]. These results focused on proof of

concept and the preliminary characterization of performance, but not safety. However, failures in the functionality of the M-DDS components could theoretically compromise patient safety. To minimize this risk, safety was integrated into each stage of development, in an effort to maintain the existing safety system for reintegration of the M-DDS into CNAO.

The assessment strategy described in this work applies an established methodology from AAPM Task Group 100 [103]. This strategy is a prospective risk analysis method that has been widely used in the medical and other industries. With this strategy, we first defined each step of the treatment process, in detail, with a process map. We then identified possible errors that could occur at each step and quantified the effect on patient treatment with an FMEA. Finally, we identified the causes of errors with a fault tree analysis (FTA). After determining the potential safety risks, we developed and tested solutions for these errors [103].

The prospective risk analysis was performed on a DDS, with integrated capabilities for target motion compensation [51]. For convenience, the general characteristics of the M-DDS are summarized here. The DDS was adapted from the DDS found at CNAO to function with the therapy research line (Cave M) at GSI Helmholtz Center for Heavy Ion Research (GSI). The DDS is composed of commercial field programmable gate arrays (FPGAs) (PXIe-1085; National Instruments, Austin, TX), which control each beam delivery component, including the scanning magnets, beam monitoring detectors, timing system, and interlock system. The DDS has been modified to synchronize the delivery of 4D-optimized plan libraries [29, 51] to detected target motion.

Motion mitigation features are integrated into the M-DDS. The first step of motion synchronized dose delivery is creating 4D treatment plan libraries from 4DCTs, where each plan in the library contains delivery information for a motion phase within the 4DCT. During beam delivery, a motion-monitoring device continuously monitors the tumor position, from

which the M-DDS determines the current motion phase [118, 119]. The delivery progresses in sequence until the tumor position has entered into another motion phase and delivery is redirected to the plan from the plan library that corresponds to the detected motion phase. Further information on the M-DDS is described by Lis *et al*. [51].

Good manufacturing practices were followed through the development of the M-DDS. Critical processes in the M-DDS were maintained from the clinical M-DDS design and all changes were evaluated experimentally in the clinical environment. The implemented software design choices were based on the existing software structure, so most uncovered sources of error were found to be related to unclear workflow and limitations to memory or signal speed. All changes and additions were documented. In the following sections, we describe a safety assessment strategy for the M-DDS. Additionally, we provide example safety and quality assurance tests for the M-DDS.

4.2.1 Process Steps

The first step of the prospective risk analysis was to identify the sub-processes that occur through the course of treatment with a process map. A process map is a visual representation of a process that demonstrates the flow of each step from start to end. We divided the process of treating a patient with scanned ion beams into 10 main stages, based on the guidelines proposed by the World Health Organization [120]. In this study, we focused on six of these stages - planning, simulation, patient setup, treatment delivery, treatment verification and monitoring - as these were the most relevant to treating moving targets. For each of these stages, we identified the sub-processes that occur at an ion beam therapy center [111], such as delivery of an iso-energy slice (IES) during the course of treatment. We then amended each stage to include any additional sub-processes when delivering motion-synchronized ion beams with the M-DDS, such as redirecting the plan delivery to compensate for detected motion. Modes of failure were then identified for each of these sub-processes.

4.2.2 Failure Modes and Effects Analysis

The FMEA assesses the likelihood and impact of failures from each step of a process. An FMEA was applied to each of the identified process steps and potential modes of failure at each step were described. Each of the failures were assigned a rank value on a numerical scale of 1 to 10 for each of three safety indices: the severity index (S) is the extent of harm of the failure on the patient, the occurrence index (O) is the likelihood that a cause will result in a failure, and the detection index (D) is the likelihood that a failure will not be detected. All three of these indices are estimated under the assumption that there was no safety check in place for that failure. The corresponding definitions for the rankings of each of these values are summarized in Table 4.1**.** This data has been adapted from the TG-100 [103]. The failures were then ranked by calculating the risk priority numbers (RPN), which is the product of these three indices (RPN = S × O × D). RPN values of above 125 were considered high risk, and any S score above 5 was also considered high risk. One example error is the gradual drift of the scanning magnet throughout the course of delivering an IES. This could potentially cause limited toxicities or overdose, as the drift may be on the scale of a few mm, and would potentially occur for every delivery in the absence of position feedback. Such an error would be difficult to detect without monitoring. The resulting RPN would then be 6 × 10 × 7 = 420. Selected FMEA indices were agreed on by a consensus group of experts, including the authors on this work.

4.2.3 Fault Tree Analysis

Causes of each identified failure were mapped out with a fault tree analysis (FTA). The FTA allows for visualizing potential points to perform quality management procedures and to minimize the propagation of errors [121]. Each failure mode was traced back to its potential causes using a logic tree. Possible failure modes include user errors, such as selecting the

wrong delivery setting or incorrect patient setup, software errors, equipment failures, and patient non-compliance. For the example of an error in delivery of an IES, the cause could be traced back to a faulty position feedback from the beamline monitors to correct the scanning magnet power supplies. Other causes of the error could also be postulated, including slow scan speeds and incorrect magnet calibration. Once causes for each failure were identified, methods to eliminate the cause or to detect the possibility of each failure were developed.

Table 4.1. Numerical scale used to assign rank values to Severity Index, Occurrence Index, and Detectability Index for each failure. This data has been adapted from the TG-100 report on FMEA. For each case, a rank of 1 was considered harmless, and a rank of 10 was catastrophic. Chosen rank values were based on observed or estimated.

Rank Value	Severity Index	Occurrence Index (Mean Time Between Failure)	Detectability Index
1	No effect on patient care	+ 4 years	Impossible to miss
2	Inconvenience or delay in care	2 years	“
3	“	1	Highly likely to notice
4	Minor dosimetric error	6 months	Easy to detect
5	“	1 month	Fairly easy to detect
6	Limited toxicity or overdose	2 weeks	Fairly difficult to detect
7	Potentially serious under- or overdose or toxicity	1 week	“
8	“	3 days	Nearly undetectable
9	Very serious under- or overdose or toxicity	1 day	“
10	Patient death	1 hour	Undetectable

4.2.4 Solutions and Tests

After identifying the potential solutions for the safety risks, appropriate solutions were implemented and error-handling tests were designed and performed. Solutions for failure modes can be classified into several categories: permanent corrective actions, error states and interlocks, commissioning and quality assurance tests, and plan verifications. Permanent

corrective actions are changes in the workflow of the planning or delivery software or user protocols in order to eliminate the possibility of that failure mode occurring. This can include implementing redundancies, such as redundant devices and communication protocols. Pass-fail tests were performed by simulating error states and checking that the delivery system entered an error state or triggered an interlock. Tests for proper exception or error handling are pass-fail safety checks that ensure error signals are sent to enter an error state, or to set an interlock when a runtime error occurs. Commissioning and QA tests are tests that verify that the system consistently works according to manufacturer specifications and within acceptable fault tolerances. Plan verification tests verify the accuracy of patient plans. For example, scan magnet position errors can be prevented in several redundant ways. Two position-monitoring chambers are used during delivery to monitor the accurate delivery of beam spots within an IES. Additionally, interlocks are in place in the case of failure of one of the monitoring or scanning magnets. Finally, daily QA is performed to confirm the functionality of the entire delivery system. Whenever possible, permanent corrective actions were implemented.

4.2.4.1. Description of Error Handling Tests

Error handling tests were created for each of the failures identified in the FTA. Pass-fail test cases were written for each of these failures. Corresponding software tests were then created that inject error scenarios into the delivery process to confirm that the DDS can respond to the respective error. In the case that an error-handling test failed, the underlying delivery software was modified to prevent the error from occurring. In other cases, an interlock was also implemented to trigger the interruption or termination of treatment in the presence of a motion synchronization error. The implemented interlocks were also tested by injecting error scenarios into the delivery process.

4.2.4.2. Daily, Weekly and Annual QA

The performance of the accelerator and beam delivery components was characterized through a series of quality assurance measurements. While existing QA protocols [101] will confirm the functionality of most aspects of motion-synchronized dose delivery, additional tests must still be performed to ensure the performance of additional features, including the motion monitoring system and 4D plan library. QA tests were designed that prioritized a simple set up, are multi-purpose, are fast and use well-characterized phantoms. A QA concept was designed to test the safety and reproducibility of motion-deliveries. Where possible, the current clinical protocols at ion therapy centers, such as those used at CNAO [35] were extended to include motion scenarios. Each test was verified experimentally in a clinical setting at CNAO.

Daily QA tests were designed and performed for measuring field uniformity, beam spot positions, and beam reproducibility. Set-ups with water-equivalent plastics (RW3 slab phantom; PTW, Freiburg, Germany) and radiochromic films (EBT3 Gafchromic; International Specialty Products, Wayne, NJ) were selected, as their assembly time is fast and they are both well-characterized systems. The daily QA procedures found at CNAO were modified and applied to test the delivery quality of motion compensation with the M-DDS. This allowed faster delivery that was not dependent on additional custom made software for analysis. The daily QA setup, a radiochromic film, mounted behind 2 cm of water-equivalent plastic, was mounted on top of a linear stage with programmable motion patterns (M-414.2PD; Physik Instrumente GmbH, Karlsruhe, Germany). Motion amplitudes, detected from an optical laser distance sensor (OD100 − 35P840; SICK, Waldkirch, Germany), were converted into motion states [51]. For each test, the clinical (non-moving) procedure was performed first, followed by the motion-compensation variant. For these beam deliveries, the linear stage moved with 20 mm amplitude sinusoidal or Lujan2 motion [122] while

delivering a uniform square profile with eight surrounding spots. The purpose of each test and the measurement criteria are summarized in Table 4.2.

All films were calibrated in a series of steps. Before the QA tests, standard dosimetry was performed [41], and calibration films, composed of eight squares with fluences from 2 × 105 to 4 × 107 particles/mm, were acquired for each batch of films. The calibration plan was delivered with 280 MeV/u carbon ions to films placed behind 2 cm of water-equivalent plastic. After delivery, the QA films were scanned with a laser film scanner (VIDAR DosimetryPRO Advantage Red; VIDAR System Corporation, Herndon, VA, USA) in landscape orientation, using 16 bit sampling and a 300 dpi resolution. A batch-specific optical density correction was applied to each film by subtracting out the optical density of an unirradiated area of the film, using an image analysis software (ImageJ version 1.52a; National Institute of Health, Bethesda, MD). The calibration films were used to apply a calibration curve, converting optical density to particle intensities. Each film was cropped, aligned, and corrected for linear energy transfer (LET) quenching effects [42], by applying a relative efficiency (RE) correction curve as follows:

$$\mathrm{RE(LET)} = \frac{\mathrm{D_{280MeV/u}(netOD)}}{\mathrm{D_{abs}}}$$

where D280MeV/u(netOD) is the 280 MeV/u carbon ion dose needed to produce the measured, corrected optical density, and Dabs is the actual dose delivered with carbon ions to the film. After, calibration, the films were analyzed.

The uniformity was assessed through the homogeneity index (HI), which is defined as

$$\mathrm{HI} = 100 - \frac{\mathrm{D_{max}} - \mathrm{D_{min}}}{\mathrm{D_p}}$$

where D_{max} and D_{min} are the maximum and minimum measured absorbed dose, respectively, and D_p is the prescribed dose. The HI was measured in the center 70 % of the target volume. HI values above 90 % were considered clinically acceptable. Additionally, the beam spot

position accuracy was assessed by measuring the relative distance between each pair of beam spots in 2D profiles of the films. The beam spot shape and distortion was measured by determining the FWHM in the horizontal and vertical directions. Beam reproducibility tests were performed by comparing the delivery results across several weeks with a coefficient of variation [123]. Finally, the increases to QA delivery time were assessed by measuring the setup and delivery time for each test and estimating the increased time for QA, when performing motion-specific testing alongside the currently performed QA tests in each treatment room.

Table 4.2. Description of the purpose and pass criteria for each quality assurance test.

Test type	**Quantity tested**	**Pass criteria**
Daily QA		
Field uniformity	Homogeneity index [124]	≥ 95 %
Spot shape	FWHM in X and Y direction across scan field [101]	Symmetrical
Spot position	Distance to agreement [34]	< ± 1 mm
Motion-monitoring system functionality	Function test	Functioning
Weekly QA		
Beam monitor calibration reproducibility	Coefficient of variation [123]	< 1 %
Annual QA		
Dose distribution with homogeneous phantom	Percent error from expected dose [35]	< 5 %
Dose distribution with heterogeneous phantom	Percent error from expected dose [35]	< 5 %
QC		
Motion-monitoring system performance	Distance to agreement [34]	< 0.1 mm

Equipment quality control (QC) is generally also performed daily to verify the functionality and accuracy of treatment equipment. To verify the performance accuracy of the

motion-monitoring equipment (a linear stage and an optical distance (OD) laser) the linear stage was programmed to move in an increasing stepwise motion pattern, as seen in Figure 4.6. The measured OD laser signal was compared to the motion files for the linear stage.

Annual QA is a series of extensive tests to measure machine performance. Annual QA tests were performed to measure dose distributions with 3D homogenous setup and a 3D inhomogeneous setup. First, 4DCTs of an heterogenous phantom (CIRS 062 electron density phantom; CIRS, Norfolk, VA, USA) and a water tank (MP3-P; PTW, Freiburg, Germany) were acquired. $60 \times 60 \times 60$ mm^3 cubes were delivered to 12 small-sized ionization chambers (PinPoint 3D ion chamber model T31015; PTW, Freiburg, Germany) in a water tank for both setups. For the 3D inhomogeneous setup, density compensation measurements were performed by the heterogeneous phantom mounted in front of the water tank. Both deliveries were performed without motion, and with motion compensation. Standard deviations for measured doses of < 5 % were considered acceptable.

4.2.4.3. Patient Plan Verification

Plan verification, or patient specific quality assurance (PSQA), is performed to assure the accuracy of a treatment plan. Treatment planning and treatment delivery errors, unique to the motion mitigation system, can be discovered through PSQA testing. Errors may include selecting the wrong motion trajectories during planning or delivery, or planning with an inintended motion compensation strategy. If not detected, these could lead to severe dose degradations. Several plan verification methods were chosen to test the extent to which planning errors related to mitigating for respiratory motion can be detected. The chosen PSQA tests included patient verification protocols that are used in ion therapy clinics, including 1) 3D dose measurements with small-sized ICs, 2) repeat 2D measurements at several depths with a 2D ionization chamber array detector (Octavius 1500 XDR; PTW, Freiburg, Germany), and 3) log file analysis. Additionally, 3D measurements were also

performed with 4) a stack of radiochromic films [125]. These measurements were analyzed with standard deviation calculations, gamma index analysis, and through the evaluation of dose volume histogram (DVH) metrics, respectively. To perform these measurements, the detector or film was placed into its respective holder, and the holder was mounted onto a linear stage. 4D-optimized patient plan libraries were created and delivered to each detector setup. The linear stage was programmed to move with trajectories derived from the patient 4DCTs. Other aspects of PSQA were also considered when designing each setup, including favoring simpler phantom setup process and the resolution of the recorded data.

3D dose measurements were performed by delivering patient plans to 12 small-sized ICs. These ICs were selected, as they are used in several clinical ion facilities for patient verification [126-128]. The ICs were inserted into a custom removable holder, connected to a linear stage that generated the motion of the ICs (Figure 4.1). The linear stage was mounted on top of a water tank, similar to the commercially used water tank phantoms, and the water tank was filled with water. Each patient plan was delivered to this phantom, with the linear stage moving with the patient's breathing pattern. Each IC recorded a dose measurement and standard deviations were calculated from these doses. The chosen prescription dose was 6 Gy per fraction. Standard deviations of < 5 % are typically considered acceptable.

2D dose measurements were performed by delivering the patient plan to a 2D ionization chamber array detector at three tumor depths. The chosen depths corresponded to the proximal end, middle, and distal end of the tumor depth. The appropriate thickness of water equivalent plastic (RW3; LAP GmbH, Lüneburg, Germany) was placed in front of the detector for each case. This setup was mounted on the linear stage to generate patient motion and a patient plan was delivered to the detector with and without motion, as seen in Figure 4.2. The delivery results were compared to the planned doses for each depth with the gamma index analysis [34], where a criterion of 3 % / 3 mm was used, with a dose thershold of 5 %

of the prescription dose. Pass rates of > 90 % for measurements made at all three depths were considered passing.

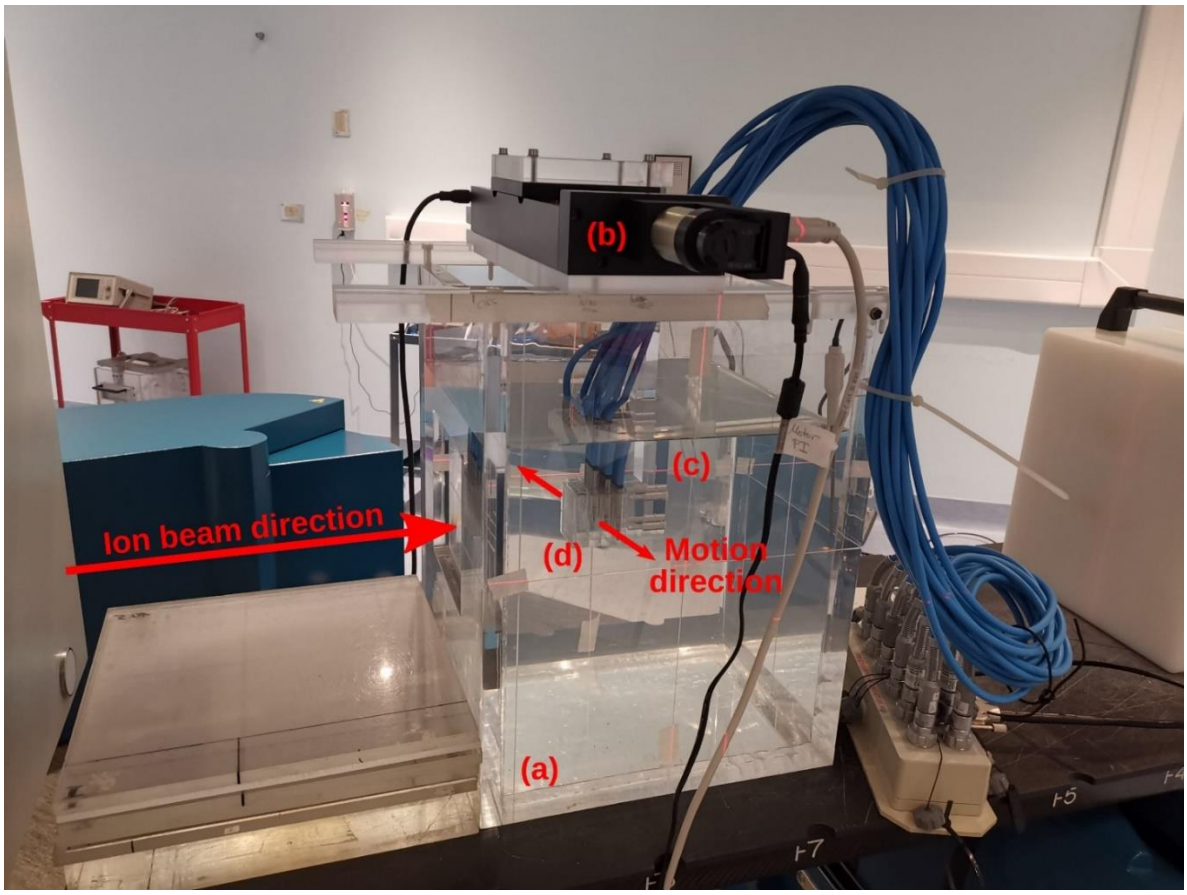

Figure 4.1. Experimental setup for patient-specific quality assurance (PSQA) measurements with a) a water tank and b) a linear stage mounted on top. The linear stage is programmed to move a variety of attachments in periodic, respiratory-like motion patterns. Here, c) a holder with d) 12 small-sized ionization chambers (IC) inserted inside is attached. This IC holder aligns with the isocenter markings on the water tank phantom, which is filled with water.

3D measurements with a stack of films were made to acquire higher resolution dose distributions. Seven 5" × 4" radiochromic films were slotted into an in-house built film holder phantom. The phantom was composed of a stack of 15 × 13 × 1 cm^3 polymethylmethacrylate (PMMA) plastic slabs, with slits for the films, as seen in the technical drawing in Figure 4.3. This setup was mounted on top of the linear stage, which generated periodic motion. Each film was numbered and labelled at the top right corner before delivery. The patient plan was delivered to the film stacks, in the presence and absence

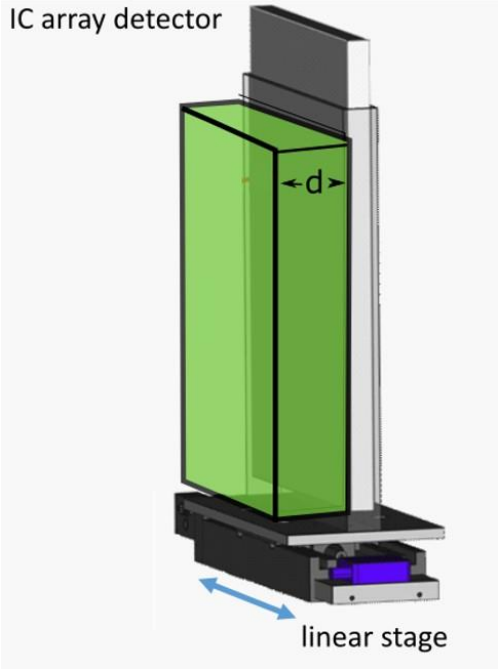

Figure 4.2. Schematic of the IC detector array setup. The IC array detector is placed inside of a 5 mm PMMA holder, mounted onto a linear stage. Water-equivalent plastic of thickness 'd', corresponding to the distal, middle or proximal depths of a target, are then placed in front of the detector.

of motion. Calibration films, composed of eight squares with fluences from 2×10^5 to 4×10^7 particles/s, were acquired on the same day. After delivery, the films were processed as described in section 4.2.4.2. Each film was then analyzed with the gamma index analysis. The average gamma index pass rates for each film stack were evaluated using an in-house developed research software for data analysis, ArrayParser, where each film was compared to the respective treatment plan at the appropriate tumor depth. Gamma index pass rates of above 90 % were considered clinically acceptable.

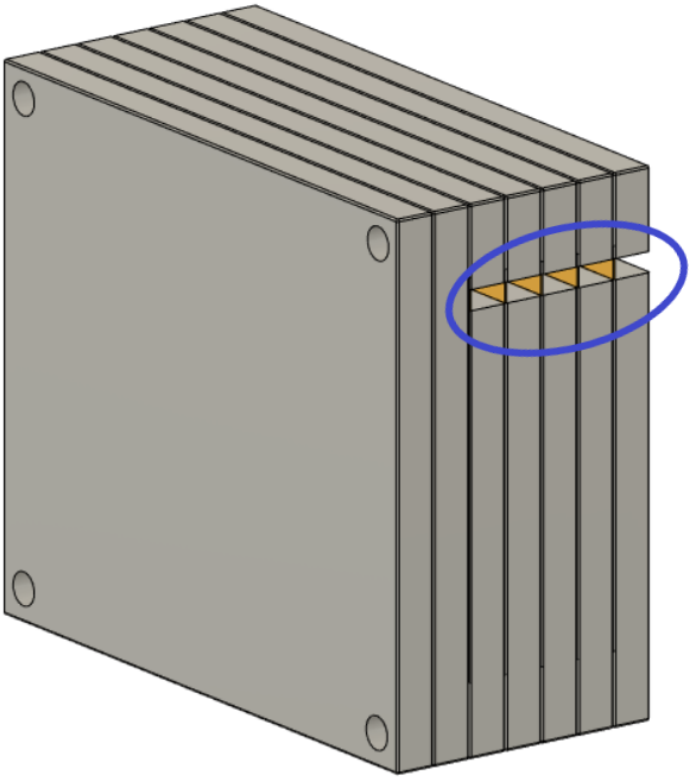

Figure 4.3. Schematic of the film stack. The film stack contains up to nine slabs of PMMA with precisely machined slots for holding radiochromic films (5" × 4") as well as several slabs of additional PMMA to vary the delivery depth. The phantom measures 15 × 13 × 9 cm^3 when nine slabs are in place. The slabs are aligned and held together by plastic screws at each corner of the phantom. The lateral cutouts (blue circle) are used for easy access of the irradiated films (yellow) without the need to disassemble the film stack phantom.

Log file analysis has been used to decrease PSQA measurement time. The patient plan was delivered to the IC array detector and log files from the scanner magnets and nozzle detectors were used to reconstruct the delivered doses on the planning 4DCT, using TRiP4D [51]. The motion signal from the linear stage was used directing plan delivery during motion-compensation. However, a simulated motion signal could also be used for these measurements. The dose reconstructions were then compared with planned dose distributions using the gamma index analysis to a criterion of 3 % / 3 mm, where > 90 % pass rates were considered acceptable.

4.3. Results

4.3.1 Process Map

A process map was created to map out the sub-processes of patient treatment at a typical ion therapy center. The processes for moving tumors are presented in Figure 4.4. This map consists of five main workflow steps, starting with patient imaging through the last fraction of treatment delivery. Patient-specific verification procedures were included as well. Several of these steps were critical to patient errors.

Steps	Imaging	Treatment Planning	Plan verification	Initial treatment	Subsequent treatments
Purpose	• Obtain internal anatomy info. • Monitor breathing • Localize anatomy to isocenter	• Create plan library	• Assessment of plan in phantom • Assessment of motion information accuracy	• Dose delivery to patient	• Deliver remaining fractions
Steps	• Patient data into database • Immobilization • Align patient • Record position • Place markers • Coach breathing • Monitor motion • Acquire images • assess images • Transfer images	• Specify images with target • Create ROIs • Edit for artifacts • Construct PTV with margins • Fuse images • Enter planning constraints • Setup dose calculation parameters, fields and beams • Calculate and optimize dose and robustness • Evaluate plan • Specify treatment course	• Simulate dose in water phantom • Setup phantom to isocenter • Setup motion monitoring device • Load plan and motion file • Deliver plan • Compare outcome to plan • Reconstruct log files • Compare reconstruction to plan	• Position and immobilize patient • Setup markers • Position motion monitoring device • Setup breathing aids • Document • Begin treatment delivery • Synchronized motion management • Fast beam gating • Online beam monitoring • Delivered data recording	• Note treatment changes and correct • Scheduling • Re-image anatomy • Re-plan for anatomy changes and respiratory changes • Documentation
Outcomes	• 4DCT • Motion file	• Robust 4D-optimized treatment plan library	• Plan library accuracy confirmed	• Delivery and motion data recorded into file • Single fraction delivered	• Treatment complete

Figure 4.4. Process map for motion-synchronized dose delivery as commonly found in ion therapy clinics. The treatment process is broken down into five categories: imaging, treatment planning, plan verification, initial treatment fraction and subsequent treatments. Each step in these processes is described.

Table 4.3. Summary of FMEA results for potential errors during patient therapy with motion-synchronized ion beams using a DDS with integrated motion compensation controls. RPNs of over 125 were considered high risk.

Failure mode	**Severity**	**Occurrence**	**Detectability**	**RPN**
Patient movement	7	6	7	294
Absolute change in breathing position	6	7	7	294
Patient alignment	7	5	6	210
No gating during sporadic movements	5	5	8	200
Gating window too large	6	8	4	192
Beam sweeping distance dose	3	8	9	192
Sending incorrect motion phase info	7	3	7	147
Error creating of slice files	7	3	7	147
Failure to gate	9	2	8	144
Position calibration incorrect	8	2	7	112
Changes to respiration pattern	7	8	2	112
Setup of motion management device to wrong position	9	2	6	108
Patient not re-imaged after anatomy change	7	3	5	105
Position feedback missing/not working	4	5	5	100
Determined wrong number of motion phases	6	2	5	90
Incorrect motion direction	9	2	5	90
Loading wrong treatment plan	4	2	10	80
Motion data recording stops	4	2	9	72
Failure to progress to next slice	6	2	5	60
Plan incomplete	6	2	5	60
Motion signal loss	9	2	3	54

4.3.2 Failure Modes and Effects Analysis

A systematic evaluation of the process map identified 58 failures. A subset of these failures is shown in Table 4.3, including the highest ranked failures during treatment delivery. Values for S, O and D indices were estimated based on the metrics from Table 4.1 and were used as a guide to determine the highest risks for conformal, motion-synchronized therapy. All failures with an RPN of 125 or greater and all failures with a severity > 5 were considered

in this study. In total, 41% of failures were identified to be low risk (RPN = 1 - 75), 33 % were found to be medium risk (RPN = 76 - 125) and 26 % were found to be high risk (RPN > 125). The highest ranked failures, with an RPN score of 294 were caused by delivery errors due to patient movement and absolute changes to breathing position. Potential failures that are common to both static site and moving site treatments were not included in the analysis, such as miscommunications between physicians and technicians and certain treatment planning errors.

4.3.3 Fault Tree Analysis

Fault tree analysis was performed to identify sources for the potential errors identified in the FMEA. Solutions for each error in the FMEA were identified, implemented and tested. A sample fault tree can be seen in Figure 4.5 for the case of gating magnet failure. Identified causes of error included human error, such as setting the treatment to the wrong delivery mode, machine errors, such as noise on the motion signal, and treatment errors, such as changes to the breathing patterns between image acquisition and treatment. Proposed solutions for these errors varied for each error type, and included disabling the option for gating when a 4D plan library is loaded, implementing a noise reduction filter on the motion signal, and using a monitoring method that compares planned to measured motion and gates delivery when out of range. Following implementation, the solutions to the identified errors were tested.

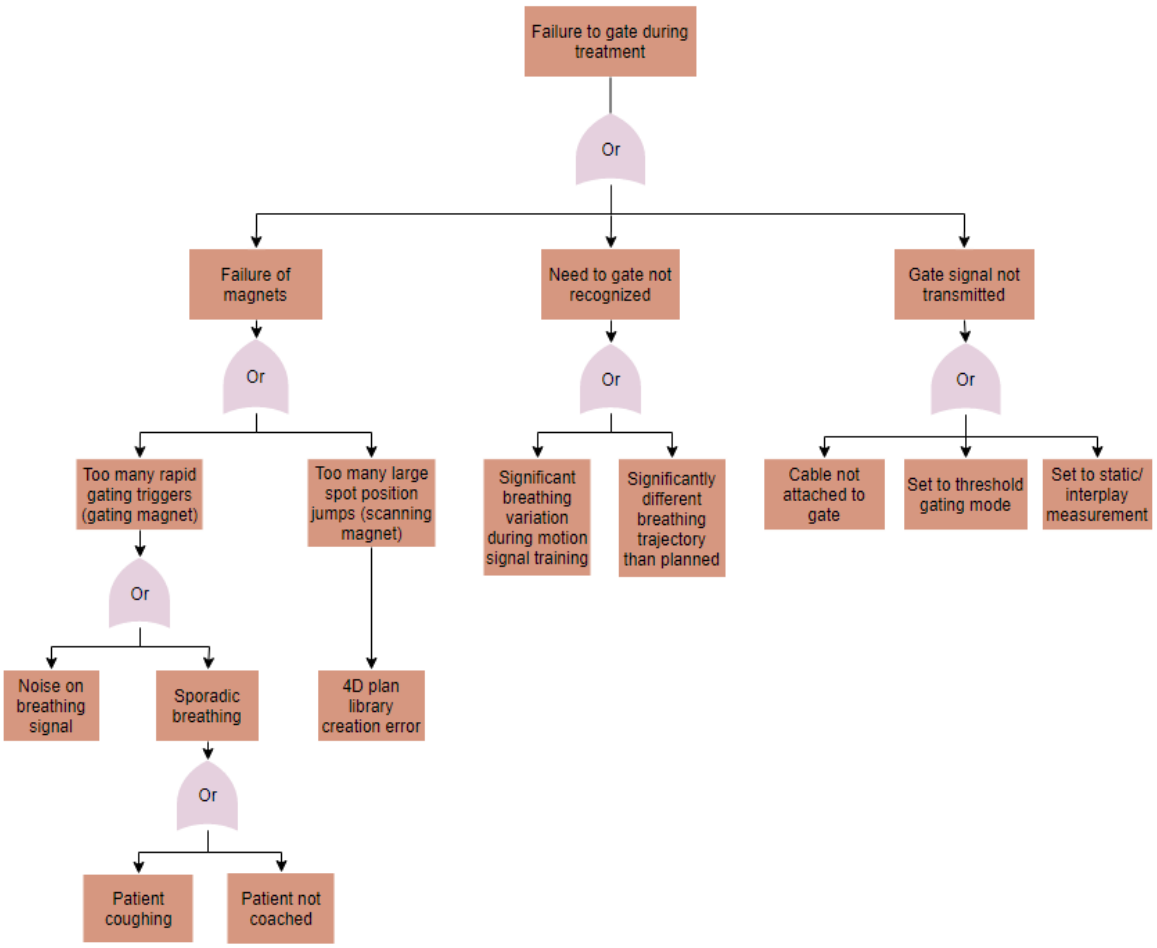

Figure 4.5. A fault tree analysis for the case of gating failures during motion-synchronized dose deliveries.

4.3.4 Safety Testing

Solutions were implemented to prevent the identified errors from occurring and each solution was tested. The implemented permanent corrective actions included noise filtering to smoothen the respiratory signal, automatic extraction and setting of the number of motion phases from the treatment plan library, and implementing a checkpoint to prevent the beginning of delivery until the motion-monitoring system is calibrated and sending a motion phase. Many errors were identified to be due to mistakes made by the user. Some examples include setting up the motion-monitoring system in an orientation other than what was used during planning image acquisition, and not accounting for changes to the tumor position, relative to isocenter [129]. In these cases, the proposed solutions included performing a

second check by another clinician or reimaging the patient periodically. Additionally, using a checklist to check the patient setup before treatment could reduce the incidence of user errors.

4.3.4.1. Pass Fail Tests

A series of error handling tests were created to test each of the implemented solutions. These tests included pass-fail tests, where the expected results included either triggering a temporary interlock, aborting treatment, or entering the "setup error" state. The summary of pass-fail test results are listed in Table 4.4.

Table 4.4. Summary of pass-fail tests and results.

Error	**Expected action**	**Result**
Incorrect plan library structure		
Wrong number of beam spots in plan library	Setup error state	Passed
Missing motion information in plan header	"	"
Particle numbers below or above limitations	"	"
Plan library larger than size limitations	"	"
Beam delivery errors		
Motion signal lost	Beam aborted	"
Motion trajectory deviating from expected trajectory	Temporary gate	"
Scanning magnet failure	Interlock	"
Gating magnet failure	"	"
Delivery of a beam spot skipped	Treatment is halted	"
MMD file recording error	Treatment stops, errors message, and file dump	"
Treatment stops prematurely	Delivery data recorded	"
Motion calibration incomplete before delivery starts	Beam gate activated	"
Treatment setup errors		
Wrong motion compensation strategy selected	Set automatically from plan	"
Motion system not fully set up or not on	Delivery cannot start	"

4.3.4.2. Daily, Monthly, Annual QA

QA tests were proposed for identifying errors in the functionality of the motion-synchronized delivery components. These tests are summarized in Table 4.2. QA setups were chosen that are available or are similar to those found in ion therapy centers. Delivered profiles were analyzed for uniformity, agreement with the treatment plan, and for beam reproducibility, the uniformity index and gamma index analysis were chosen as analysis metrics.

Delivery uniformity with motion-compensation was determined by assessing a square profile for a single energy of 240 MeV/u, delivered with motion-compensation, to a radiochromic film. HI for the static and 10 phase compensation deliveries were 95.3 % and 94.8 %, respectively. The spot position accuracy was found to be within ± 0.5 mm from the expected position. The beam spot shape was determined through a measurement of the FWHM in the X- and Y- directions, where the X-direction was the direction of motion. For static deliveries, this was found to be 3.9 mm and 3.4 mm, respectively, and for the 10 phase deliveries, this was found to be 4.7 mm and 3.3 mm, respectively. The observed broadening of the beam in motion direction is an indication of the residual motion both within and between the motion phases, and spot size increases of up to ± 0.5 mm were tolerated.

The increased time to perform the QA tests was measured and compared to static QA alone. For the current clinical QA procedures, setup and irradiation time was found to be 5 minutes and 3 minutes, respectively, and for the motion compensation QA, the setup and irradiation time was found to be 5 minutes and 10 minutes, respectively. The estimated increase in QA-personnel time for a facility with three treatment rooms is $3 \times 7 = 21$ minutes, based on current QA methods and experience.

Annual QA tests included measuring 3D uniformity in a homogeneous and heterogeneous phantom. The static cube delivery measured a homogeneity of ± 1.2 % and the

motion compensated delivery measured a homogeneity of ± 3.5 %. The static cube delivery of 10 Gy, through the heterogeneous phantom, measured a homogeneity of ± 2.1 % and the motion compensated delivery measured a homogeneity of ± 2.3 %.

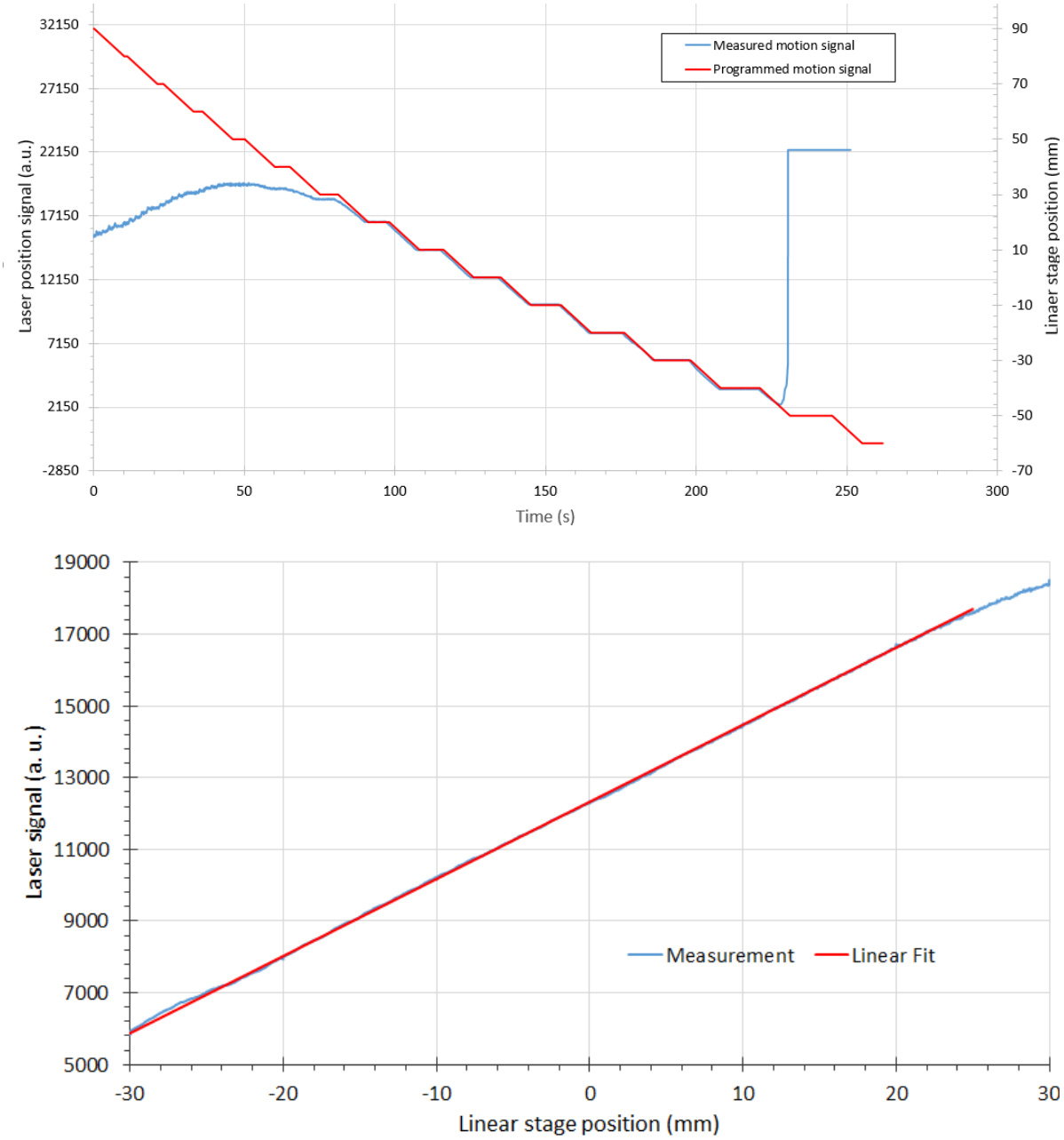

Figure 4.6. a) Correlation of motion position to the measured signal of the motion-monitoring device (an optical distance laser sensor) for a step-wise motion pattern. The motion positions, in mm, (red) are uploaded onto the linear stage as a motion file and used to move the linear stage. The motion-monitoring device then records the relative displacement (blue) as an analog signal. The left and right portions of the motion signal show where the motion-monitoring device is out of signal range. b) A plot of position accuracy between the optical distance laser signal (in arbitrary units) and the linear stage position (in mm).

The basic functions and accuracy of the motion-monitoring equipment were also determined. The measured motion was within ± 0.5 mm for all steps within the measurement range of -30 mm to 20 mm, as seen in Figure 6a. The agreement between the programmed linear stage positions and measured positions from the distance sensor are seen in Figure 6b, where the linear relationship indicates a high degree of measurement accuracy.

4.3.4.3. Patient Specific QA Results

Patient plan verification tests were performed to compare the measured accuracy of the delivered 4D plan libraries. Patient verification deliveries were all found to be within clinical requirements; however, the measurement resolution varied for each approach. Results are summarized in Table 4.5. The small-sized IC measurements were found to be within ± 2.4 % and ± 8.9 % of the prescription dose for static deliveries and 10 phase motion compensation deliveries, respectively, where ± 5% is ideal, but due to residual motion, ± 10 % was considered acceptable at this stage; however, higher precision may be necessary before clinical use. The measurements at three depths, with an ionization chamber array detector were assessed using the gamma index analysis. As only the distal measurement did not meet the pass criteria, log file analysis was performed to verify delivery quality. Pass rates (Pearson correlation score) for the motion-compensated delivery were found to be 91.6 % (0.9901), 98.6 % (0.9954), 90.9% (0.9971) for distal, middle and proximal profiles, respectively. The average gamma index pass rates for the film stacks were 92.4 %, and 90.4 % for conventional 4D optimized and robust 4D optimized deliveries, respectively. The average pass rate for the static delivery was 92.2 %. The homogeneity for robustly optimized and conventionally optimized 10 phase motion compensated deliveries was 90.6 % and 92.4 %, respectively. Delivered dose data (DDD) log files were reconstructed and compared to planning simulations. The gamma pass rates were found to be 99.4 % and 96.0 % for static and motion-compensated deliveries, respectively. The measured motion signals were used to

reconstruct the delivered beam spot position. The comparability of the data for each setup was limited by the lack of direct correlation between analysis methods [50]. The small-sized IC and film stack phantoms were found to have a relatively fast setup and execution. Due to the limited number of detectors, small-sized IC measurements provided less information in cases where results were nearly passing. In those cases, DDD dose reconstructions were necessary to determine the dose distributions. 2D dose measurements with the IC array detector took multiple times longer to deliver than the film stack and small-sized IC measurements, due to the multiple measurements at varying depths.

Each PSQA method was also assessed for the ability to detect motion-specific planning and setup errors. Errors in positioning and orientation of the motion-monitoring system were visible for all PSQA methods, but were least apparent in the film stack deliveries. Selection of the wrong number of motion phases were only visible in log file reconstruction and films, but had little impact on the delivery results. Delivering a few beam spots to the wrong positions, not delivering a few beam spots and using the wrong motion file during planning were both only visible in the log file reconstructions, but there were no measurable changes to the treatment delivery quality. Finally, selecting the incorrect motion compensation strategy was visible on film stack images and IC detector array measurements but was not immediately clear without log file reconstructions. Log file reconstructions were quicker than other methods, due to requiring no phantom setup time. Likewise, log file analysis, and to some extent, film analysis, did not require precise positioning. IC array detector measurements took nearly three times as long as small-sized IC measurements, but provided a higher number of measurement points. In both cases, measurement analysis programs are available to assess plan accuracy. Films require additional time for digitizing and show a non-linear dose response. Calibrating the dose response of a film requires considerable effort before it can be used for QA measurements.

Table 4.5. Summary of patient specific quality assurance results for four measurements. These measurements included calculating 3D dose measurement agreement with 12 small-sized ionization chambers (IC), and calculating gamma index analysis pass rates for comparisons between log file reconstructions and treatment plans as well as IC array detector measurements. Acceptable criteria and analysis results are summarized.

QA test	**Metric (pass criteria)**		**Static results**	**Motion mitigation results**
Pinpoints	Dose deviation (± 5 %)		± 2.4 %	± 8.9 %
Log files (planned to reconstructed)	Gamma index analysis (> 90 %)		99.4 %	96.0 %
Film stacks	Gamma index analysis (> 90 %)		92.4 %	90.4 %
IC detector to log file reconstructions	Gamma index analysis (> 90 %)	Distal	84.1 % (0.9883)	91.6 % (0.9901)
		Middle	100.0 % (0.9947)	98.6 % (0.9954)
		proximal	99.4 % (0.9983)	90.9% (0.9971)

4.4. Discussion

We have designed and tested a prospective risk analysis strategy for the motion-synchronized dose delivery system, developed for scanned ion beam therapy of moving targets. We created this strategy specifically to assess the safety of the motion mitigation portion of the DDS for its eventual use in the clinic. Additionally, we have implemented and tested solutions for possible errors related to motion mitigation. The major finding of this study is that we have identified the sources of and solutions to major errors with a comprehensive risk assessment strategy. We also obtained pre-clinical test results that suggest the clinical reliability in motion-synchronized dose delivery. The results of this study have determined that the proposed safety assessment tests can be utilized at ion therapy centers, which operate with the modular M-DDS.

The implication of this study is that the described comprehensive risk analysis strategy and proposed tests can serve as an example during initial safety, commissioning, and QA tests leading to implementation of the M-DDS into clinical use. This assessment is part of

a larger effort to confirm and maintain the clinical safety of the M-DDS from the design stage through clinical implementation. The M-DDS has been implemented following good manufacturing practices, including testing at several stages and maintaining extensive documentation. The described preliminary safety tests suggest that the M-DDS is safe, reliable, and ready for additional tests, leading to eventually treating patients. Further, the proposed error tests and QA tests could be performed within clinically reasonable timeframes. The safety tests are not the final solution for commissioning and QA procedures within the clinic, but rather are an example of a general safety strategy for the M-DDS, which can be modified and extended to meet the specific needs of a particular clinic. Full acceptance testing and commissioning will be performed before re-implementing the modified DDS into the clinic.

This is the first implementation of a comprehensive, prospective safety assessment for pre-clinical testing of a motion-synchronized dose delivery system. The results of this study are coherent with the recommendations found in the TG-100 and other AAPM reports [92, 96, 101, 103, 130]. All plan verification and QA tests were within clinical specifications. Log file analysis provided the additional benefit of recognizing individual beam spot errors and indicating other errors during treatment preparation that could otherwise be unnoticed and should be performed alone or along with regular plan verification.

Several studies have applied the safety assessment protocols presented in TG-100 to ion therapy [111, 131]. To our knowledge, no studies have been performed to apply this approach to new technologies in ion therapy, including motion mitigation systems. Additionally, several studies have assessed the practicality of QA procedures. One study, by Hara *et al*. [86], describes a plan verification procedure for moving tumors. This strategy involves delivering patient plans to a 2D IC at three depths, and performing gamma analysis on each measurement. This study also concluded that this procedure is a beneficial QA

procedure for moving tumors. Another study [132] described the process of plan verification with small-sized IC deliveries. The procedure and phantoms were modified in our study for motion compensation. Further, Matter *et al*. [133] investigated the capabilities of various plan verification procedures to ensure the integrity of treatment plans under a variety of planning errors. Of the measured errors, two cases were relevant considerations for motion-synchronized deliveries with the M-DDS: the 'all spots shifted randomly' case, and the 'increase in spot weights' case. In particular, residual motion within a motion phase can be as high as 1-2 mm, and is accounted for in planning margins. In contrast, small increases in spot weights may be possible when the beam is frequently gated or when there are frequent jumps in the scan position due to non-optimally created plans can result in non-trivial increases to the integral dose. As such, we conclude that log file analysis could provide a supplement to plan verification measurements. This study did not consider failures associated with using real-time imaging to monitor target motion. This is a vital part of motion-mitigation and will be investigated in future studies. Though a variety of imaging techniques and motion monitoring devices can be integrated with the M-DDS, additional risk analysis must be performed to identify and mitigate for failures associated with these devices.

Our study has several strengths. One is that this method is based on established methods (e.g., FMEA, FTA) that have been applied in clinics worldwide. It can be extended to any modular device with integrated motion mitigation strategies. Yet, it allows for identifying errors that may specifically occur when using motion synchronized delivery devices. Further, the strategy uses the official risk assessment proposed by the AAPM, can be applied to any motion-synchronized dose delivery implementation, and to any clinic that integrates the described M-DDS to their treatment systems. This strategy is a well-developed, well-known, and comprehensive risk analysis strategy. Though clinic-specific modifications will need to be made, the described approach can provide insight into potential

complications, which could arise with the M-DDS. Finally, the presented quality assurance tests were designed with phantoms that are regularly found in proton and ion therapy clinics. These tests were performed at an ion therapy center (CNAO) under clinical conditions, with interlocks in place. QA and most PSQA tests were also performed at CNAO and GSI, except the film stack analysis, which was only performed at GSI.

One limitation of this study is that all safety procedures were tested with a predefined, 1D movement, generated by a motion-phantom. The motion patterns were well known and in complete agreement between the measured and actual motion. This is not a major limitation, as the delivery results with irregular motion will be characterized in future studies. Another limitation of this study is that no high-precision 3D dose distributions could be measured. 3D gels could potentially provide nearly instantaneous 3D dose distribution information. Gels produced by Maryanski *et al*. [134], which are readout with optical CT have recently been developed for 3D dosimetry of carbon ions. However, this strategy is still in the early stages of testing and has only been optimized for high doses for carbon ions. Another dosimeter for high precision 3D dose measurements would be measurements with a 2D IC array detector in a water tank phantom [135, 136]. Though this strategy automatically provides high-resolution 3D dose information, this strategy requires delivering prohibitively long times for patient specific QA and assumes no phase dependence for motion-compensated deliveries; therefore, this method is better suited for beam commissioning. Another limitation of this study is that no independent dose calculations, such as Monte Carlo (MC) based dose calculations, were performed. However, this is not a major limitation, as MC dose calculations are typically time consuming; therefore, they are currently mainly performed to verify dose distributions when patient QA measurements do not pass. Additionally, the proposed patient verification methods are example solutions, and each clinic should select their appropriate plan verification method. Finally, MC performed at CNAO showed that MC simulations are

sensitive to input conditions and simplifications to the MC models [137]. Nevertheless, MC verification of patient plans has been growing in popularity and can serve as a powerful tool for independent dose calculation on well-characterized data sets.

The M-DDS is substantially complete and the current version has been transferred back to CNAO for use in the research room there. Additional features are still in development that aim to handle irregular respiratory scenarios and other complications related to respiration; these will be completed before the M-DDS is implemented for clinical use. Additionally, interoperability with other centers and full compatibility to DICOM and I-HERO standards will be implemented, along with any necessary regulatory approvals for human use, followed by a full clinical commissioning. Before clinical use, the plan library structure must also be implemented into commercial treatment planning systems.

4.5. Conclusion

We have applied a comprehensive safety assessment strategy for the motion-synchronized portion of the dose delivery system. This work has shown that M-DDS is a clinically viable motion compensation strategy. The efficacy of possible QA procedures for motion-synchronized deliveries have been confirmed. Importantly, this strategy is specific to the motion-synchronized dose delivery system, but not to a specific clinic. Therefore, the presented methods can be adapted to other facilities using the M-DDS.

Chapter 5. Dosimetric Validation of a Modular System to Treat Moving Tumors Using Motion-synchronized Scanned Ion Beams

5.1. Introduction

Proton and ion therapy provide conformal dose distributions for static targets, and in the past few decades, have emerged as a formidable alternative to photon therapy. Ion therapies have mainly been used to treat static tumors, including several in the regions of the head and neck, cranium, retina, and the spine, with high conformity [43, 138], resulting in reduced toxicities and tumor recurrence [6]. Conformal treatments have been shown to be partially effective in reducing complications associated with radiotherapy of moving tumors, such as non-small cell lung cancer (NSCLC), including pneumonitis and cardiac complications [139, 140]. However, contemporary ion beam therapies for thoracic tumors still have high complication rates and low survival rates [141]. Additional unmet clinical needs include shorter treatment times and streamlined patient-specific quality assurance procedures. Thus, it is imperative to develop treatment methods that can meet these clinical needs.

Currently, about two thirds of proton and ion therapy centers use relatively simple motion mitigation strategies to treat moving tumors, including various combinations of techniques such as breath hold, beam gating, and internal target volumes (ITV), used with or without rescanning [116]. These motion mitigation strategies for scanned ion therapy have successfully eradicated some, but not all, moving tumors, yet treatment complication rates remain a serious problem [142, 143]. The local failures are largely believed to be caused by insufficient dose to the tumor and complications are believed to be caused by excessive dose to surrounding healthy tissues [144]. An obvious approach to overcome these limitations is to amend treatment planning and dose delivery methods to increase tumor coverage and reduce dose to normal tissues. To achieve these, improvements are needed to mitigate against range variations that are induced by moving heterogenous anatomy, including cases where the

movements of the tumor and surrounding healthy tissue differ from one another. The most advanced motion mitigation approach currently in clinical use, namely the phase-controlled rescanning method at the National Institute of Radiological Sciences (NIRS), combines rapid beam delivery with fluoroscopy-guided beam gating. This requires minimal changes to the target position during the time where the treatment unit actively delivers beam to the tumor. With this approach, treatments must be halted if tumor motion changes substantially from the expected tumor location [145]. The advantage of the gating approach is that it avoids the technical complexity of motion mitigation, but increases the compliance requirements of patients, and some patients cannot comply with respiratory requirements. The most technologically advanced approach, commonly called 4D-optimized tracking, allows the patient to breath freely and requires the treatment system to modify the trajectories of the delivered ion beams to follow the moving tumor, using real-time monitoring of the tumor position. This approach, developed at GSI for more than a decade [14], revealed promising dosimetric qualities and technical feasibility, but its vast technological complexity required to compensate anatomical motion has thus far been a major obstacle to its translation to clinical practice. To overcome these obstacles, Lis *et al*. [51] developed a technologically straightforward approach, called multi-phase 4D beam delivery (MP4D), which provides comparable dosimetric quality to that of beam tracking without the associated complications. It takes anatomical and tumor motion into account during treatment planning and subsequently synchronizes the beam delivery in real-time so that it follows the moving tumor. The MP4D approach was previously characterized for moving targets with promising preliminary results, but the tests did not attempt to compensate for range changes that occur in a heterogeneous phantom. To our knowledge, no system with such capabilities has yet been validated or clinically commissioned.

The objective of this study was to validate, by measurement and calculation, the performance of a recently created motion-synchronized dose delivery system (M-DDS) [51], used to deliver MP4D treatments. In particular, we validated, for the first time, the ability of the M-DDS to compensate for tumor motion in the presence of anatomical, motion-induced range changes. Libraries of 4D-optimized carbon-ion treatment plans were delivered to phantoms and absorbed dose distributions were measured. The dosimetric quality was assessed by examination of the dose coverage, conformity, overdose and uniformity. These quantities were compared for deliveries with a variety of test cases, including those with stationary and moving tumors, with and without the application of motion synchronization.

5.2. Materials and Methods

We validated a prototype system to treat moving targets with scanned ion beams. The overall approach was to synchronize the delivery of the beam to the periodic motion of the target, to allow for almost continuous delivery of the beam to the moving target. This capability included compensating for motion in heterogenous anatomy, which would otherwise cause range over- and under-shoots due to the anatomical, motion-induced range changes. For the convenience of the reader, we briefly review here the previously reported methods for motion mitigation with MP4D deliveries [29, 51], the treatment planning system [145], and the experimental apparatus [51]. We then describe the analysis methods for assessing the impact of managing organ motion.

5.2.1 Treatment Planning System and Treatment Delivery System

Treatment plans were created with the research treatment planning system developed at GSI Helmholtzzentrum für Schwerionenforschung GmbH (GSI), called TRiP4D [26]. This is an extension of TRiP98 [76, 77], which takes into account changes in patient anatomy caused by respiratory motion. Several previously established planning strategies were used,

including conventional- and robust 4D optimization and conventional- and robust 3D optimization (these are each explained below). To create a 4D treatment plan, a 3D sub-plan is created on each of the respiratory motion phases found in a 4DCT image set. The library of sub-plans is utilized together as a complete, or composite, treatment plan. In this study, we used two simple phantoms to represent the human thorax and a moving tumor. We purposefully selected simple phantoms to facilitate direct comparisons of calculated and measured dose distributions. These comparisons were essential for validating the dosimetric performance in test scenarios where the target depth or range varied in time. More specifically, two types of variations were considered, including constant range variations (created with a stationary, homogenous wedge), and discrete range variations (created by a stationary slab containing heterogeneities).

4D treatment plans were created for each phantom. First, 4DCT image sets were created by shifting a $4/3\pi$ $3 \times 3 \times 2$ cm^3 ellipsoid target or a $6 \times 6 \times 4$ cm^3 cuboid target contour within a simulated water box phantom. The targets followed a Lujan2-type motion trajectory [122] that was lateral to the beam axis. To explore the impact of the number of motion phases on delivery quality, we created 4D plans containing 3, 6 and 10 motion phases. Sub-plans were optimized to cover the clinical target volume (CTV) in each motion phase with a fraction of the prescription dose, such that the sum of the sub-plan doses results in the target receiving the prescription dose. The preceding planning method will be referred to as 4D optimization for brevity. For 3D optimization, 3DCT image sets of the ellipsoid and cuboid targets were created and used during treatment planning.

Both conventional and robust optimization planning techniques were used. For conventional optimization, treatment plans were created for CTVs which had 3 mm isotropic margins, while for robust optimization, margins were calculated from nine uncertainty scenarios, including range uncertainties and target position shifts, to minimize their

dosimetric impact. Robust optimization was described by Wolf *et al.* [146]. Plan libraries were created for ellipsoid and cuboid target volumes, on 3, 6 and 10 amplitude-based motion phase 4DCT images and optimized to a homogenous absorbed dose of 3 Gy.

The plan libraries were delivered with the motion-synchronized dose delivery system (M-DDS) [51], which was created to accelerate research and translation of motion mitigation strategies in ion therapy. This system was implemented in a research version of the dose delivery system (DDS) that is used clinically at the National Center for Oncological Hadrontherapy (CNAO) [25]. It was similarly implemented in the radiotherapy research facility (Cave M) at GSI [147].

The general approach considers motion of the entire anatomy during treatment planning. This allows for compensating for the motion of heterogeneous tissue and variable target depths without the need for real-time modifications to the beam spot delivery positions during delivery. Instead, the real-time target position is monitored to redirect delivery from sub-plan to sub-plan, as the target moves to another motion phase. As such, the sub-plans are delivered as a series of discrete stationary plans. This continues until the entire prescription dose is delivered. For this study, up to 10 motion phases were considered, corresponding to the number of phases typically found in a 4DCT for lung cancer patients; however, additional motion phases can be trivially added if needed. Though the number of motion phases is discrete, the tumor motion is continuously monitored, and a variety of motion monitoring devices can be selected.

In this study, we used continuous monitoring of target motion to adapt the delivery sequence of sub-plans. The 1D target motion was monitored with an optical distance sensor (OD100—35P840, SICK, Waldkirch, Germany). The signal amplitude was digitized and analyzed to yield a discrete motion phase. The sub-plan found in the plan library, corresponding to the detected phase, was then accessed. During beam delivery, the beam

spots in the sub-plan that corresponded to the detected motion phase were delivered in sequence until complete, or until another motion phase was detected. When another phase was detected, the delivery was then redirected to the nearest beam spot within the corresponding sub-plan and delivery continued as before. Once all of the spots in an iso-energy slice (IES) were delivered for the given sub-plan, the beam was suspended until delivery was directed to a sub-plan containing yet undelivered spots of the same energy. This process continued until all beam spots for that IES were delivered, then delivery progressed to the next IES. For deliveries to static targets (plan libraries with one motion phase), all the beam spots are delivered in sequence for each IES until all beam spots were delivered.

At the time of this study, the refurbished accelerator system at GSI was only capable of single-energy deliveries; subsequent work will implement fast and automated switching between accelerated beam energies to efficiently deliver multiple beam energies. Therefore, all plans were delivered with 280 MeV/u carbon ion beams. As a provisional means to produce multiple beam energies and ranges within a single delivery, we used a binary range shifter comprised polyethylene (PE) plastic slabs [73]. The beam energies, as specified in treatment plans, were converted to binary codes that correspond to range shifter settings. The range shifter settings specify the insertion of a combination of range shifting absorber slabs to modulate the beam range. Each of the selected binary codes corresponds to a combination of plastic slabs that allowed for shifting the beam spots longitudinally by as little as 0.1 mm increments. The range shifter was further described elsewhere [73].

This motion-synchronized dose delivery system was previously implemented into the M-DDS and preliminary tests were reported [51].

5.2.2 Experimental Setup

Plan libraries were delivered to two setups, containing a heterogenous phantom, and moving slabs and dosimeters (Figure 5.1). Treatment deliveries were repeated twice for each setup: once to irradiate a 2D ionization chamber (IC) array detector (Octavius 1500XDR; PTW, Freiburg, Germany) and again to a stack of six radiochromic films (EBT3 Gafchromic; International Specialty Products, Wayne, NJ). The 2D IC array detector was placed within a 5 mm thick PMMA holder, and the film stack comprised 6 films was placed between 10 mm slabs of PMMA [148]. The 2D IC array detector, containing ICs filled with air at ambient pressure, was set to integral mode to measure total delivered dose. Both holders were mounted on top of a motorized linear stage (M-414.2PD; Physik Instrumente (PI) GmbH, Karlsruhe, Germany), aligned perpendicularly to the beamline. Slabs of water equivalent plastic, corresponding to 56.7 mm water-equivalent thickness (WET) were placed in front of these holders, on the linear stage. The linear stage was programmed to move with a 20 mm, uni-axial Lujan2-type respiratory motion-like pattern [122], and the motion was monitored in real time with an optical distance laser sensor [51, 149].

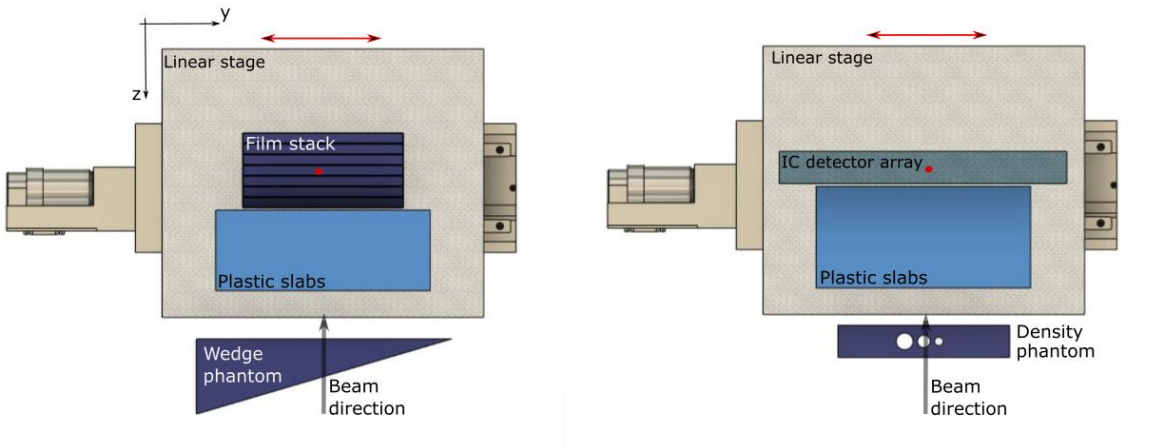

Figure 5.1. Setups for testing motion compensation through heterogenous targets. A combination of four setups were used with either the wedge or density phantom and where measurements were made with either an IC array detector or film stack. A top view of the wedge-shaped phantom (left) and slab phantom with density heterogeneities (right) are shown, placed in front of a periodically moving linear stage. For all setups, the dosimeter was placed behind a set of plastic slabs. Isocenter is marked with a red circle and the linear stage movement is indicated with a red arrow.

Both setups contained a range modifying phantom. These included a wedge-shaped piece of PMMA ('wedge phantom') and a rectangular shaped piece of PMMA ('density phantom') with three air cavities (Figure 5.1). These were used to test uniform, gradual changes to the thickness proximal to the target, and discrete gradients from air gaps respectively. The wedge phantom was 100 × 70 × 128 mm^3, with a lateral slope of 0.3 mm/mm. The density phantom was a 160 × 109.9 × 30 mm^3 block of PMMA with 15.8, 12.0, and 8.1 mm diameter cylindrical air gaps. In both cases, the wedge and density phantoms remained stationary and were placed in front of the detector and water-equivalent plastic slabs, which were placed on top of the moving linear stage. The density phantom induced range changes of 5.5 to 18.4 mm and the wedge phantom induced a maximum range gradient of 8.8 mm/mm. In addition to the MP4D deliveries, 3D optimized plans were delivered to moving targets, without motion mitigation, to assess the dosimetric impact of motion interplay effects. Similarly, 3D-optimized plans were delivered to static targets to determine the reference dosimetric performance of the treatment delivery system.

5.2.3 Data Analysis

The dosimetric quality of deliveries through the multiple range phantoms was analyzed by reconstructing beam monitoring data from treatment delivery log files of the M-DDS. The dose delivery data log files were reconstructed on the 4DCT images containing a simulated water-box phantom. The dose delivery data log files and motion monitoring data log files, from the motion monitoring system [51], were parsed and reformatted into the TRiP4D treatment plan format. TRiP4D was then used to calculate (reconstruct) the delivered dose distributions from the reformatted files. Virtual target volumes were created within each water-box phantom to calculate the dose distributions on. We then compared the reconstructed, planned and measured dose distributions. The dosimetric quality metrics we selected to assess motion management included uniformity, conformity, dose coverage and

overdose. Each of these metrics were calculated from dose volume histogram (DVH) data from planned and delivered dose reconstructions. Conformity number is

$$CN = \frac{V_{T,p}}{V_T} \times \frac{V_{T,p}}{V_p} \quad (1)$$

where $V_{T,p}$ is the portion of the planning target volume (PTV) that receives a dose that is greater than or equal to the prescribed dose, D_p, V_T is the PTV, and V_p is the volume that receives a dose that is greater than or equal to D_p [36]. A CN value of 100 % is ideal and, while there is no threshold for an acceptable CN, we considered > 60 % to be acceptable. Homogeneity (HI), which is a measure of delivery uniformity, is

$$HI = D_5 - D_{95} \quad (2)$$

where D_5 and D_{95} are the percentages of the prescription dose, D_p = 3 Gy, which are delivered to 5 % and 95 % of the tumor volume, respectively [150]. An HI of 0 % is ideal and < 5 % is considered acceptable [35]. Tumor dose coverage, which is the percentage volume of the PTV that received at least 95 % of the D_p, is represented by V_{95}. A V_{95} of 95 % is considered clinically acceptable. Overdose, denoted by V_{107}, is the percentage of the PTV that receives over 107 % of the prescription dose. Zero overdose is ideal. The acceptable ranges for these metrics were selected for the purposes of this study.

Each measured dose distribution was compared to the corresponding planned dose distribution and reconstructed dose distribution. The 3D generalized gamma index analysis [151], was used to compare the distributions, including, to quantify the degree of agreement between each pair of dose distributions. Pass criteria of 3 % dose difference and 3 mm distance to agreement were applied in all cases. Pass rates of > 90 % were considered acceptable. The purpose of comparing measured and reconstructed dose distributions was to validate the accuracy of the dose reconstruction method. The purpose of comparing measured and planned dose distributions was to determine the amount of unintended delivered dose during beam gating and spill pauses.

We performed limited quality assurance (QA) on the beam output prior to dosimetry measurements. The QA comprised relative dosimetry, using the methods described by Luoni *et al.* [152]. Specifically, the constancy of the beam output (relative absorbed dose) was measured with a farmer-type ionization chamber (PTW 30010 Farmer Chamber; PTW, Freiburg, Germany), placed at isocenter. The farmer chamber was inserted into a 30 × 30 × 1 cm^3 water-equivalent plastic holder slab, with a water-equivalent point of measurement at 5 mm depth. A 5 × 5 cm^2 square field of 2 Gy absorbed dose was delivered with 280 MeV/u carbon ion beams without range modulation. Each measurement was repeated three times. The same field was delivered to a film at 5 mm depth to measure field homogeneity. This QA approach was selected because it is well established, fast and because beamtime for QA procedures was severely limited at the time of this study.

We defined reference conditions to facilitate calibrations of two dosimeters (a 2D IC array detector and radiochromic films). The reference conditions comprise three major elements, namely, a reference radiation field, a reference phantom, and a reference measurement location. The reference radiation field comprised a 280 MeV/u carbon ion beam without range modulation and with an incident beam spot size of 6.7 mm full-width half maximum, delivered to a measurement depth of 5 mm, at isocenter.

We calibrated the 2D IC array detector and film to absorbed dose under reference conditions. The calibrations of these dosimeters were based on measurements of their responses to irradiations of known absorbed dose. The known absorbed dose was determined from dose reconstructions, which were previously calibrated and are described elsewhere [145]. We simultaneously calibrated the IC array detector and films. The detector was positioned at isocenter, inside of a 31 × 40 × 4 cm^3 box-like holder with 5 mm water-equivalent thick walls. A film was taped directly in front of the 2D IC array detector, inside the holder. A calibration plan was delivered that comprised eight 30 × 30 mm^2 square fields,

ranging in fluences from 5×10^4 to 1×10^7 particles/ mm^2, corresponding to absorbed doses of 0.1 to 9.9 Gy at 1 cm depth, in the plateau region. The initial beam energy was 280 MeV/u, and no additional range modulation was introduced. This interval of absorbed dose values was selected to encompass the dynamic range anticipated for the clinical deliveries and to remain within the dynamic range of optical densities for radiochromic films.

We used an established formalism to calibrate the IC array detector [51, 148, 153]. These are briefly reviewed here for the convenience of the reader. The IC array detector was calibrated to absorbed dose to water under reference conditions. Measured absorbed dose is given by

$$D_{IC} = M \times C \times k_Q \tag{3}$$

where M is the measured response (corrected for leakage, temperature, and pressure) and C is the calibration coefficient under reference conditions, k_Q corrects for the effects of the difference between the reference conditions and the non-reference conditions. We confirmed the stability of the previously determined value of C = 1.2 Gy per unit of measured response, following methods similar to those described by Stelljes *et al.* [154]. The effects of non-reference conditions were negligible and k_Q was approximated as unit value. The absolute absorbed dose values, at the same locations as the ICs and under reference conditions, were also reconstructed from delivery log files, which allowed us to calculate dosimetric outcomes from the reconstructions.

We used radiochromic films to simultaneously measure relative 2D absorbed dose distributions under reference and non-reference conditions. Films allowed for faster data acquisition at multiple depths during the limited beamtime available. They also provided the high spatial resolution needed to measure dose distributions distal to the wedge and density phantoms. We used methods similar to those of Yonai *et al.* [155] for calibrating the film response to relative absorbed dose, which is briefly reviewed here for the convenience of the

reader. First, the treatment planning system was used to create a calibration plan under reference conditions, described above. The calibration plan was delivered to the radiochromic film, in the geometry described above. The exposed films aged for one day, then were digitized (DosimetryPro Advantage Red; VIDAR Systems Corporation, Herndon, VA, USA) using a 16-bit sampling and 300 dots per inch resolution. The net optical density of the scanned film was determined by

$$OD_{net} = OD_m - OD_{bkg} \tag{4}$$

where OD_m is the measured (scanned) optical density, and OD_{bkg} is the background optical density scanned in an unirradiated area on each film. The OD_{net} was determined in the central region of each square field in the calibration film. The known absorbed dose values at the center of each square field, D_{film}, were fit to eight measured OD_{net} values according to

$$D_{film} = D_{film,uncorr} \times k_{Q,film} \tag{5}$$

where $D_{film,uncorr}$ is the uncorrected, measured absorbed dose from films, and $k_{Q,\,film}$ is a correction factor for changes in the film response due to changes in beam quality at non-reference conditions. The uncorrected absorbed dose from the film under reference or non-reference conditions is given by

$$D_{film,uncorr} = (a \times OD_{net} + b \times {OD_{net}}^{c}) \tag{6}$$

where a, b, and c are empirical calibration fit parameters. A second order polynomial was selected to take non-linearities in film response due to saturation and non-linearities of the film scanner into account. By definition, $k_{Q,film}$ took a value of 1 at the reference condition used for the calibration. The calibration procedure above was performed separately for each batch of film used. Conceptually, Equation 6 is a generalized form of the product of $M \times C$ given in Equation 3 for ionization chamber dosimetry. The generalized form is necessary because the film's response exhibits a nonlinear dependence on OD_{net} (*i.e.*, $b \times {OD_{net}}^{c}$) in addition to a linear dependence (*i.e.*, $a \times OD_{net}$).

In addition to calibrating the film to respond linearly with absorbed dose under reference conditions, it was also necessary to correct the film's absorbed dose response to be independent of beam quality at depths of measurement other than at the reference depth, d_o. Under non-reference conditions, the value of the correction factor $k_{Q,film}$ corrected for changes in the film response due to quenching, which depends on beam quality, as specified by the beam's linear energy transfer. We determined $k_{Q,film}$ values as a function of average linear energy transfer ($\overline{LET}$) using methods modified from Yonai *et al.* [155], given as

$$k_{Q,film}(\overline{LET}) = \frac{D(\overline{LET})}{D_{film,n}(\overline{LET})} \tag{7}$$

where $D_{fim,n}(\overline{LET})$ is the absorbed dose that must be delivered ($\overline{LET}$) to obtain the same value of OD_{net} measured at reference conditions. ($\overline{LET}$) and the known value of $D(\overline{LET})$ were calculated by the TPS using dose reconstructions. The quantity ($\overline{LET}$) is the absorbed-dose-weighted average of the LET of all charged particles present at a position (x, y) in film *n*. The function $k_{Q,film}(\overline{LET})$corresponds to a factor that is called relative efficiency elsewhere [155, 156]. The values of $k_{q,film}$ were determined from one delivery of the calibration plan in which the entire phantom assembly was stationary.

The calibration and corrections embodied in Eqs. 4-6 were applied to all film measurements of absorbed dose from other beam deliveries, *e.g.*, those to confirm the accuracy of the dose reconstruction method (Section 5.2.1). For all deliveries, ($\overline{LET}$) values were obtained from the TPS at locations in the phantom corresponding to the measurement point of interest in the film.

5.3. Results

Figure 5.2 reveals that the reconstructed dose distributions agree well with the corresponding dose distributions obtained from measurements with film. This result confirms the suitability of the method for reconstructing dose distribution for the main

purpose of this study, which is to assess the quality of dose distributions delivered by various techniques. We defer discussion of the results on confirming of the reconstruction methods until later in this section.

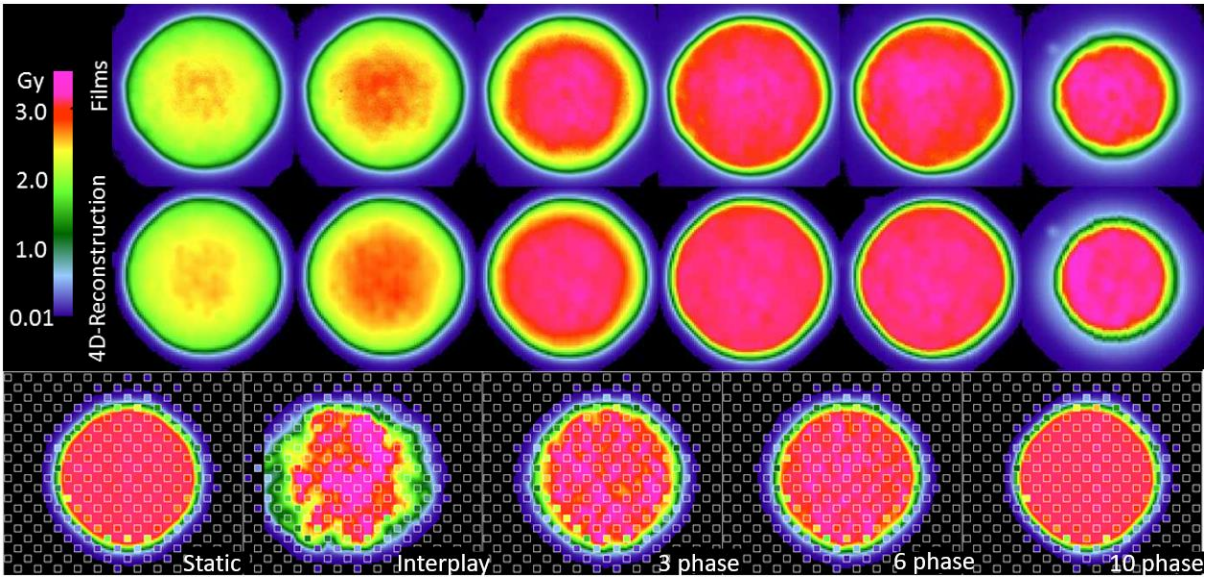

Figure 5.2. Comparison of film measurements (top row) to dose reconstructions (middle row) and 2D ionization chamber array detector measurements to dose reconstructions (bottom row). The top row shows the films from a film stack for a multi-phase 4D irradiation using 10 motion phases to the wedge phantom with 20 mm uniaxial motion. Films are ordered left to right with increasing depth in the density phantom. The depth increment between films is approximately 11 mm water-equivalent thickness. The corresponding dose reconstructions for the same delivery are shown in the middle row. The bottom row shows measured absorbed dose values (values inside of small white squares) overlaid on reconstructed absorbed dose distributions (values outside of the small white squares). The dose distributions are distal to the density phantom (see Figure 1). Distributions are from four delivery techniques: static target, moving target without motion compensation (interplay), and moving target with multi-phase 4D motion compensation. Multi-phase 4D deliveries are shown using 3, 6, and 10 motion phases in the treatment plan libraries.

We assessed the dosimetric quality of deliveries through the wedge and the density phantoms. Measured absorbed dose distributions were compared to the corresponding dose distributions from reconstructions and treatment plans. Figure 5.2 plots the absorbed dose distributions for these deliveries, including those with a static target, moving target without motion compensation (revealing the extent of interplay), and moving target with the multi-phase 4D approach (revealing the effectiveness of motion mitigation).

Specifically, dosimetric quality was assessed with four metrics: conformity, homogeneity, coverage, and overdose (Figure 5.3). The major qualitative finding from these results is that 10-phase MP4D deliveries provided the best overall dosimetric quality. The major qualitative finding is that 10-phase and 6-phase MP4D deliveries had acceptable dosimetric quality, while quality metrics for 3-phase MP4D were mixed. Figure 5.2 reveals that the reconstructed dose distributions agree well with measurements. Acceptable conformity (*CN* > 60 %) was obtained in all multi-phase 4D deliveries with 6 and 10 phases. However, at least 10 motion phases were required to achieve acceptable homogeneity (*HI* < 5 %) of the absorbed dose in the PTV. Fewer motion phases produced unacceptably large heterogeneities, due to interplay effects within each motion phase (so-called "residual motion"). The average *HI* value for all of the 10-phase MP4D deliveries (both phantom types and PTV shapes) was 8 %, approaching the criteria of < 5 %, which was achieved for static deliveries and is considered acceptable for other deliveries. Target coverage was 100 % for 10-phase MP4D deliveries and was > 98 % for 6-phase MP4D deliveries, also approaching the ideal results of 100 %, which were obtained from deliveries to a static target. These findings on coverage and heterogeneity are qualitatively supported by dose distributions plotted in Figure 5.2, which shows that the MP4D approach produces similar results for the static and 10-phase MP4D deliveries. It was expected that the deliveries using 10 motion phases would have superior results, since the residual motion was less than that with 6 or 3 motion phases. The increasing homogeneity is also seen in Figure 5.4A, where the range of average measured absorbed dose values narrow with increasing number of motion phases. Here, the average absorbed dose was within ± 1.5 % of the prescription dose for MP4D deliveries. Finally, the 10-phase MP4D approach produced hotspots in the PTV that were < 103 % of the prescribed absorbed dose. Together, these findings suggest that the 10-phase

MP4D approach provides good dosimetric quality that closely approaches the quality that was achieved for static-target deliveries.

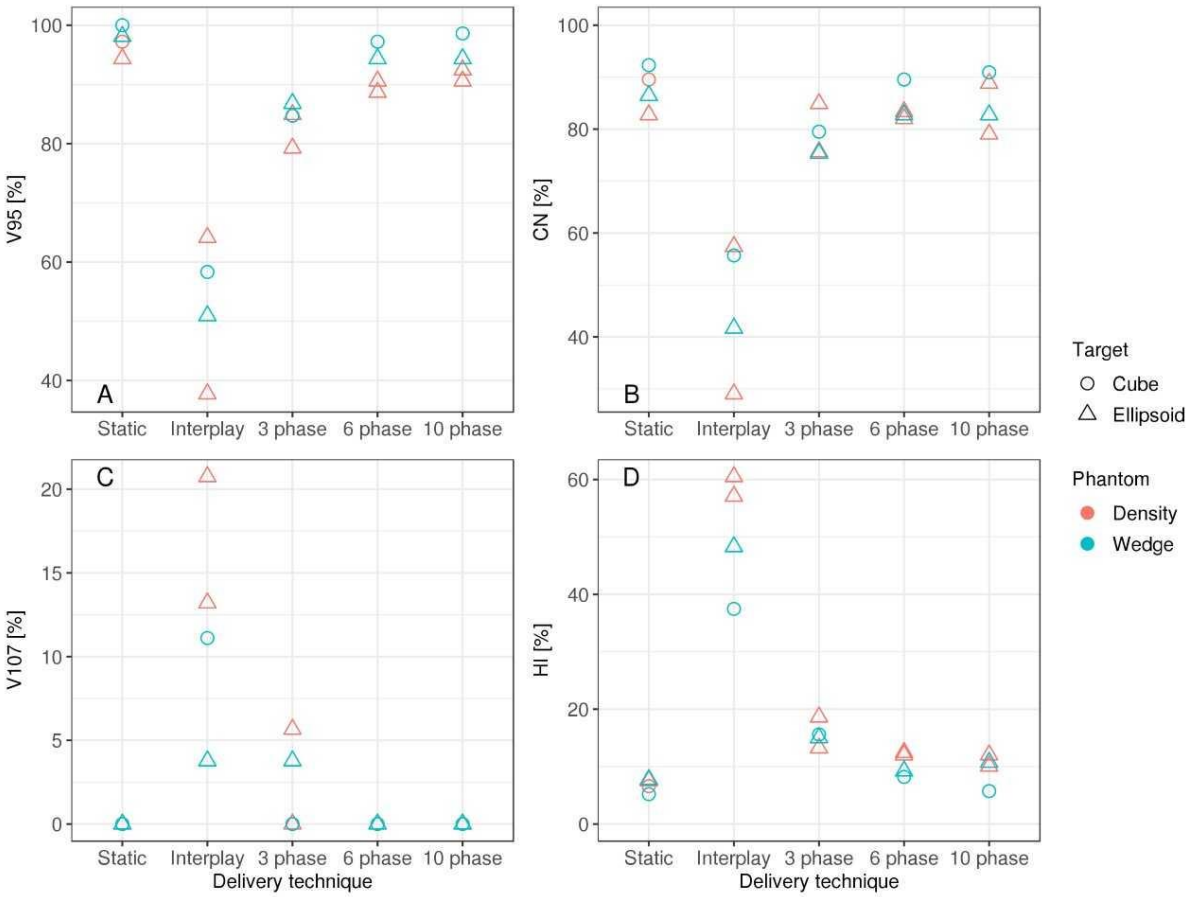

Figure 5.3. A) Dose coverage (V_{95}), B) conformity (CN), C) overdose (V_{107}), and D) homogeneity (HI) for static deliveries to stationary targets (static), static deliveries to moving targets (interplay), and 3-phase, 6-phase and 10-phase multi-phase 4D deliveries to cube and ellipsoid target volumes, through the wedge and density phantom.

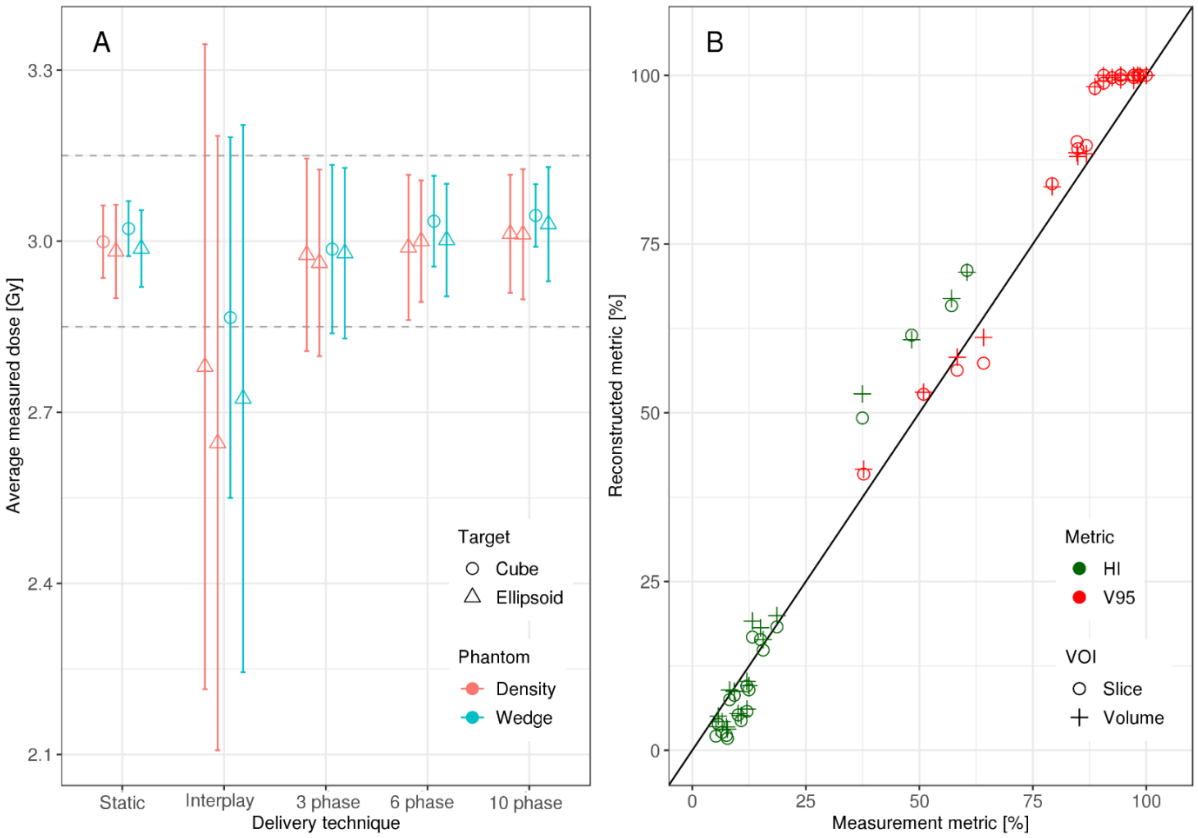

Figure 5.4. A) Average measured absorbed dose versus delivery technique evaluated using the density and wedge phantoms. The dashed grey lines delineate the ± 5 % tolerance interval centered about the prescription absorbed dose of 3 Gy and the bars indicate the spread measured dose values from each ionization chamber (IC) of the 2D IC array detector in the planning target volume (PTV) B) Homogeneity (HI) and coverage (V_{95}) for measured versus reconstructed absorbed dose distributions in the target volume. Dosimetric quality was calculated in a single iso-energy slice within the PTV and in the entire PTV for each delivery. All delivery techniques for both phantom types and for both VOIs are plotted. Data points that fall on the line indicate full agreement of measured and reconstructed HI and V_{95} values.

The results of MP4D deliveries also yielded important findings regarding over- and undershoot of the beam range and regarding the inverse interplay effect. Regarding range effects, absorbed dose distributions from treatment plans and dose reconstructions are shown in Figure 5.5, which illustrates that static robust optimization created dose distributions with range over- and undershoots. These are a consequence of taking the large range uncertainties in low density material of the phantom into account. These range effects manifest distal to the cavities of the density phantom, near the end of range. The MP4D approach reduced these range defects as, the dose delivered to these regions were “blurred out” by delivering multiple

subplans to the target volumes. Regarding the inverse interplay effect, the MP4D approach exhibited no dose defects from this (Figure 5.5B and 5.5D). The inverse interplay effect is a serious concern that is associated with the beam tracking delivery approach [26], which can deliver uniform doses to the target but increases hotspots proximal to the target in healthy tissue. With the MP4D approach, there were no hotspots in the proximal healthy tissue. Instead, the lateral extent of the irradiated healthy tissue was broadened by the amplitude of the target motion. These findings on range defects and inverse interplay further suggest that MP4D approach can provide high quality deliveries.

Figure 5.2 reveals that the dose reconstruction methods were confirmed by measurements. In particular, high gamma-index pass rates confirmed the accuracy of the treatment planning and dose reconstructions in this study. Specifically, we compared dose distributions from measurements with the IC detector array to those from the corresponding log file reconstructions (Figure 5.6C) and planned dose distributions (Figure 5.6B) obtained with moving targets. Average pass rates increased with the number of motion phases, due to the decreasing residual motion within each motion phase. In all cases, reconstructed dose distributions agreed well with measured dose distributions (Figure 5.6C), with pass rates > 90 %, confirming the validity of the dose reconstruction strategy. Gamma index analysis pass rates were lower for comparisons between planned and measured dose distributions and only static deliveries and 10-phase MP4D deliveries had pass rates > 90 %.

Similarly, we compared all dose distributions from measurements to reconstructions of static deliveries (Figure 5.6A). This comparison provided important contextual information on the magnitude of dose degradations that were caused by target motion occurring within a motion phase and without motion compensation. Pass rates were < 90 % for comparisons between static reconstructions and 3 phase MP4D measurements and were < 60 % for

comparisons between static reconstructions and interplay deliveries. For planning studies, 10 or more motion phases should be selected.

The total delivery time was calculated from treatment log files. Average total delivery time for static ellipsoid deliveries was 7.4 min. The relative increase in delivery time for 3-phase, 6-phase and 10-phase MP4D deliveries, compared to static deliveries, was 7 %, 17 %, and 21 %, respectively. This suggests that the MP4D method provides motion-mitigated deliveries with increases to delivery time that would be well-tolerated by most radiotherapy patients and compatible to existing patient caseloads.

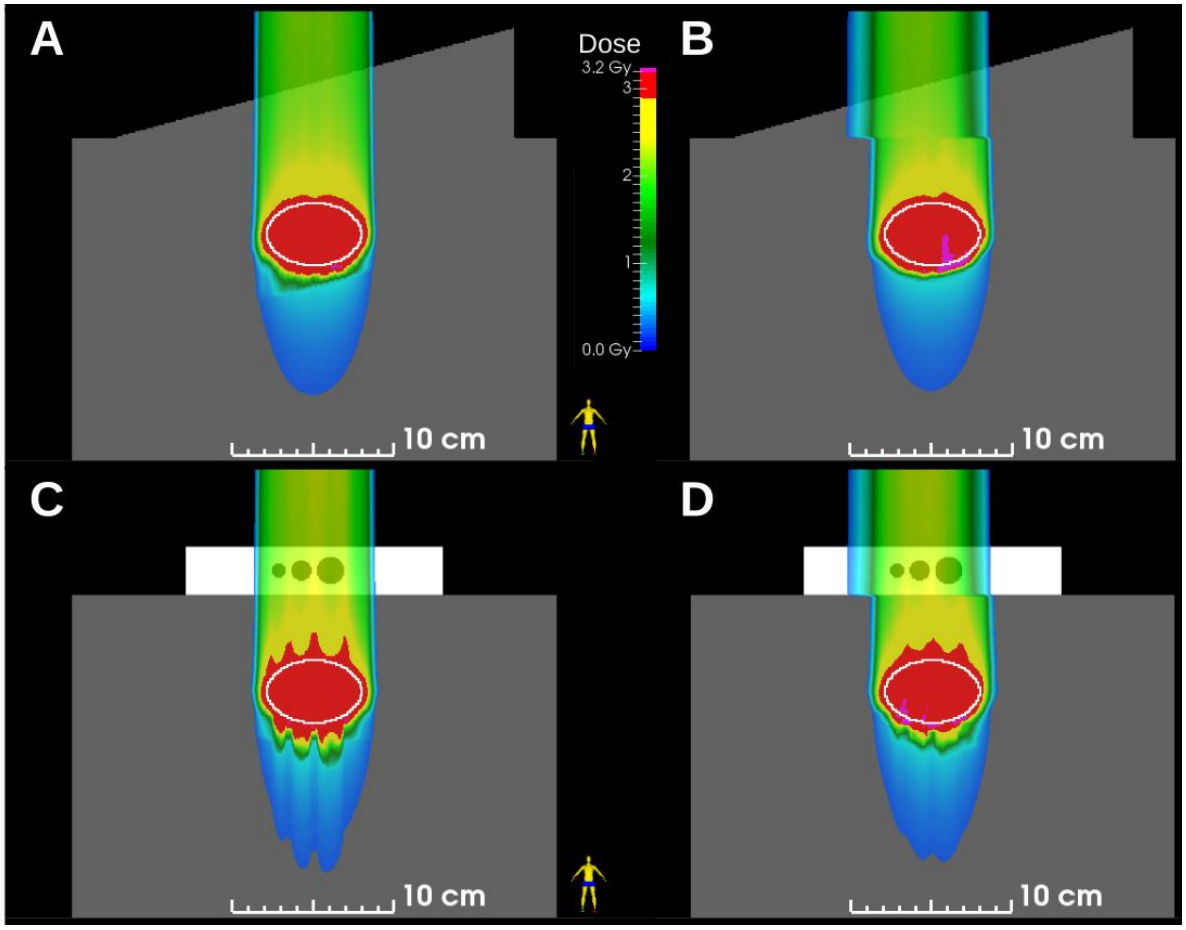

Figure 5.5. Dose distributions in ellipsoid targets (white ovals) for A) static and B) 10-phase multi-phase dose deliveries through the wedge phantom and for C) static and D) 10-phase multi-phase 4D deliveries through the density phantom. Deliveries were reconstructed from beam delivery log files and motion monitoring log files.

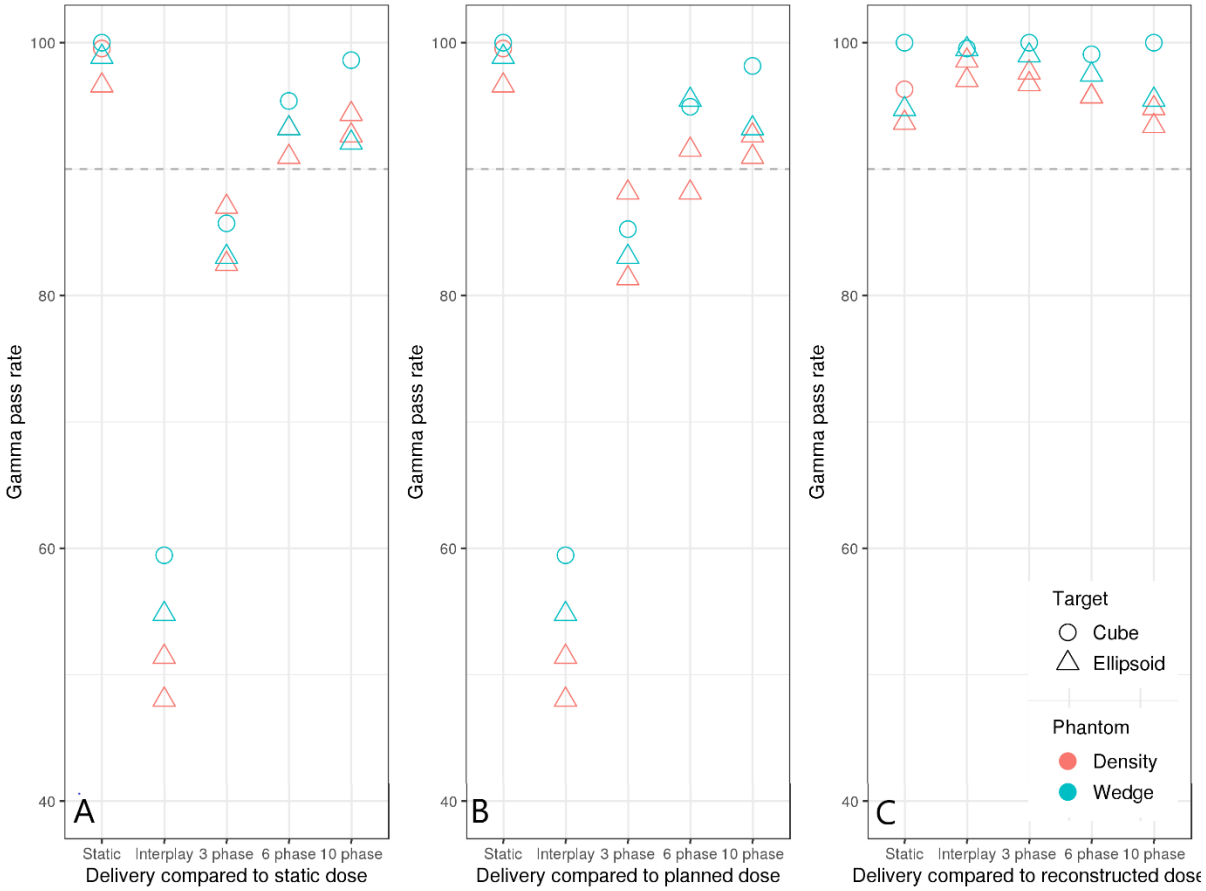

Figure 5.6. Gamma index analysis pass rates versus beam delivery technique. The pass rates indicate good agreement between measured absorbed dose distributions and A) reconstructed absorbed dose distributions for the static delivery, B) planned absorbed dose distributions and C) reconstructed absorbed dose distributions. Comparisons were made for static deliveries to stationary targets (static), static deliveries to moving targets (interplay), and multi-phase deliveries to moving targets with 3 phases, 6 phases, and 10 phases of motion compensation. Pass rates showed only a weak dependence on phantom type (wedge or density types) and target shape (cube or ellipsoid types).

5.4. Discussion

In this study, we validated the dosimetric performance of a novel multi-phase 4D treatment approach with deliveries to heterogenous phantoms. Specifically, we measured dosimetric quality of absorbed dose distributions from plan libraries delivered through two phantoms. The major findings of this study are that the multi-phase 4D (MP4D) dose delivery approach has acceptable dosimetric quality without introducing inverse interplay effects.

The implication of this study is that MP4D delivery offers a promising new alternative approach to motion mitigation that provides good dosimetric quality with

moderate technical complexity. The magnitude of technical complexity is an important characteristic because it can be a barrier on the path of translation of new technologies to clinical practice. One such technology, ion beam tracking, entails rapidly modifying planned beam spot positions to the real-time detected target motion [14, 157]. Consequently, the dose distributions delivered to a patient cannot be fully confirmed by pre-treatment quality assurance testing. One type of beam tracking, called 4D-optimized tracking, that pre-computes tracking vectors to take anatomical motion from 4DCTs into account during planning, still exhibited inverse interplay effects and other dose degradations [144]. Our results suggest that, in the absence of respiratory-motion-related uncertainties (baseline drifts and changes to the tumor trajectory), clinically acceptable projected therapeutic outcomes could be achieved without inducing significant hotspots in normal tissues (due to inverse interplay effects) and the target volume (due to interplay effects). This study provides new evidence that, when considered with other recent studies [51, 153], suggest it may be feasible to translate the MP4D approach to clinical practice for both carbon ion and proton beam treatments. It must be emphasized that the MP4D approach is still in the early stages of preclinical development and testing; further work is needed to understand how dosimetric quality is impacted by irregular motion (*e.g.*, baseline drifts and changes to target trajectories caused by coughs and sneezes). Furthermore, additional research is needed to implement and evaluate MP4D deliveries with real-time corrective tracking and to compare the MP4D approach to the 4D-optimized tracking approach.

This work is broadly coherent with previous literature on motion mitigation approaches for proton and ion therapies. Our findings extend previous preliminary studies that suggested feasibility of a novel dose delivery system (M-DDS) with integrated motion-synchronization strategies [51, 153, 158]. The MP4D delivery approach poses a straightforward solution to solve the limitations of 3D tracking and 4D-optimized tracking.

Previous research at GSI focused on 3D tracking, which required utilizing a fast wedge system to compensate for motion-induced range changes in real-time, during dose delivery [157]. Experiments confirmed the range compensation capabilities of this system. The 3D tracking method, reported by Saito *et al.* [157], compensated for translational target motion (only), but beam spot delivery accuracy was still within 5 mm in the lateral and longitudinal directions. Importantly, this work revealed several complications with potentially important clinical implications for certain situations. First, the so-called "inverse interplay" effect was observed, due to differences in motions of the target and the tissue of the entrance channel [159]. Second, complex motion, such as tumor rotations or deformations could not be fully compensated for [24]. Finally, for tissues with large heterogeneities, no solution was found to compensate for motion-induced range changes. 4D-optimized tracking [14], or online adaptive tracking [160] partially solved the latter problem. However, that 4D tracking implementation encountered several obstacles, including limitations on the available hardware speed and memory, and difficulties with synchronizing the system timing. These issues rendered the system obsolete; it was dismantled and replaced with the motion-synchronized dose delivery system described here and elsewhere [51].

In consideration of the above, the MP4D delivery strategy is generally less complex, and allows for integrating a variety of treatment planning strategies, such as 4D optimization [78]. It also accommodates the pre-treatment quality assurance methods similar to those currently used clinically [161]. Our findings on dosimetric quality are comparable to those of the system at NIRS. At NIRS, phase-controlled rescanning is used to deliver a full set of rescans during each gating window [38]. X-ray fluoroscopy detects when the tumor is within a pre-defined gating window, resulting in accurate treatment to the tumor volume. Typical results for phase-controlled rescanning were a D_{95} of over 95 %. Further, clinical outcome data revealed 2-year survival rates were as high as 82 % for stage 3 lung cancers treated with

passive ion beams [162]. This method relies on the fast-scanning magnets of the HIMAC accelerator at NIRS, and slower beam deliveries may not be able to achieve the same results. In contrast, our approach allows for continuously adapting the delivery sequence to detected motion, with minimal delivery pauses (a maximum 21 % observed increase to total delivery time with regular motion), and with minimal residual motion during active beam delivery. For these reasons, it appears that the MP4D approach may find broader applicability than is possible with other approaches.

Our study has several strengths. First, we performed all of our measurements with a modular and portable dose delivery system [51], with integrated solutions for motion-synchronized dose delivery. This is potentially broadly applicable and the M-DDS has already been demonstrated at multiple centers, including CNAO and GSI. Additionally, as the motion mitigation portion of the M-DDS is an optional module, the M-DDS requires no modifications to run either with or without the motion mitigation module. This allows for implementing the M-DDS in a stepwise manner into existing facilities. We also selected methods for assessing dosimetric quality that are standard techniques within ion therapy centers [35, 87]. Further, the range changes were measured by delivering beams to simple phantoms rather than anthropomorphic phantoms, eliminating additional variables, such as range uncertainties associated with variations in tissue density, irregular breathing patterns, and generally more complex range changes that are found in a human anatomy.

Our study had several limitations. At the time of these experiments at GSI, our beam gating system (based on radiofrequency knockout extraction) could not yet fully gate the beam [147], and the accelerator system could not yet provide beams of multiple energies in any one delivery. We discuss both of these limitations in detail here. The inability to completely gate off the beam results in an insignificant but observable amount of undesired radiation that only slightly degraded the dose distributions. Specifically, a trend was apparent

(Figure 5.6) that, as the number of motion phases increased, the average absorbed dose in the PTV increased as well. The increase was under 0.4 % undesired, additional dose. To overcome the limitation of having only single energies available, a passive range shifter system was utilized to modulated beam energy and range. Due to the additional material and air gaps between the range shifter plates, the beam spot size was strongly dependent on the amount of range shifter material [161]. This was not a serious limitation, as the range compensation capabilities could still be demonstrated, and the TRiP4D treatment planning system was updated to take the correct spot sizes into account in the dose calculation algorithm. In the next stage, the experiments reported here will be reproduced at CNAO, where the gating system is tuned for therapy and beam energies of 120 – 400 MeV/u are available for carbon ions [25]. Another limitation of our study is that we have not tested the MP4D delivery strategy under more complex respiratory scenarios, including baseline drifts, changes to breathing amplitude and changes to breathing speed, as well as more extreme respiratory irregularities, including coughing. These capabilities will be implemented in later stages, along with improved beam gating, which will be used for handling unforeseen motion, including coughing. Additionally, we did not use anthropomorphic phantoms for testing [163]. Geometries that are more complex could further confirm that our motion-synchronized dose delivery strategy can compensate for range changes and represent scenarios that are closer to clinical conditions. However, this is not a major limitation, as the performance results presented in this work provide a more representative example of the extent to which this delivery strategy can handle two individual range change scenarios. Other studies have investigated the impact of tumor motion with scanned ion beams using anthropomorphic phantoms [164]. Further, in later stages, pre-clinical tests will be performed with anthropomorphic phantoms to characterize the full capabilities of the M-DDS. Finally, we did not compare the MP4D delivery strategy to other motion handling methods currently used in

clinics (including the gating methods, and ITV-based deliveries with rescanning [165]) or study the results of combining motion mitigation strategies. These strategies are studied in detail elsewhere [165, 166], and delivery degradations in the complete absence of motion mitigation are shown in this study.

The results presented in this work are part of an ongoing effort to develop motion-synchronized dose delivery strategies at GSI. The motion-synchronized dose delivery system was previously assessed for safety [161], and the strategy has been validated against other approaches, including ITV-based deliveries with rescanning [165]. In the future, dose degradation due to irregular motion and differences between motion during imaging and during delivery will be quantified, and corrective motion tracking will be implemented to correct for irregular target motion. The long-term goal is to translate the multi-phase 4D delivery approach and motion-synchronized dose delivery system into clinical use at CNAO.

5.5. Conclusion

We validated the dosimetric performance of multi-phase 4D treatment delivery with scanned ion beams in the presence of multiple beam ranges. The results of this work demonstrate that it is possible to deliver motion compensated dose distributions in the presence of anatomical heterogeneities. Notably, the dosimetric performance was achieved without high technological demands or specialized equipment for mitigating target motion.

Chapter 6. Treatment Quality and Projected Therapeutic Outcomes for Multi-phase 4D Dose Deliveries of Treatment Plans with Proton and Carbon Ion Beams

6.1. Introduction

Almost 290,000 people in the USA were diagnosed with lung or pancreatic cancer in 2019 [2]. Of these, over 40 % were diagnosed at late stages, and 5-year survivorship was only 15 % for late-stage lung cancer and 8 % for late-stage pancreatic cancer, respectively. Low survival rates are thought to be due, in part, to difficulty in treating these cancers [144]. Several prospective clinical trials have revealed that, for some cancers, proton and ion beam therapies reduce the risk for treatment complications compared to photon therapies [43, 167]. Carbon ion and proton therapy have been used to treat deep-seated tumors, moving tumors, and certain radioresistant tumors [168, 169]. One such radioresistant tumor, early-stage non-small cell lung cancer (NSCLC), responds well when treated with stereotactic body radiation therapy (SBRT). In contrast, late stage NSCLC treatments with photons have not demonstrated a clinical advantage with dose escalation [170, 171], and severe normal tissue complications have been seen in over 20 % of cases [172]. Proton and heavier ion beams have also proven advantageous relative to photon beams in cases where tumors are located near critical organs [173]. These ion beams have emerged as effective treatments for some thoracic tumors [174].

Considerable attention has been paid to studying the physical aspects of methods to treat moving tumors with radiation beams, particularly with photon beams [141, 175], but also with ion beams [176]. Approaches used in the clinic include immobilization (such as breath hold [177] and abdominal compression [178]), free breathing with expanded safety margins (such as the internal target volume (ITV) method [165]), and free breathing with respiratory-synchronized beam gating [166]. Several well-characterized methods exist for monitoring respiration, including chest wall motion monitoring, surgically implanted

radiopaque fiducial marker monitoring [179] and transmission photon imaging techniques (e.g., fluoroscopy). Even with these approaches, poor clinical outcomes have persisted, likely due to the dose distributions in the tumor and normal tissue being compromised by tumor movement [176]. Motion mitigation strategies have not yet fully exploited the technical aspects of ion therapy, such as sharp gradients and fast pencil beam scanning, to deliver conformal, motion mitigated beams. To overcome these limitations, two approaches have emerged: sparing surrounding healthy tissue by minimizing tumor motion during active delivery and synchronizing beam delivery to tumor motion. To date, only a few prototypes have explored the latter approach [14, 29, 31, 157]. These early studies revealed promising preclinical results, but also revealed that the treatment planning and delivery processes were generally complex, machine specific, and fraught with obstacles on the path to translate them to clinical practice. Also, knowledge of the differences in dosimetric performance of these approaches was incomplete.

Further, the literature is replete with studies that explored the superior conformity and theoretical radiobiological advantages of carbon ion therapy regarding tumor control [180-183]. It has also been suggested that conformity is even more important in treatments with dose escalation [43, 169]. Both radiobiological advantages and conformity are especially important for late-stage cancers, which are often radioresistant, such as pancreatic tumors and stage III/IV NSCLC [184]. Recent clinical outcome studies have suggested that conformal carbon ion therapy results in superior complication-free survival as compared to SBRT for stage II/III NSCLC [185] and for pancreatic cancers [186], due to the radiobiological advantages of carbon ion beams, but few clinical studies have been performed on treating late-stage lung cancers with ion therapy. A recent clinical outcome study at the National Institute of Radiological Sciences (NIRS) revealed that conformal carbon ion therapy resulted in nearly 55 % overall survival at two years [187]. These results are promising, but the

approach appears suitable only for patients with minimal changes to the respiratory motion trajectory. A recent treatment planning study by Eley *et al*. [14] revealed that the beam tracking approach achieved superior dosimetric results, but introduced a high degree of technical complexity that have hindered efforts to translate the technique to clinical practice. It was not known if the dosimetric advantages of beam tracking could be obtained with a simpler approach that is more amenable to clinical translation.

The objective of this pre-clinical study was to assess the characteristics of a motion-synchronized treatment delivery approach, called multi-phase 4D dose delivery (MP4D). Characteristics considered included dosimetric quality and projected therapeutic outcomes. For context, compared results from MP4D deliveries to those from unsynchronized approaches for treating moving tumors. We evaluated MP4D separately for proton beams and carbon ion beams using image sets from two patients who had previously received radiotherapy. Calculations were verified against measurements using two motion mitigation strategies. We assessed plan quality in terms of dose conformity, uniformity, and tumor coverage, as well as the projected therapeutic outcomes by normal tissue complication probabilities and tumor control probabilities.

6.2. Materials and Methods

In this study, we compared the dosimetric quality and projected therapeutic outcomes achieved by motion compensated approaches with proton and carbon ion beams. These approaches were ITV-based rescanning and MP4D. For the convenience of the reader, we briefly review the previously developed methods for motion mitigation [51] and treatment planning [51] that are used in this study. We also describe the experimental set-up, as well as metrics used to characterize and compare treatment plans. We compared the relative performance of these motion mitigation methods in terms of dosimetric quantities and projected patient outcomes. The results from motion mitigations approaches were compared

to static deliveries without target motion (to estimate the best achievable results) and deliveries with target motion and no motion compensation (to estimate the magnitude of dose degradation caused by anatomical motion).

6.2.1 4D Treatment Planning and Motion Mitigation

We used a research treatment planning system developed at GSI Helmholtzzentrum für Schwerionenforschung GmbH (GSI), called TRiP4D [145]. This treatment planning system extends TRiP98 [76, 188] to consider patient motion during the treatment planning process. Specifically, 4DCT images were utilized to create a conformal, 4D optimized treatment plan using each motion phase. In this study, two forms of 4D optimized treatment planning and delivery approaches were used: conformal treatment plan libraries for MP4D deliveries, and ITV-based plans for rescanned deliveries.

In order to create an MP4D plan, or a library of treatment plans, a 3D sub-plan was optimized on each of the respiratory motion phases contained in the patient 4DCT image sets. Each of these sub-plans were initially optimized separately to the entire prescription dose. Two forms of optimization were used for the MP4D plans: conventional optimization on a geometrical planning tumor volume (PTV) with 3-mm isotropic margins, or with robust optimization on a clinical tumor volume (CTV) with ± 3.5 % range margins to incorporate uncertainties in Hounsfield units in the CT images and 3 mm margins to consider tumor position uncertainties [78, 146]. 4D optimization involved using a cost function to create a uniform dose distribution on the PTV to at least 95 % of the prescription dose in the entire plan library, while minimizing the dose to surrounding organs at risk (OAR). The optimization incorporated information about temporal anatomy changes due to respiratory motion and included margins for range uncertainty in the treatment plan. After optimization, the number of particles in each beam spot was scaled by a weighting factor, such that the total absorbed dose of the plan library was equal to the prescribed dose [146]. The library of

optimized and weighted sub-plans was then utilized together as a single MP4D treatment plan.

We note that for simplicity and clarity, we simplified the treatment planning methods by assuming a generic relative biologic effectiveness (RBE) of unit value for all tissue and endpoints. The higher RBE of carbon beams was implicitly taken into account by taking into account α/β values for the tumor, heart and lung. This approximation is discussed later in the manuscript.

A similar process was utilized to create ITV-based treatment plans. 3D sub-plans were optimized simultaneously on each of the motion phases found on the patient 4DCT image sets [78]. An ITV was created which encompassed to entire tumor trajectory. Both conventionally and robustly optimized plans were created with 15 rescans to mitigate heterogeneities due to tumor motion [189]. Additionally, plans were created for deliveries to static PTVs and moving PTVs without motion compensation by optimizing the entire treatment plan on the reference motion phase of the 4DCT images. This study was designed as a proof of principle, and is not representative of actual patient treatment. Two simplifications were afforded for this study to facilitate direct comparisons of various treatment strategies. Specifically, each treatment plan contained only one beam orientation, and dose constraints were not applied to OARs during the treatment planning optimization process.

The MP4D motion mitigation delivery strategy was to synchronize the delivery of various 4D optimized treatment plans to the motion of a moving target. To accomplish this, we used a recently developed motion-synchronized dose delivery system (M-DDS), as described by Lis *et al*. [51] and reviewed here for the convenience of the reader. The M-DDS extends the dose delivery system (DDS), which was originally developed and is currently used clinically at the National Center for Oncological Hadrontherapy (CNAO, Pavia Italy), in

two major ways, namely, to provide integrated motion mitigation capabilities and to contain the necessary modularity to operate at multiple accelerator facilities. Specifically, the M-DDS is available for research studies at the radiotherapy research beamlines at CNAO and at GSI [147]. The system is embodied by a portable crate that contains eight electronics modules. Each module is a field programmable gate array (FPGA) that is dedicated to controlling one or more dose-delivery functions. These functions include transfer of beam delivery data (loading and sending of delivery information), monitoring beam intensity, monitoring beam spot position, controlling magnetic scanning of the beam, monitoring target motion and synchronizing it with beam delivery, interfacing with the accelerator timing system, initiation and termination of the irradiation, and various safety functions [161]. The motion mitigation features are implemented in two of these modules. The FPGA modules are commercial units (PCI Extensions for Instrumentation Express (PXIe); National instruments, Austin, Texas). The hardware and software interfaces to the accelerator control systems were developed in house [147].

The MP4D approach requires continuous monitoring of the tumor motion in real time. The continuous motion signal is used to select the corresponding discrete motion phase from the library of phase-specific treatment plans. The beam spots from the treatment plan corresponding to the current motion phase are delivered in their planned sequence until a change in the motion phase is detected. The corresponding treatment plan is then selected, and beam spots are delivered starting at the location where the delivery was suspended in the previous plan. This is repeated until all beam spots in the iso-energy slice (IES) are delivered. The process continues until all IES have been delivered. For deliveries to static targets and deliveries to moving targets without motion compensation, the treatment plan is delivered in sequence for all IES.

We retrospectively created robust 4D optimized and conventional 4D optimized treatment plans for two patients who had previously received radiation therapy for lung cancer. We planned and delivered them with proton beams and carbon ion beams using two motion mitigation methods and compared these deliveries to corresponding static deliveries. These motion mitigation methods included MP4D and ITV-based deliveries with rescanning. The former approach has the theoretical advantage of better dosimetric performance, and the latter has the advantage of greater conceptual and technical simplicity.

The MP4D approach, which has not yet been used clinically, is described above and elsewhere [29, 51]. The approach to ITV-based rescanning, which has been used previously in clinical studies, involves creating an ITV from 4DCT images to encompass the tumor movement and delivering beam spots multiple times. This so-called "layer rescanning" blurs out the dose heterogeneities due to interplay effects between the scanning beam and the moving tumor. ITV-based deliveries with carbon ions were rescanned 10, 15 and 20 times to determine the appropriate number of rescans. 15 rescans were subsequently selected for deliveries with ITV-based rescanning.

The treatment plans in this study were created from 10 phase 4DCTs of a patient (patient 1) from the University of Texas MD Anderson Cancer Center in Houston, Texas and another (patient 2) from the Champalimaud Centre for the Unknown in Lisbon, Portugal. Patient 1 was a 59-year-old female, diagnosed with T2N2M1 adenocarcinoma and treated with SBRT. Patient 2 was an 83-year-old male, diagnosed with stage 4 NSCLC and was treated with single fraction radiotherapy. The tumor volume for patient 1 was 260 cc, located in the left lower lobe of the lung at 75 mm physical depth in the reference phase. The peak-to-peak motion from the 4DCTs was estimated at 22 mm. The tumor volume for patient 2 was 54.0 cc, and was located in the right lower lung lobe, near the chest wall. The peak-to-peak motion was estimated to be 19.5 mm. Treatment plans for patient 1 were delivered with

both carbon ions and protons, and treatment plans for patient 2 were delivered with protons. Patients with large tumor motion amplitudes were selected to severely test and compare motion mitigation approaches. That is, neither the selected patients nor the treatment plans were intended to be representative of typical clinical treatments.

Before dose distribution measurements began, we performed quality assurance procedures, including relative dosimetry using the methods described by Luoni *et al*. [152]. Measurements included dose output constancy, and beam spot stability. Dosimetry procedures are further described by Lis *et al*. [190]. The detector used in this study was calibrated according to the protocols described elsewhere [154, 190].

We measured dose distributions using an ionization chamber (IC) array detector (Octavius 1500 xdr; PTW, Freiburg, Germany). The IC array detector was placed within a 5-mm thick polymethylmethacrylate (PMMA) plastic holder and PMMA slabs were placed in front [51]. Each measurement with the IC array detector was repeated three times, with the IC array detector placed at three water equivalent depths corresponding to the distal, middle, and proximal ends of the PTV or ITV: 72 mm, 96 mm, and 110 mm for patient 1, and 95 mm, 107 mm, and 121 mm for patient 2. The phantoms were mounted on top of a computer-controlled motorized linear stage (M-414.2PD; Physik Instrumente (PI) GmbH, Karlsruhe, Germany), which was programmed to move with a uni-axial projection of the motion from the patients' 4DCTs, thus mimicking respiratory motion.

The delivered dose distributions were reconstructed onto a water cube (to verify dose calculations) and onto the 4DCT images (to project clinical outcomes). The reconstructions were performed by parsing the delivered dose data (DDD) log files from the M-DDS and motion information from motion log files [51], which provided information on the position of each delivered beam spot. The file information was then reformatted into the TRiP4D treatment plan format. TRiP4D was then used to calculate the absorbed dose distributions of

the reconstructed treatment plans in water and on the 4DCT images. Measured absorbed dose distributions were compared with delivery reconstructions in water and planned absorbed dose distributions in water, and dose reconstructions on the patient 4DCT images were used to assess dosimetric quality and estimate therapeutic outcomes.

Gamma index analysis was performed to confirm the accuracy of the planned and reconstructed absorbed dose distributions, both of which were calculated. Data measured with the IC array detector was compared with planned and reconstructed distributions, calculated on a water box phantom using a generalized gamma index analysis [151]. Gamma index pass rates of > 90 % were considered acceptable.

The ideal dosimetric characteristics of successful motion management are high uniformity, tumor coverage, and conformity, as well as the absence of hotspots. Each of these were assessed from dose volume histogram (DVH) data derived from dose distributions from treatment plans or dose reconstructions on the patient 4DCT images. The first of these, dosimetric uniformity, was assessed with the homogeneity index $HI = D_5 - D_{95}$, where D_5 and D_{95} are the percent of the prescription doses that cover 5 % and 95 % of the PTV, respectively [150]. An HI of 0 % is ideal. Target dose coverage is the relative volume of the PTV that receives at least 95 % of the prescription dose, and it is represented by V_{95}. A V_{95} of 100 % is ideal and 95 % is commonly considered clinically sufficient target coverage of the prescription dose [191]. The extent of hotspots or overdose, V_{107}, is the relative target volume that receives over 107 % of the prescription dose, and 0 % V_{107} is ideal. Finally, dose conformity number (CN) is calculated by $CN = \frac{V_{T,p}}{V_T} \times \frac{V_{T,p}}{V_p}$, where $V_{T,p}$ is the volume of the target which receives a dose that is greater than or equal to the prescription dose, V_T is the PTV of the target, and V_p is the volume that receives a dose that is greater than or equal to the prescription dose [36]. It was used to assess the degree of conformity of the irradiated volume to the target volume. The ideal value on CN is 100 %, but this is rarely achieved in practice.

6.2.2 Comparison of Proton and Carbon Ion Treatment Plan Deliveries

We omitted dose constraints on normal tissues during the plan optimization process to facilitate comparisons between delivery approaches. However, to confirm that the resulting plan libraries were still clinically realistic, DVHs for lung and heart volumes were compared to the Quantitative Analyses of Normal Tissue Effects in the Clinic (QUANTEC) dose criteria [192]. The selected criteria were calculated with the equivalent dose formula [193]. The mean absorbed dose for symptomatic pneumonitis in the lung was < 14.1 Gy for 2.5 Gy fractions, which is expected to have a 10 % complication rate, and a V_{30} < 46 % for pericarditis, which is expected to have a complication rate of < 15 %. Mean doses were calculated for each structure from the cumulative DVHs of the lung and heart for static, MP4D deliveries, and ITV rescanned deliveries.

6.2.3 NTCP and TCP Calculations

We estimated, in a rudimentary manner, therapeutic outcomes for each delivery in order to check if the dosimetric finding are of clinical importance. Outcomes depend, in a complex way, on treatment factors, including dose, dose rate, irradiated volume, radiation quality (*e.g.*, particle types and energy distributions), and other factors. They also depend on host factors, such as sex, age, tissue, endpoint, timepoint, and inter-patient variations in biologic responses. In this work, simplified the prediction methods for simplicity, brevity, and to avoid confounding our main (dosimetric) findings with complex biologic uncertainties.

The outcomes were predicted with normal tissue complication probability (NTCP) and tumor control probability (TCP) calculations [194]. The NTCP values were calculated for cumulative probabilities at 5 years after treatment for the following complications: lung pneumonitis and cardiac perfusion or pericardial effusion. TCP calculations estimated the likelihood of local tumor control (no recurrence) [195]. Ideally, NTCP is 0 % and TCP is 100 %, although this is rarely realized in practice. Several models exist for NTCP and TCP

calculations, including models that consider non-standard fractionation schemes [196], the effects of different dose regions [197, 198], and the radiosensitivity of the tissues [199]. For this study, an updated version of the Lyman Kutcher-Burman (LKB) model was used, which uses the equivalent uniform dose (EUD) to reduce dose distributions into a single equivalent dose value. NTCP and TCP calculations for each delivery strategy (MP4D, ITV-based with 15-rescans, and static) were then compared for a relative estimate of the clinical benefit of each. It must be emphasized that the TCP and NTCP models and calculations in this study were used to aid the interpretation of dosimetric differences of various motion management strategies. That is to say, they provide a rudimentary means to assess the potential clinical importance of the observed physical differences in various deliveries. The calculations are not intended to provide predictions of clinical outcomes for any other purpose.

The TCP and NTCP for the lung were calculated from differential DVHs (dDVH). The dDVHs were an output of dose reconstructions. The percentage of the prescription dose delivered to each voxel of the dDVH was converted to absorbed dose values per voxel (Gy/mm^3) by multiplying the percentage prescription dose by the prescribed absorbed dose per fraction (fx) to the PTV: 2.5 Gy. The biologically effective dose (*BED)* [200-202], factors in the dosimetric impact of the chosen fractionation scheme and of the tissue-specific dose response, with the α/β was calculated on each voxel with a *BED* calculation [200-202],

$$BED_i = n \times d_i \left(1 + \frac{d_i}{\alpha/\beta}\right) \quad (1)$$

where n is the number of fractions, d_i is the absorbed dose in each voxel ($Gy_{\alpha/\beta}/mm^3$), and α/β is dependent on tissue type, particle type and fractionation scheme. The α/β ratio is a quantity that describes a tissue's cellular response (cell killing or altered tissue function) to radiation. Low α/β ratios are associated with late responding tissues, whereas high α/β ratios are associated with early responding tissues. Values of α/β ratios of 4, 2.5 and 12 Gy [192]

were selected for the lung, heart and NSCLC tumor, respectively, for proton and carbon ion beams. Uncertainties in α/β ratios range from 0.5-2.1 Gy [203], 1.8-5.6 Gy [204], and 12-16 Gy [205], respectively. The variations in RBE wih beam quality (*e.g.*, linear energy transfer) were omitted for simplicity and clarity. The prescribed absorbed dose to the target volume was 2.5 Gy / fx. Following Sun *et al*. [206], we prescribed the number of fractions at 26.

The dose distribution information from the BED-adjusted absorbed dose per voxel was then reduced to a single equivalent uniform dose value (Gy_{EUBED}), called the Equivalent Uniform Dose (EUD). This equation is a power-law equation

$$EUD = \left(\sum_i v_i \times {D_i}^a \right)^{\frac{1}{a}} \tag{2}$$

where v_i is the i'th partial volume of the structure that receives a differential BED-adjusted absorbed dose of D_i, and a is an organ specific factor that is derived from clinical data. For this study, a values of 1, 3 and -10 were used for the lung, heart and NSCLC tumor, respectively, as reported by Emami *et al*. [207], Okunieff *et al*. [208], and with QUANTEC data [192]. These values were derived from photon therapy. The *EUD* was then used to calculate the TCP [209] and NTCP.

TCP was calculated with

$$TCP = \frac{1}{1 + \frac{tcd50^{4 \times \gamma 50}}{EUD}} \tag{3}$$

where *tcd50* is the tumor dose to control 50 % of tumors, and $\gamma 50$ is a unitless tumor-specific factor that describes the slope of the dose response curve. For this study, a *tcd50* value of 60 Gy and a $\gamma 50$ of 2 was selected for the NSCLC tumor. Other, more complex TCP models are available, but for the intents and purposes of this study, simplicity and brevity were favored in model selection.

The NTCP for the heart and lung dose were calculated with a serial and parallel model, respectively. For the lung and heart, the following logistical function [200, 210, 211] was used:

$$NTCP = \frac{1}{1 + \frac{td50}{EUD}^{4 \times \gamma 50}} \quad (4)$$

where *td50* is the maximum tolerance dose for a 50 % complication rate within 5 years [207], and γ*50* is a unitless organ-specific parameter that describes the slope of the dose response curve. Reported values for γ*50* are 0.97 – 2 [192, 211], and 0.94 – 3 [200] for the lung and heart, respectively, and reported values for *td50* are 24.5 – 40 Gy [207, 212], and 48 – 57 Gy for the lung and heart, respectively. For this study, γ*50* of 2 and 0.94 were selected for the lung and heart, respectively [54, 58], and *td50* values of 30.8 Gy and 50 Gy were selected for the lung and heart, respectively [207, 211, 213].

6.3. Results

We assessed the dosimetric quality of MP4D deliveries with protons and carbon ions and compared the corresponding results from ITV-rescanned deliveries, static deliveries, and uncompensated deliveries, using the metrics described in section 6.2.3.

First, we used the generalized gamma index analysis [151] to calculate the agreement between the IC detector array measurements and planned dose distributions in water. The purpose of comparing measured and planned dose distributions was to quantify the impact motion-related dose defects. Figure 6.1 plots gamma index pass rates (and Pearson correlation score) for static, uncompensated, ITV-based deliveries with 15 rescans, and MP4D deliveries. Similar analyses were performed for ITV-based deliveries with 10, 15 and 20 rescans, using carbon ions. Pass rates for these deliveries were 100.0 % (Pearson correlation score of 0.993), 100.0 % (0.993), 80.9 % (0.992), respectively. ITV-based

deliveries with 15 rescans were selected for further study with proton ions due to faster delivery times and higher pass rates, relative to deliveries with 20 rescans. Moreover, low pass rates were found for uncompensated deliveries due to the significant dose heterogeneities produced by interplay effects in the absence of motion mitigation. The pass rates for the MP4D deliveries were relatively lower than ITV and static deliveries, as well, due to incomplete gating, as described further below.

Second, we quantified the agreement between reconstructed and measured dose distributions using the generalized gamma index analysis. The purpose of comparing measured and reconstructed dose distributions was to validate the accuracy of the dose reconstruction method. Pass rates were generally higher for reconstructed and measured dose distributions than they were for planned and measured dose distributions. The results for static, uncompensated, and ITV deliveries with 15 rescans, were > 90 % for seven of the eight cases, indicating a high degree of correlation between reconstructed and measured data, and results for MP4D deliveries were 96.0 % (0.996). The average pass rates for the MP4D dose reconstructions were approximately 10.7 % and 1.8 % higher than the gamma index analysis results for the planned dose distributions for carbon ion and proton dose deliveries, respectively. This suggests that the differences between planned and delivered dose distributions were mainly due to an experimental problem of incomplete beam gating through radiofrequency knockout (RFKO) rather than an inherent limitation of the conformal, MP4D approach. (The incomplete gating was a performance defect of the delivery system that was addressed subsequent to the completion of the experimental portions of this study.) This was confirmed by assessing measured particle counts during incomplete beam gating. This revealed that incomplete gating increased the delivered particles by up to 9.0 % more than were called for in the treatment plan.

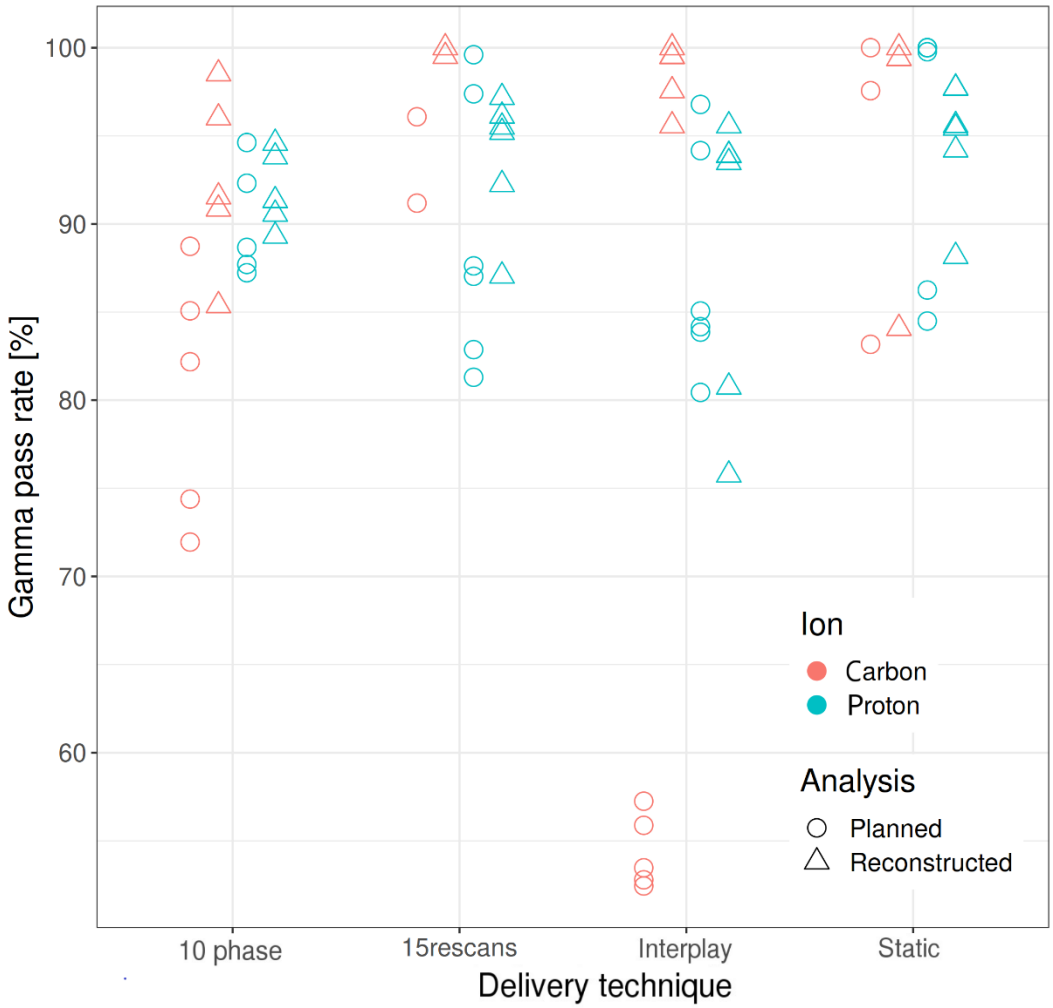

Figure 6.1. A summary of gamma index analysis results for multi-phase 4D deliveries (10 phase), ITV-based deliveries with 15 rescans, uncompensated (interplay) and static deliveries with criteria of 3 % dose difference and 3 mm distance to agreement. Carbon ion deliveries are represented in red and proton deliveries are represented in blue. Gamma index analysis results comparing planned dose distributions to measurements are represented as circles, while results comparing reconstructed log file dose distributions measurements are represented as triangles.

DVH data was used to calculate four dosimetric quality metrics: conformity number (*CN*) and homogeneity index (*HI*), dose coverage (V_{95}) and overdose (V_{107}) for each delivery. Results are summarized in Error! Reference source not found. The MP4D approach generally p rovided favorable outcomes, however, delivery artifacts (with incomplete beam gating) compromised carbon ion delivery results. The average CN for the MP4D deliveries was 57.3 %, which are more conformal than ITV rescanned (48.7 %) and static deliveries (53.7 %). V_{107} results were 0.0 % for rescanned, ITV deliveries and static deliveries. In

contrast, MP4D deliveries showed V_{107} values of up to 60 % and 22 % for carbon ions and protons, respectively, likely due to incomplete beam gating. While this decreased the dosimetric quality for the MP4D deliveries, the overdose was concentrated in the target, and the conformity from carbon ion beams was still superior to the conformity of ITV based rescanned deliveries. Uncompensated deliveries also contained hotspots due to motion interplay effects. Similarly, *HI* results for static and rescanned ITV deliveries were, on average, below 10 %, while MP4D deliveries were as high as 30 % for carbon ion deliveries. In contrast, MP4D proton deliveries, which were delivered at higher speeds and required less beam gating, resulted in substantially more favorable values of V_{107} and *HI*. The dose coverage, V_{95}, was within typical clinically acceptable ranges for all deliveries, and average V_{95} values were 99.5 ± 0.37 %, 100 ± 0.03 % and 99.5 ± 0.54 %, for MP4D deliveries, static deliveries, and ITV deliveries with 15 rescans, respectively. These results are summarized in Figure 6.2. Broadly, this finding reveals that MP4D delivery resulted in the most conformal dose distributions, with a sharper dose fall off than in the ITV rescanned deliveries but with hotspots in the target.

6.3.1 Comparison of Proton and Carbon Ions

Delivery quality with carbon ions were compared to that with protons for patient 1 by assessing DVH data. Doses to two OARs, the heart and the normal tissue of the left (healthy) lung, were compared for each of the delivery strategies. Representative DVHs for both ions to the target volume and to the OARs are shown in Figure 6.4, for static deliveries, MP4D deliveries, and ITV-based deliveries with 15 rescans. In all cases, better dose coverage was achievable for carbon ions, and, for both motion mitigation strategies, lung sparing was greater for carbon ion deliveries. Lung and heart doses were highest for ITV deliveries with 15 rescans and lowest for MP4D deliveries. However, for MP4D deliveries with carbon ions, hotspots due to radiation leakage through the RFKO gating system compromised the dose

delivery results to the PTV and OARs, resulting in higher doses to regions of the heart. Carbon ion deliveries also had additional dose to the heart due to the fragmentation tail. These doses were lower for MP4D deliveries, possibly due to the higher conformity of this strategy. Coronal and sagittal planes for each delivery are shown in Figure 6.3.

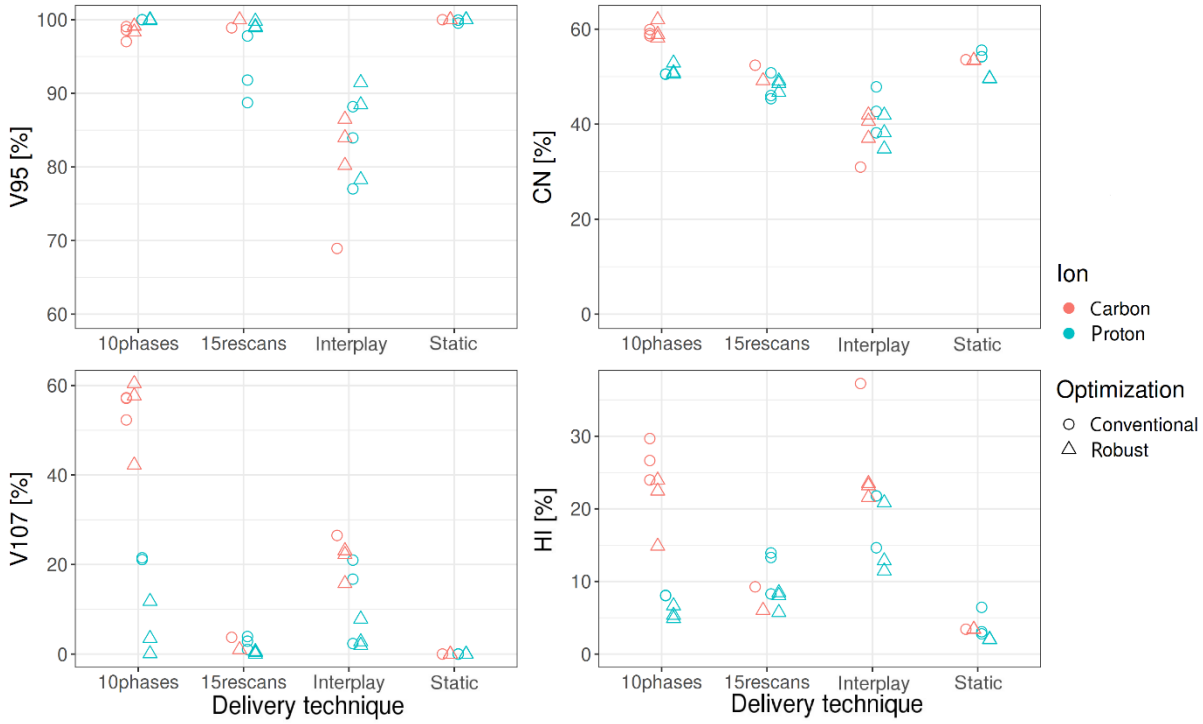

Figure 6.2. Selected delivery quality metrics, from dose-volume histogram data, including a) dose coverage, V_{95}, b) conformity, *CN*, the c) overdose, V_{107}, and d) homogeneity, *HI*, for carbon (red) and proton (blue) plans, for multi-phase 4D (10 phases) deliveries, ITV-based deliveries with 15 rescans, uncompensated deliveries (interplay), and static deliveries. Conventional 4D optimized deliveries are represented as circles and robust 4D optimized deliveries are represented as triangles.

We assessed the delivery reconstructions for compliance to QUANTEC clinical dose criteria to the lung and heart for patient 1. MP4D and static deliveries with carbon ions satisfied the criterion of less than 13 Gy mean dose to the normal tissue of the whole lung, as the calculated mean doses to were 5.4 Gy, 6.8 Gy, and 3.1 Gy, for static, ITV 15 rescan and MP4D deliveries, respectively. Proton deliveries also satisfied lung dose criteria in all cases and mean doses were 7.4 Gy, 8.1 Gy and 4.9 Gy, respectively. The heart criteria were met for all deliveries, and V_{30} results were 21.4 %, 22.4 %, and 8.6 % for static, 15 rescan, and MP4D

deliveries with carbon ions, and 20.9 %, 15.3 % and 9.1 % for static, 15 rescan, and MP4D deliveries with protons, respectively.

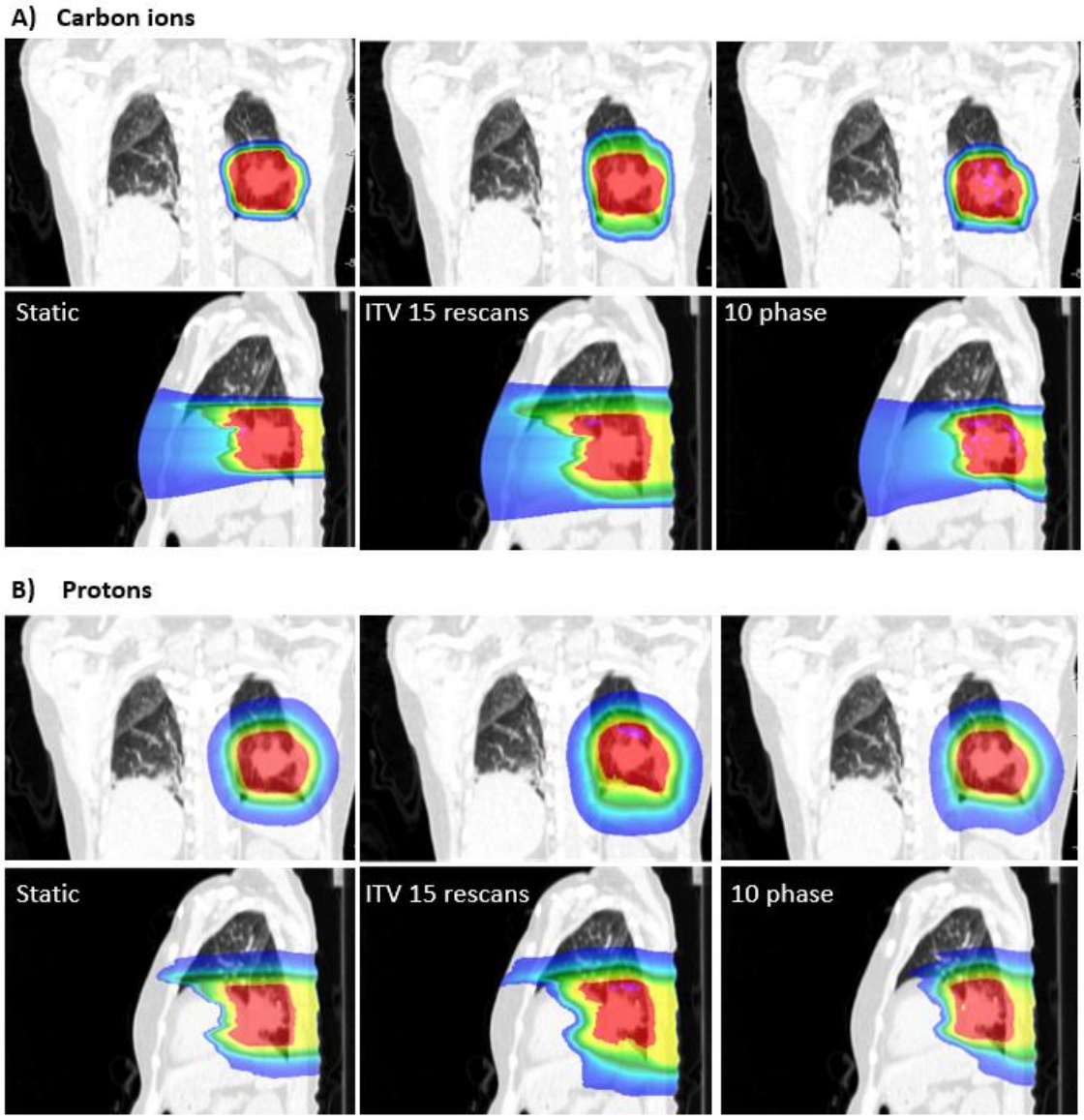

Figure 6.3. Coronal and sagittal planes of dose reconstructions on a 4DCT. Deliveries with a) carbon ions and b) protons are shown for static deliveries to a stationary target, ITV-based deliveries with 15 rescans, and 10-phase multi-phase 4D dose deliveries (MP4D).

Carbon ion patient plans were compared with proton patient plans, for MP4D deliveries, static deliveries, and ITV-based deliveries with 15 rescans with several DVH metrics, including *CN*, V_{95}, V_{107}, and *HI*, as described in section 6.2.2. Results of these comparisons are summarized in Table 6.1.

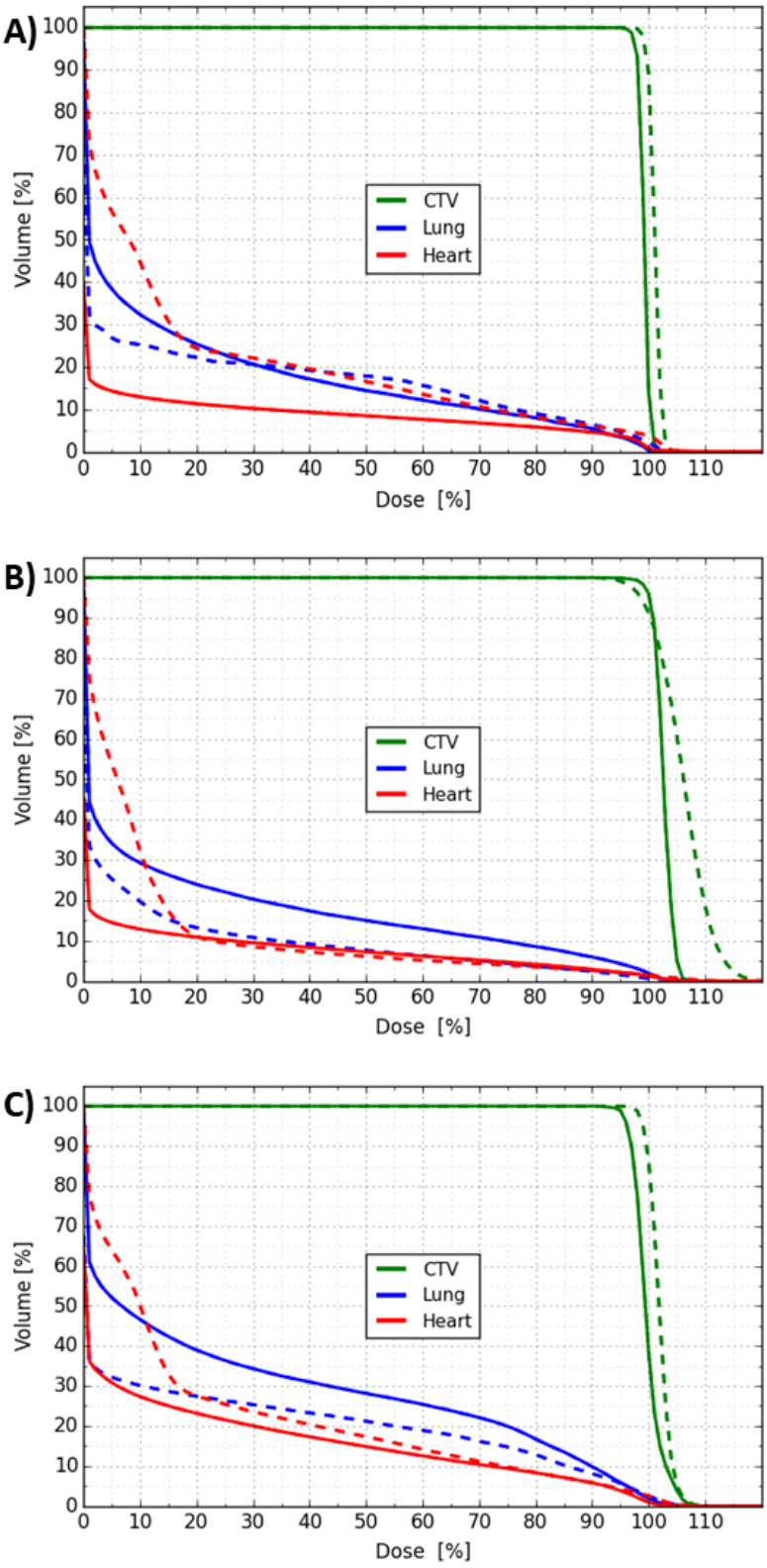

Figure 6.4. Plots of the volume doses to the target volume (green lines), the heart (red lines) and lung (blue lines) of patient 1 for 2.5 Gy, delivered with carbon ions (represented a dashed lines) and protons (represented as solid lines) to a) static, b) 10-phase multi-phase 4D deliveries c) 15 rescans ITV, reconstructed from log files (DDD).

Table 6.1. Table of average result values for dose volume histogram (DVH) metrics and projected therapeutic outcomes for patients 1 and 2. Static deliveries to a static target, multi-phase 4D deliveries (MP4D), and ITV-based rescanning deliveries were made with carbon ion and proton beams.

DVH Metric	Patient 1						Patient 2		
Delivery strategies	Static		MP4D		ITV rescanned		Static	MP4D	ITV rescanned
Ion	Proton	Carbon	Proton	Carbon	Proton	Carbon	Proton		
D_{95} (%)	98.2	99.4	101.4	99.0	96.2	97.3	99.4	95.5	96.1
V_{95} (%)	100.0	100.0	100.0	99.1	98.9	98.9	99.8	97.6	97.0
V_{107} (%)	0.0	0.0	2.9	42.2	0.6	1.0	0.0	0.0	3.3
CN (%)	49.6	53.3	50.8	61.7	48.6	52.4	33.7	36.9	31.7
HI (%)	2.0	1.4	2.1	6.0	3.4	3.3	1.5	3.0	4.2
Heart NTCP (%)	13.0 (9.1 - 15.6)	15.6	7.7 (6.5 - 8.5)	6.9 (6.1 - 7.9)	11.5 (9.0 - 13.5)	12.3 (9.2 - 15.3)	0.0 (0.0 - 0.0)	0.0 (0.0 - 0.0)	0.0 (0.0 - 0.0)
Lung NTCP (%)	0.3 (0.0 - 0.5)	0.0 (0.0 - 0.0)	0.0 (0.0 - 0.0)	0.0 (0.0 - 0.0)	0.7 (0.1 - 1.6)	0.1 (0.1 - 0.1)	0.0 (0.0 - 0.0)	0.0 (0.0 - 0.0)	0.0 (0.0 - 0.0)
Tumor EUD (Gy_{EUBED})	67.1 (67.0 - 71.5)	68.6 (68.6 - 68.6)	70.8 (67.6 - 71.)	73.2 (71.6 - 75.5)	67.2 (66.8 - 67.4)	68.9 (68.1 - 69.1)	67.2 (67.1- 67.3)	66.5 (65.6 - 67.5)	65.6 (65.3 - 66.0)
TCP (%)	71.0 (70.8 - 80.3)	74.4 (74.4 - 74.4)	77.8 (76.9 - 80.4)	82.1 (80.5 - 82.8)	71.2 (70.1 - 71.6)	75.1 (74.7 - 75.6)	71.2 (70.8 - 71.6)	69.3 (67.2 - 71.9)	67.1 (66.2 - 74.1)

6.3.1.1. NTCP and TCP Calculation Results

NTCP and TCP values were calculated for two patients: patient 1, planned with protons and carbon ions, and patient 2, planned with protons. Results are summarized in Table 6.1. For patient 1, 10 phase MP4D deliveries had the most favorable therapeutic outcomes for TCP calculations and for NTCP calculations of the heart and lungs for deliveries with proton and carbon ion beams. Notably, heart NTCP values were only 7.7 % and 6.9 %, respectively, for the MP4D approach, while heart NTCP values were 13.0 % and 15.6 % for static deliveries. Due to the tumor location in patient 2, all delivery results showed favorable NTCP and TCP results. Uncertainties for several parameters, including a, α/β, γ_{50}, td_{50} and tcd_{50} produced significant uncertainties for NTCP and TCP calculation results [192, 200, 208, 211, 213, 214]. Specifically, variations in γ_{50} and tcd_{50} values varied TCP results for NSCLC tumors from as low as 58 % to as high as 91 % for motion compensated proton deliveries.

6.4. Discussion

In this study, we investigated the dosimetric quality and projected therapeutic outcomes from two approaches to treating moving tumors: multi-phase 4D (MP4D) deliveries and ITV-based deliveries with rescanning. We delivered patient plans using both methods, with proton and carbon ions, and demonstrated the new, MP4D approach yielded superior dosimetric quality compared to other delivery approaches. The major finding of this work is that the MP4D approach can be effective at mitigating tumor motion, and potentially reducing the risk of treatment side effects. The specific results of this study suggest that the higher conformity of MP4D deliveries, combined with the sharper dose falloff of carbon ion therapy can be maintained when tumor motion is effectively mitigated, resulting in greater tissue sparing than other approaches. Further, we demonstrated that carbon ions are favorable to protons for conformal deliveries, as carbon ions result in a steeper dose falloff; however,

these results only impact organs directly adjacent to the tumor that are not located in the fragmentation tail. The hotspots seen in this study for carbon ion deliveries were due to defects in the gating system rather than limitations of the MP4D approach.

The implication of this study is that MP4D deliveries, based on 4D optimized plan libraries, appears to be a promising approach to achieve the necessary dosimetric quality and outcomes, compared to other motion mitigation strategies with ion beams. These pre-clinical results are preliminary in nature and part of a larger effort to develop and validate a modular M-DDS.

This work is the first reported implementation of a dose delivery system with integrated capabilities for conformal, MP4D deliveries of scanned ion beams. The results of this study are comparable to previous work in motion mitigation studies at GSI, and to delivery results for motion mitigation at the National Institute of Radiological Science (NIRS). At GSI, planning studies have been performed to predict the dose delivery quality of motion mitigation strategies, including 4D rescanning (here referred to as MP4D) and beam tracking [29]. The reported results at GSI were a V_{95} of 98.5 %, 72.5 %, 99.4 % and 98.5 % for static, uncompensated, 4D rescanning and tracking plans, respectively. In comparison, we predicted average values of V_{95} of 100 %, 98.9 % and 99.1 % for static deliveries, ITV-based deliveries with 15 rescans, and MP4D deliveries, respectively. As the work by Graeff *et al*. [23] was a treatment planning study, additional uncertainties, including residual motion and noisy particle delivery rates were not factored in. At NIRS, phase-controlled rescanning is used along with fluoroscopically gated deliveries. Typical dosimetric quality results listed by Mori, *et al*. [215] were $D_{95} > 95$ %. Reported limitations included the inability to modify delivery in response to significant changes to the tumor baseline. The NTCP and TCP calculations used in this work are similar to Gay *et al*. [200] and Niemierko *et al*. [216]. To our knowledge, no NTCP and TCP assessments have been performed for comparing motion

mitigation strategies. This study has been performed with absorbed dose calculations rather than biological dose calculations, due to the persistence of high uncertainties in α/β ratios. Due to the high RBE for NSCLC tumors and relatively RBE in surrounding normal tissue, carbon ion therapy is thought to be particularly beneficial for treating lung tumors.

This study has several strengths. First, the methods for assessing dosimetric quality are commonly used at ion therapy clinics, including CNAO and NIRS [35, 87]. Further, we considered relevant factors when designing the programs and selecting algorithms for NTCP and TCP analysis, including using a serial NTCP model to consider the partial volumes of the heart and a parallel model for the lungs, and factoring the fractionation scheme by performing BED calculations. Additionally, this study uses a portable and modular device (M-DDS), described in detail by Lis *et al*. [51]. This will be important to address open research questions regarding more effective methods for tumor motion compensation. For this purpose, the M-DDS has several motion mitigation strategies integrated into a modular unit, including gating, ITV-based rescanning, tracking and MP4D deliveries. The M-DDS is also available at both CNAO and at GSI for research on motion mitigation. The M-DDS is a version of the DDS used clinically at CNAO, with modification for motion mitigation, so the clinical safety features from the original DDS are in place. Safety and performance assessments have been performed on the motion additions of the M-DDS [51], and the plan libraries for MP4D deliveries described in this study have been delivered to phantoms at CNAO. Finally, the results of this work show that the MP4D approach is versatile enough to deliver both proton and carbon ions conformally and results in outcomes that are above the clinical standards. This presented strategy can be extended to other ion species, including helium ions and radioactive ion beams [217] and can be used with both synchrotrons and cyclotrons.

One limitation of this study is that it considered only two patients and a limited number of treatment plans. However, this is not a serious limitation because, with the methods and infrastructure we have now demonstrated, additional studies were initiated and are underway to generate additional data that aim to inform the process of translating the M-DDS from the laboratory to the clinic. Another limitation of this study is the simple methods used to project therapeutic outcomes. This is not currently a serious limitation, because the physical performance issues are the main challenges facing the continued development of the motion mitigation strategies considered here. Much pre-clinical work remains to be done on beam delivery, *e.g.,* advances in gating and monitoring patient respiratory motion. Hence, the purpose of the outcome calculations was only to provide a rudimentary context for the observed dosimetry findings. After the M-DDS has been commissioned for clinical use, more detailed outcome projections will become an essential part of the pre-clinical research. Additionally, the MP4D deliveries were performed under ideal respiration, in the absence of uncertainties due to irregular motion, such as variations in the breathing cycle patterns and an imperfect correlation between the motion signal and the actual target motion. A more exhaustive study on the benefits of conformal motion mitigation with carbon ions and protons must still be performed. Another limitation was that the radiofrequency knockout extraction gating method was not fully tuned at GSI, resulting in significant hotspots in the dose distributions for the MP4D deliveries. Ideally, we would have delivered these plans at a clinical facility as well, where fast magnets dump the beam entirely during a gate. Nevertheless, the contributions of the leakage particles were quantified, and the data was analyzed with consideration of the contributions to the dose distributions. Another limitation was that the carbon ion plan libraries were delivered with absorbed dose calculations rather than biological doses. This would have increased the complexity of the carbon ion deliveries, but also would have further increased the peak to plateau ratio in comparison to proton

deliveries. As lung is a late responding tissue, the RBE is greater for the tumor, and could result in more favorable NTCP and TCP results. In future studies, we will investigate motion mitigation with RBE-weighted, physically inhomogeneous doses, as must be applied in clinical practice. Finally, though we considered subregions for the heart, we did not consider subregions of the tumor volume, which can have an increased radio-resistance in certain regions, resulting in decreased tumor control [218]. This is not a major limitation, as carbon ion therapy already has been shown to be more effective in treating radioresistant tumors [184]. Further investigation on the therapeutic gain of carbon ions for NSCLC tumors are beyond the scope of this manuscript.

This study is part of a larger project to develop a modular, motion-synchronized dose delivery system for clinical use. In the next stages, several of the limitations of this study, noted above, will be addressed. For example, MP4D deliveries will be performed with irregular motion, and the M-DDS will be expanded to correct for changes in the detected motion trajectory (so-called “corrective tracking”) and to accept diverse forms of motion trajectory information, including 3D displacement vectors. The M-DDS will later be transferred to CNAO for pre-clinical testing.

6.5. Conclusion

The results of this work support that the multi-phase 4D dose delivery (MP4D) approach can deliver ion beam treatments with favorable treatment quality and projected therapeutic outcomes compared to other motion mitigation approaches. The M-DDS used in this work is modular, portable design that has a variety of motion mitigation strategies incorporated. Compared to static deliveries and ITV-based deliveries with rescanning, the MP4D approach is more conformal, resulting in reduced projected normal tissue complications.

Chapter 7. Discussion and Conclusions

This work has developed and tested a portable, modular dose delivery system for investigating ion therapy treatment strategies, including the multi-phase 4D dose delivery approach to motion mitigation. The motion-synchronized dose delivery system (M-DDS) was developed as part of a framework for research in novel ion therapy solutions and for comparing delivery strategies. This necessitated integrating the clinically certified DDS from CNAO into a research facility, developing motion mitigation solutions, integrating a comprehensive risk analysis strategy to verify the safety of new technologies, and developing experiment protocols to validate performance. The major finding of this study was that the MP4D approach can deliver conformal, motion-synchronized beams to clinically acceptable performance, dosimetric quality and safety standards.

7.1. Implications

The results of this study suggest that treatment outcomes for moving tumors can be improved by delivering conformal, motion synchronized ion beams. With the delivery strategy developed here, it is possible to consider full anatomical motion information from 4DCT images during the planning process, allowing for uniform and conformal, free-breathing treatments. This method may provide a radiotherapy method for treating tumors such as radioresistant, late-stage NSCLC tumors and pancreatic tumors, which are often located near critical organs and can benefit from more conformal treatments. Moreover, the motion mitigation strategy has been implemented with a modular, portable design, which can be utilized at multiple centers. This compatibility allows for more coherence when performing multi-institutional studies and for performing pre-clinical testing before adopting new treatment methods, beyond motion mitigation strategies, into clinical practice. In order for particle therapy to expand to other treatment methods, including using radioactive ion beams, mixed beams and Flash therapy, accelerators that are capable of providing the

necessary beam conditions will be needed. The M-DDS has been implemented in one such accelerator and was developed from a clinically certified DDS, allowing for testing new delivery strategies in clinic-like conditions before translation into the clinical use (Chapter 2 and 3). Furthermore, the motion mitigation strategy was implemented into a clinically certified delivery system, and a prospective risk analysis has been performed to confirm and maintain the safety of the DDS and its suitability for clinical use (Chapter 4). The developed M-DDS is not a singular solution for motion mitigation, but can be expanded to include other motion mitigation solutions, including tumor tracking. In further studies, the M-DDS with be expanded to include solutions for treating irregular motion.

7.2. Coherence with Existing Literature

Though many proton and ion therapy clinics regularly use motion handling strategies such as respiratory gating and breath holds, few integrated motion compensation strategies have been implemented into clinical delivery systems. Therefore, it is difficult to draw direct quantitative comparisons with other existing methods. The phase-controlled rescanning method, used clinically at NIRS [219], synchronizes scanned ion beam delivery with tumor motion by enabling beam delivery when the tumor is detected to be within a gating window. Our strategy provides comparable results, as the motion compensated ellipsoid deliveries produced 3 % homogeneities with the phase-controlled rescanning method at NIRS [38] and 5 % homogeneities with the motion-synchronized delivery approach at GSI and CNAO (Chapter 5). Though the phase-controlled rescanning method has shown excellent dose distributions, there is no manner to correct for changes to the respiratory motion amplitude during delivery, and the low duty cycle of respiratory gating relies on faster delivery methods. In contrast, our method considers the respiratory patterns measured during acquisition of 4DCT images and delivers ion beams throughout the respiratory cycle, which allows for inherent compensation of heterogeneous tissue motion and up to 100 % duty

cycles. The M-DDS can also be expanded to allow for applying corrective tumor tracking vectors to the delivery position, allowing for modifying the beam delivery to changes in the measured breathing pattern, such as baseline drifts. Previously, the tracking method has been studied at GSI [157]. This study determined that accuracies of up to 0.16 mm were achievable in the lateral direction, while only a 1 mm accuracy was theoretically achievable with longitudinal tracking. Though this strategy showed promising results, the delivery system contained unreconcilable problems with memory capacity and delivery timing, rendering the design unsuitable for the clinic. Additionally, delivery problems related to differing motion between the target and entrance channel (the inverse interplay effect) and when tumor motion was not only translational limited the performance of the tracking method [26]. Treatment planning studies on 4D-optimized delivery [29] predicted high treatment quality results, including a delivery uniformity of 2.2 %.

7.3. Strengths of this Study

This study has several notable strengths. First, we designed the motion mitigation additions of the M-DDS to be modular and portable. The M-DDS was integrated into the GSI research facility with minimal changes to the internal software by designing an adaption layer of interfaces between the M-DDS and the beam nozzle component interfaces. This allows for straightforward implementation into other institutes, which can aid in performing larger, international research studies, including multi-institutional clinical trials for light ion therapy. Additionally, the modular design of the M-DDS is flexible and expandable, as it allows for interchanging components for different functionalities and implementing a variety of motion-mitigation techniques for comparison. We demonstrated this versatility by delivering motion compensated and static deliveries, with and without the motion mitigation module, respectively, at two facilities. Second, we applied well-established methods for our analyses. More specifically, we performed a comprehensive, prospective risk analysis, based on the

established recommendations of the AAPM [103], and used detectors and set-ups (*i.e.*, 2D IC detector arrays, radiochromic films, and small-volume ICs) that are recommended by the AAPM task group 224 report [101], as well as analysis methods commonly used in the clinic (*i.e.*, the homogeneity index, the gamma index analysis and the conformity index). Finally, we performed our studies at both CNAO and at GSI at various stages. This allowed us to verify the performance of the motion-synchronized dose delivery strategy under a variety of delivery conditions, including higher particle intensities, two beam gating modes, two energy modulation modes, a variety of beam nozzle elements, and in the presence of clinical interlocks.

7.4. Limitations of this Study

This study is not free of limitations. First, we did not perform an in-depth characterization of the performance of each beam nozzle component implemented into the research facility. Several components were maintained from the pilot study performed at GSI and a subset of validation tests were performed to verify the functionality of these components. Additionally, some peripheral components were still in development during the course of this study. These components, such as the position monitor readout interfaces, will be validated in a future study. A second limitation is that we did not validate the M-DDS with irregular motion, including baseline drifts, changes to the breathing cycle amplitude and duration, or sudden changes, such as coughs. However, the treatment quality of the M-DDS has been validated using recorded patient breathing information, as described in Chapter 6, and the modular design of the M-DDS will allow for expansion and implementation of additional motion mitigation features and motion mitigation approaches. Further solutions for mitigating irregular motion patterns, such as corrective tracking, are beyond the scope of this study and must still be implemented and tested. Nevertheless, the current M-DDS is a transferable product, which can be translated into the clinic. Additionally, the delivery quality

and therapeutic outcomes of motion-synchronized deliveries have only been quantified for two patient plans. This is not a major limitation, as the selected patients were cases that are challenging to treat, and our finding support that MP4D delivery of 4D-optimized plan libraries provides favorable treatment outcomes. Additionally, planning studies with 4D-optmization have been performed previously with more patient plans [29, 51]. Nevertheless, further studies must be performed to conclusively confirm the clinical efficacy of this approach. Moreover, we have only compared the motion compensation strategy to one clinically approved motion handling strategy (ITV-based rescanning) at two facilities (GSI and CNAO) and an in-depth comparison with other clinical methods, including phase-controlled rescanning and gating, and a combination of methods should still be performed. Finally, the dose calculations in this study were only performed with the treatment planning system found at GSI, TRiP4D. This planning system has been used in patient treatment from 1997-2008 and has been experimentally verified under diverse conditions [26]. Nevertheless, no independent calculations, such as Monte Carlo calculations, were performed. This is not a major limitation, as film and 2D IC detector measurements from experiments at GSI and CNAO compared to dose distributions simulations created from TRiP4D were in good agreement.

7.5. Conclusion

This work has demonstrated that a motion-synchronized approach can provide a clinical viable and generalizable approach to motion mitigation with scanned ion beams. The M-DDS is an example solution of a framework for integrating the development and clinical testing of therapy methods. We have designed and implemented a modular and portable dose delivery system with integrated motion mitigation capabilities. Our safety risk analysis has revealed several safety risks that are unique to the M-DDS and appropriate solutions were proposed and tested. Accordingly, the M-DDS was shown to be a safe, clinically viable solution for

motion compensation. Additionally, we have determined that the multi-phase 4D dose delivery strategy compensated for heterogeneous anatomical motion with minimal degradations to the dose distributions. In conclusion, this work provides a comprehensive pre-clinical study on the modular, motion-synchronized dose delivery system for delivering conformal dose distributions to moving targets.

Appendix. Copyright Information

Chapter 2. Copyright agreement

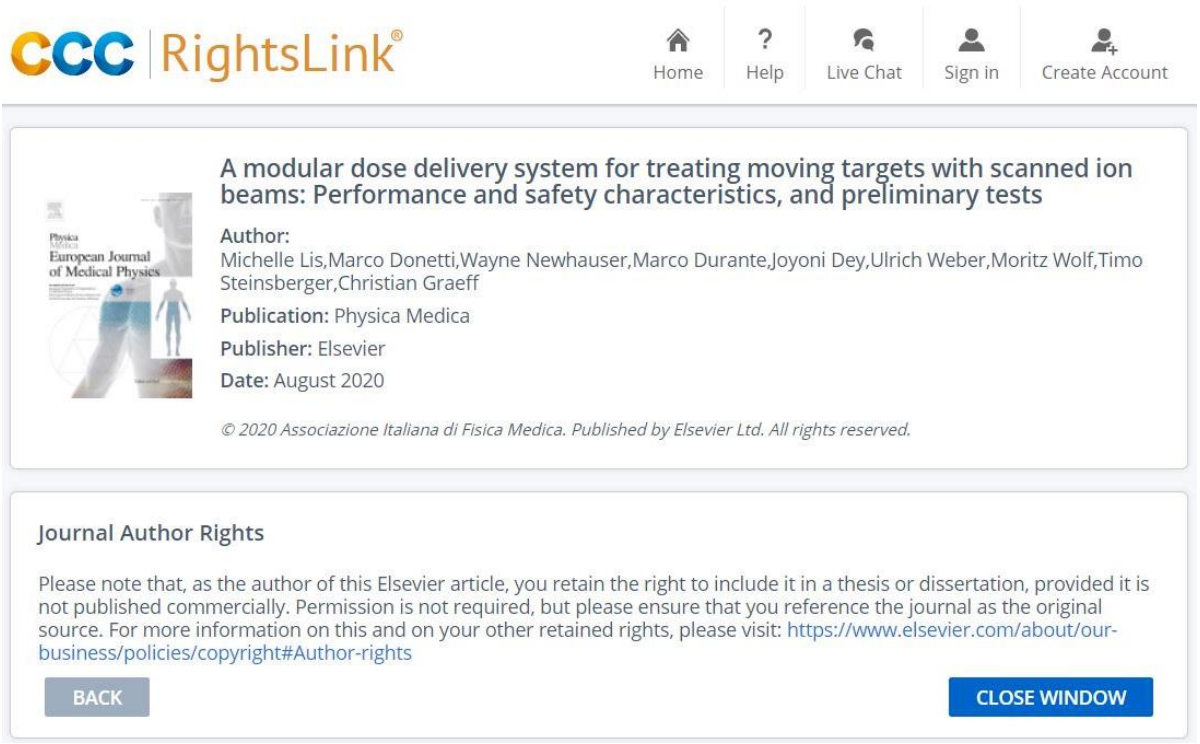

Chapter 3. Copyright agreement

Dear Michelle,

Thank you for your request to reproduce content from Journal of Instrumentation.

The content you have requested was published under a CC BY licence which permits reuse for any purposes, even commercial, provided the licence terms are adhered to.

Therefore you may reuse the content without permission, so long as you reference it adequately and adhere to the terms of the CC BY licence.

Please note this does not apply to any content/figure which is credited to another source in our publication or has been obtained from a third party, which is not available under a suitable open access licence. Express permission for such content/figures must be obtained from the copyright owner.

Chapter 4. Copyright agreement

Works Cited

1. *Global Cancer Facts & Figures 4th Edition*, A.C. Society, Editor. 2018, American Cancer Society: Atlanta.

2. Siegel, R.L., K.D. Miller, and A. Jemal, *Cancer statistics, 2019.* CA: A Cancer Journal for Clinicians, 2019. **69**(1): p. 7-34.

3. Arnold, M., et al., *Progress in cancer survival, mortality, and incidence in seven high-income countries 1995–2014 (ICBP SURVMARK-2): a population-based study.* The Lancet Oncology, 2019. **20**(11): p. 1493-1505.

4. Yang, H., et al., *Clinical analysis of conformal and intensity-modulated radiotherapy in patients with recurrent ovarian cancer.* Scientific Reports, 2020. **10**(1): p. 17172.

5. Kilburn, J.M., et al., *Image guided radiation therapy may result in improved local control in locally advanced lung cancer patients.* Practical Radiation Oncology, 2016. **6**(3): p. e73-e80.

6. Tsujii, H. and T. Kamada, *A review of update clinical results of carbon ion radiotherapy.* Jpn. J. Clin. Oncol, 2012. **42**(8): p. 670-685.

7. Serizawa, T., *Radiosurgery for metastatic brain tumors.* International Journal of Clinical Oncology, 2009. **14**(4): p. 289-298.

8. Gao, J., et al., *Salvage Carbon-Ion Radiation Therapy For Locoregionally Recurrent Head and Neck Malignancies.* Scientific Reports, 2019. **9**(1): p. 4259.

9. Kamada, T., et al., *Carbon ion radiotherapy in Japan: an assessment of 20 years of clinical experience.* The Lancet Oncology, 2015. **16**(2): p. e93-e100.

10. Suit, H., et al., *Proton vs carbon ion beams in the definitive radiation treatment of cancer patients.* Radiotherapy and Oncology, 2010. **95**(1): p. 3-22.

11. Califf, R., *Institute of Medicine (US) Roundtable on Translating Genomic-Based Research for Health.*, in *Translation of Innovations.* . 2008, National Academies Press (US): Washington (DC).

12. Ren, Y., et al., *Clinical translation of the assets of biomedical engineering – a retrospective analysis with looks to the future.* Expert Review of Medical Devices, 2019. **16**(11): p. 913-922.

13. Mori, S., et al., *Systematic evaluation of four-dimensional hybrid depth scanning for carbon-ion lung therapy.* Med Phys, 2013. **40**(3): p. 031720.

14. Eley, J.G., et al., *4D optimization of scanned ion beam tracking therapy for moving tumors.* Phys. Med. Biol, 2014. **59**(13): p. 3431-3452.

15. Zhang, Y., et al., *Online image guided tumour tracking with scanned proton beams: a comprehensive simulation study.* Physics in Medicine and Biology, 2014. **59**(24): p. 7793-7817.

16. Prall, M., et al., *Ion beam tracking using ultrasound motion detection.* Medical Physics, 2014. **41**(4): p. 041708.

17. Trnková, P., et al., *Clinical implementations of 4D pencil beam scanned particle therapy: Report on the 4D treatment planning workshop 2016 and 2017.* Physica Medica: European Journal of Medical Physics, 2018. **54**: p. 121-130.

18. Bert, C., et al., *Target motion tracking with a scanned particle beam.* Medical Physics, 2007. **34**(12): p. 4768-4771.

19. Negoro, Y., et al., *The effectiveness of an immobilization device in conformal radiotherapy for lung tumor: reduction of respiratory tumor movement and evaluation of the daily setup accuracy.* International Journal of Radiation Oncology*Biology*Physics, 2001. **50**(4): p. 889-898.

20. Tashiro, M., et al., *Technical approach to individualized respiratory-gated carbon-ion therapy for mobile organs.* Radiological Physics and Technology, 2013. **6**(2): p. 356-366.

21. Iwata, H., et al., *High-dose proton therapy and carbon-ion therapy for stage I nonsmall cell lung cancer.* Cancer, 2010. **116**(10): p. 2476-2485.

22. Mori, S., et al., *Conformity and robustness of gated rescanned carbon ion pencil beam scanning of liver tumors at NIRS.* Radiother Oncol, 2014. **111**(3): p. 431-6.

23. Reddy, V.Y., et al., *Prophylactic catheter ablation for the prevention of defibrillator therapy.* The New England journal of medicine, 2007. **357**(26): p. 2657-65.

24. Lüchtenborg, R., et al., *Experimental verification of a real-time compensation functionality for dose changes due to target motion in scanned particle therapy.* Med. Phys, 2011. **38**(10): p. 5448-5458.

25. Giordanengo, S., et al., *The CNAO dose delivery system for modulated scanning ion beam radiotherapy.* Med Phys, 2015. **42**(1): p. 263-75.

26. Richter, D., *Treatment planning for tumors with residual motion in scanned ion beam therapy*. 2012, Technical University Darmstadt: Darmstadt.

27. Krämer, M., et al., *Treatment planning for heavy-ion radiotherapy: physical beam model and dose optimization.* Physics in Medicine and Biology, 2000. **45**(11): p. 3299-3317.

28. Krämer, M. and M. Scholz, *Treatment planning for heavy-ion radiotherapy: calculation and optimization of biologically effective dose.* Physics in Medicine and Biology, 2000. **45**(11): p. 3319-3330.

29. Graeff, C., *Motion mitigation in scanned ion beam therapy through 4D-optimization.* Phys. Med, 2014. **30**(5): p. 570-577.

30. Anderle, K., et al., *In silico comparison of photons versus carbon ions in single fraction therapy of lung cancer.* Phys Med, 2016. **32**(9): p. 1118-23.

31. Graeff, C., et al., *A 4D-optimization concept for scanned ion beam therapy.* Radiother Oncol, 2013. **109**(3): p. 419-24.

32. Eley, J., et al., *Tracking moving tumors with a scanned carbon beam: Robustness to changing target motion characteristics and tracking uncertainties.* Medical Physics, 2011: p. TH-C-BRC-9.

33. Wolf, M., *Robust optimization in 4D treatment planning for carbon ion therapy of lung tumors*, in *Physics*. 2018, Technical University of Darmstadt: Darmstadt.

34. Low, D.A., et al., *A technique for the quantitative evaluation of dose distributions.* Medical Physics, 1998. **25**(5): p. 656-661.

35. Mirandola, A., et al., *Dosimetric commissioning and quality assurance of scanned ion beams at the Italian National Center for Oncological Hadrontherapy.* Medical Physics, 2015. **42**(9): p. 5287-5300.

36. van't Riet, A., et al., *A conformation number to quantify the degree of conformality in brachytherapy and external beam irradiation: application to the prostate.* Int. J. Radiat. Oncol. Biol. Phys, 1997. **37**(3): p. 731-736.

37. Huq, M.S., et al., *The report of Task Group 100 of the AAPM: Application of risk analysis methods to radiation therapy quality management.* Medical physics, 2016. **43**(7): p. 4209-4209.

38. Furukawa, T., et al., *Moving target irradiation with fast rescanning and gating in particle therapy.* Med Phys, 2010. **37**(9): p. 4874-4879.

39. Graeff, C., et al., *Multigating, a 4D optimized beam tracking in scanned ion beam therapy.* Technol Cancer Res Treat, 2014. **13**(6): p. 497-504.

40. Seregni, M., et al., *Tumor tracking based on correlation models in scanned ion beam therapy: an experimental study.* Phys. Med. Biol, 2013. **58**(13): p. 4659-4678.

41. Graeff, C., *Robustness of 4D-optimized scanned carbon ion beam therapy against interfractional changes in lung cancer.* Radiother Oncol, 2017. **122**(3): p. 387-392.

42. Cardin, A., et al., *Validation of high-resolution 3D patient QA for proton PBS and IMPT using laser CT of improved polymer gel dosimeters.* Journal of Physics: Conference Series, 2015. **573**: p. 012017.

43. Malouff, T.D., et al., *Carbon Ion Therapy: A Modern Review of an Emerging Technology.* Frontiers in Oncology, 2020. **10**(82).

44. Durante, M., R. Orecchia, and J.S. Loeffler, *Charged-particle therapy in cancer: clinical uses and future perspectives.* Nature Reviews Clinical Oncology, 2017. **14**(8): p. 483-495.

45. Durante, M. and J.S. Loeffler, *Charged particles in radiation oncology.* Nature Reviews Clinical Oncology, 2010. **7**(1): p. 37-43.

46. Haberer, T., et al., *Magnetic scanning system for heavy ion therapy.* Nucl. Instrum. Meth. A, 1993. **330**: p. 296-305.

47. Kitagawa, A., et al., *Review on heavy ion radiotherapy facilities and related ion sources (invited).* Review of Scientific Instruments, 2010. **81**(2): p. 02B909.

48. van de Water, S., et al., *Towards FLASH proton therapy: the impact of treatment planning and machine characteristics on achievable dose rates.* Acta Oncologica, 2019. **58**(10): p. 1463-1469.

49. Santos Augusto, R.M.d., *On the feasibility of using radioactive ion beams in hadrontherapy Dosimetric and imaging studies*. 2018.

50. Volz, L., et al., *Experimental exploration of a mixed helium/carbon beam for online treatment monitoring in carbon ion beam therapy.* Phys. Med. Biol., 2020. **65**(5): p. 055002.

51. Lis, M., et al., *A modular dose delivery system for treating moving targets with scanned ion beams: Performance and safety characteristics, and preliminary tests.* Physica Medica, 2020. **76**: p. 307-316.

52. Group, P.T.C.-O. *Particle therapy facilities in clinical operation* 2020; Available from: https://www.ptcog.ch/index.php/facilities-in-operation.

53. Schippers, J.M. and M. Seidel, *Operational and design aspects of accelerators for medical applications.* Physical Review Special Topics - Accelerators and Beams, 2015. **18**(3): p. 034801.

54. Eickhoff, H., et al., *The GSI Cancer Therapy Project.* Strahlentherapie und Onkologie, 1999. **175**(2): p. 21-24.

55. Tsujii, H., et al., *Overview of clinical experiences on carbon ion radiotherapy at NIRS.* Radiother. Oncol, 2004. **73**(S2): p. 41.

56. Abe, M., *Charged particle radiotherapy at the Hyogo Ion Beam Medical Center: Characteristics, technology and clinical results.* Proceedings of the Japan Academy. Series B, Physical and biological sciences, 2007. **83**(6): p. 151-163.

57. Ohno, T., et al., *Carbon Ion Radiotherapy at the Gunma University Heavy Ion Medical Center: New Facility Set-up.* Cancers, 2011. **3**(4): p. 4046-4060.

58. Combs, S.E., et al., *Particle therapy at the Heidelberg Ion Therapy Center (HIT) - Integrated research-driven university-hospital-based radiation oncology service in Heidelberg, Germany.* Radiother Oncol, 2010. **95**(1): p. 41-44.

59. Durante, M., et al., *All the fun of the FAIR: fundamental physics at the facility for antiproton and ion research.* Physica Scripta, 2019. **94**(3): p. 033001.

60. Zelefsky, M.J., et al., *Dose escalation with three-dimensional conformal radiation therapy affects the outcome in prostate cancer.* Int. J. Radiat. Oncol. Biol. Phys, 1998. **41**(3): p. 491-500.

61. Bai, M., et al., *CHALLENGES OF FAIR PHASE 0 **. 2019.

62. Badura, E., et al., *Control system for cancer therapy with a heavy ion beam at GSI.* IEEE Transactions on Nuclear Science, 2000. **47**(2): p. 170-173.

63. Ondreka, D., et al. *RECOMMISSIONING OF SIS18 AFTER FAIR UPGRADES*. 2019.

64. Steiner, M., et al., *Preliminary measurements of SIS 18 beam parameters.* Nucl. Instrum. Meth. , 1992. **312**(3): p. 420-424.

65. Jacso, F., A. Kouznetsov, and W.L. Smith, *Development and evaluation of an ultrasound-guided tracking and gating system for hepatic radiotherapy.* Med Phys, 2009. **36**(12): p. 5633-5640.

66. Lipiński, M., et al. *White Rabbit Applications and Enhancements*. in *2018 IEEE International Symposium on Precision Clock Synchronization for Measurement, Control, and Communication (ISPCS)*. 2018.

67. Weber, U. and G. Kraft, *Design and construction of a ripple filter for a smoothed depth dose distribution in conformal particle therapy.* Phys. Med. Biol, 1999. **44**(11): p. 2765-2775.

68. La Rosa, A., et al., *A pixel ionization chamber used as beam monitor at the Institut Curie—Centre de Protontherapie de Orsay (CPO).* Nucl. Instrum. Meth., 2006. **565**: p. 833-840.

69. Benedikt, M. and A. Wrulich, *MedAustron—Project overview and status.* The European Physical Journal Plus, 2011. **126**(7): p. 69.

70. Fausti, F., et al., *Design and characterization of a 64 channels ASIC front-end electronics for high-flux particle beam detectors.* Nucl. Instrum. Meth. , 2017. **867**: p. 1-6.

71. Veis, N.D., et al., *Performance studies of the PANDA planar GEM-tracking detector in physics simulations.* Nucl. Instrum. Meth. A 2018. **884**: p. 150-156.

72. Garcia, F., et al., *A GEM-TPC in twin configuration for the Super-FRS tracking of heavy ions at FAIR.* Nucl. Instrum. Meth., 2018. **884**: p. 18-24.

73. Simeonov, Y., et al., *3D range-modulator for scanned particle therapy: development, Monte Carlo simulations and experimental evaluation.* Phys. Med. Biol., 2017. **62**(17): p. 7075-7096.

74. Stöhlker, T., et al., *APPA at FAIR: From fundamental to applied research.* Nucl. Instrum. Meth. , 2015. **365**: p. 680-685.

75. Saito, N., et al., *Prediction methods for synchronization of scanned ion beam tracking.* Technology in Cancer Research & Treatment, 2010.

76. Krämer, M., et al., *Treatment planning for heavy-ion radiotherapy: physical beam model and dose optimization.* Phys. Med. Biol, 2000. **45**(11): p. 3299-3317.

77. Krämer, M. and M. Scholz, *Treatment planning for heavy-ion radiotherapy: calculation and optimization of biologically effective dose.* Phys. Med. Biol, 2000. **45**(11): p. 3319-3330.

78. Wolf, M.E., *Robust optimization in 4D treatment planning for carbon ion therapy of lung tumors*, in *Physics*. 2018, Technical University of Darmstadt: Darmstadt.

79. Hoss, A., et al., *COMPUTERVERFAHREN IN DER DREIDIMENSIONALEN STRAHLENTHERAPIEPLANUNG.* Radiologe, 1995. **35**(9): p. 583-586.

80. Martisíková, M., et al., *Use of Gafchromic (R) EBT films in heavy ion therapy.* Nuclear Instruments & Methods in Physics Research Section A-accelerators Spectrometers Detectors and Associated Equipment - NUCL INSTRUM METH PHYS RES A, 2008. **591**: p. 171-173.

81. Darmstadt, G. *Biophysics & Radio-Biology Program Advisory Committee (Bio-PAC)*. 2020; Available from: https://www.gsi.de/en/work/organisation/scientific_boards/pac/bio_pac.htm.

82. Kanai, T., et al., *Irradiation of mixed beam and design of spread-out Bragg peak for heavy-ion radiotherapy.* Radiat. Res, 1997. **147**(1): p. 78-85.

83. Saito, N., et al., *Prediction methods for synchronization of scanned ion beam tracking.* Phys Med, 2013. **29**(6): p. 639-43.

84. Sato, S., T. Furukawa, and K. Noda, *Dynamic intensity control system with RF-knockout slow-extraction in the HIMAC synchrotron.* Nuclear Instruments and Methods in Physics Research Section A: Accelerators, Spectrometers, Detectors and Associated Equipment, 2007. **574**(2): p. 226-231.

85. Vignati, A., et al., *Accuracy assessment of the CNAO dose delivery system in the initial period of clinical activity and impact of later improvements on delivered dose distributions.* Medical Physics, 2020. **47**(4): p. 1468-1480.

86. Hara, Y., et al., *Commissioning of full energy scanning irradiation with carbon-ion beams ranging from 55.6 to 430MeV/u at the NIRS-HIMAC.* Nucl. Instrum. Meth., 2017. **406**: p. 343-346.

87. Hara, Y., et al., *Application of radiochromic film for quality assurance in the heavy-ion beam scanning irradiation system at HIMAC.* Nuclear Instruments and Methods in Physics Research Section B: Beam Interactions with Materials and Atoms, 2014. **331**: p. 253-256.

88. Furukawa, T., et al., *Design study of a raster scanning system for moving target irradiation in heavy-ion radiotherapy.* Med. Phys, 2007. **34**(3): p. 1085-1097.

89. Laube, K., et al., *4D particle therapy PET simulation for moving targets irradiated with scanned ion beams.* Phys Med Biol, 2013. **58**(3): p. 513-33.

90. Council, E.R. *Biomedical Applications of Radioactive ion Beams*. 2020 [cited 2020 August, 27, 2020]; Available from: https://cordis.europa.eu/project/id/883425.

91. Purdie, T.G., et al., *Respiration correlated cone-beam computed tomography and 4DCT for evaluating target motion in Stereotactic Lung Radiation Therapy.* Acta Oncol, 2006. **45**(7): p. 915-922.

92. ICRU, *ICRU Report 78: Prescribing, Recording and Reporting Proton-Beam Therapy.* Journal of the ICRU, 2007. **7**(2): p. 1-210.

93. Nath, R., et al., *AAPM code of practice for radiotherapy accelerators: Report of AAPM Radiation Therapy Task Group No. 45.* Medical Physics, 1994. **21**(7): p. 1093-1121.

94. Mestrovic, A., et al., *Direct aperture optimization for online adaptive radiation therapy.* Med. Phys, 2007. **34**(5): p. 1631-1646.

95. Commission, I.E. *Guidelines for Radiotherapy Treatment Rooms Design*. 1997 1997 [cited 2020 06.10.2020]; Available from: https://global.ihs.com/doc_detail.cfm?document_name=IEC%2FTR%2061859&item_s_key=00257408#abstract-section.

96. Kutcher, G.J., et al., *Comprehensive QA for radiation oncology: Report of AAPM Radiation Therapy Committee Task Group 40.* Medical Physics, 1994. **21**(4): p. 581-618.

97. Klein, E.E., et al., *Task Group 142 report: Quality assurance of medical acceleratorsa).* Medical Physics, 2009. **36**(9Part1): p. 4197-4212.

98. Fraass, B., et al., *American Association of Physicists in Medicine Radiation Therapy Committee Task Group 53: Quality assurance for clinical radiotherapy treatment planning.* Medical Physics, 1998. **25**(10): p. 1773-1829.

99. *Quality Assurance in Radiotherapy*. 1998, Vienna: INTERNATIONAL ATOMIC ENERGY AGENCY.

100. Guckenberger, M., et al., *ESTRO ACROP consensus guideline on implementation and practice of stereotactic body radiotherapy for peripherally located early stage non-small cell lung cancer.* Radiotherapy and Oncology, 2017. **124**(1): p. 11-17.

101. Arjomandy, B., et al., *AAPM task group 224: Comprehensive proton therapy machine quality assurance.* Medical Physics, 2019. **46**(8): p. e678-e705.

102. Health, N.I.o. *PAR-13-371: Planning for a National Center for Particle Beam Radiation Therapy Research (P20)*. p20 Exploratory Grants 2013 03.10.2013 [cited 2020 06.10.2020]; Available from: https://grants.nih.gov/grants/guide/pa-files/PAR-13-371.html.

103. Huq, M.S., et al., *The report of Task Group 100 of the AAPM: Application of risk analysis methods to radiation therapy quality management.* Medical Physics, 2016. **43**(7): p. 4209-4262.

104. Ishikura, S., *Quality Assurance of Radiotherapy in Cancer Treatment: Toward Improvement of Patient Safety and Quality of Care.* Japanese Journal of Clinical Oncology, 2008. **38**(11): p. 723-729.

105. Fallon, E.F., L. Chadwick, and W. van der Putten. *Learning from Risk Assessment in Radiotherapy*. in *Digital Human Modeling*. 2009. Berlin, Heidelberg: Springer Berlin Heidelberg.

106. Malicki, J., et al., *Patient safety in external beam radiotherapy, results of the ACCIRAD project: Current status of proactive risk assessment, reactive analysis of events, and reporting and learning systems in Europe.* Radiotherapy and Oncology, 2017. **123**(1): p. 29-36.

107. Koo, J., et al., *Radiotherapy Risk Estimation Based on Expert Group Survey.* Frontiers in Physics, 2019. **7**(118).

108. Veronese, I., et al., *Multi-institutional application of Failure Mode and Effects Analysis (FMEA) to CyberKnife Stereotactic Body Radiation Therapy (SBRT).* Radiation oncology (London, England), 2015. **10**: p. 132-132.

109. Faught, J.T., et al., *An FMEA evaluation of intensity modulated radiation therapy dose delivery failures at tolerance criteria levels.* Medical physics, 2017. **44**(11): p. 5575-5583.

110. Ralston, A., et al., *The RABBIT risk-based approach to clinical implementation of new technology: SRS as a case study.* Technical Innovations & Patient Support in Radiation Oncology, 2020. **14**: p. 51-60.

111. Cantone, M.C., et al., *Application of failure mode and effects analysis to treatment planning in scanned proton beam radiotherapy.* Radiation oncology (London, England), 2013. **8**: p. 127-127.

112. Broggi, S., et al., *Application of failure mode and effects analysis (FMEA) to pretreatment phases in tomotherapy.* Journal of Applied Clinical Medical Physics, 2013. **14**(5): p. 265-277.

113. Kim, J., et al., *FMEA of MR-Only Treatment Planning in the Pelvis.* Advances in Radiation Oncology, 2019. **4**(1): p. 168-176.

114. Dueck, J., et al., *Robustness of the Voluntary Breath-Hold Approach for the Treatment of Peripheral Lung Tumors Using Hypofractionated Pencil Beam Scanning Proton Therapy.* International Journal of Radiation Oncology*Biology*Physics, 2016. **95**(1): p. 534-541.

115. Grassberger, C., et al., *Motion mitigation for lung cancer patients treated with active scanning proton therapy.* Medical Physics, 2015. **42**(5): p. 2462-2469.

116. Mori, S., A.-C. Knopf, and K. Umegaki, *Motion management in particle therapy.* Medical Physics, 2018. **45**(11): p. e994-e1010.

117. Fracchiolla, F., et al., *Implementation of proton therapy treatments with pencil beam scanning of targets with limited intrafraction motion.* Physica Medica, 2019. **57**: p. 215-220.

118. Fattori, G., et al., *Monitoring of breathing motion in image-guided PBS proton therapy: comparative analysis of optical and electromagnetic technologies.* Radiation Oncology, 2017. **12**(1): p. 63.

119. Bertholet, J., et al., *Real-time intrafraction motion monitoring in external beam radiotherapy.* Physics in Medicine & Biology, 2019. **64**(15): p. 15TR01.

120. *The World Health Report 2008: Global Initiative on Radiation Safety in Healthcare Settings*, in *Technical Meeting Report*. 2008, World Health Organization.

121. Bloch, H.P. and F.K. Geitner, *Preface*, in *Machinery Failure Analysis and Troubleshooting (Fourth Edition)*, F.K. Geitner and H.P. Bloch, Editors. 2012, Butterworth-Heinemann: Oxford. p. xv.

122. Lujan, A.E., J.M. Balter, and R.K. Ten Haken, *A method for incorporating organ motion due to breathing into 3D dose calculations in the liver: Sensitivity to variations in motion.* Medical Physics, 2003. **30**(10): p. 2643-2649.

123. McKenzie, E.M., et al., *Reproducibility in patient-specific IMRT QA.* Journal of applied clinical medical physics, 2014. **15**(3): p. 4741-4741.

124. Kataria, T., et al., *Homogeneity Index: An objective tool for assessment of conformal radiation treatments.* J Med Phys, 2012. **37**: p. 207-13.

125. McCaw, T.J., J.A. Micka, and L.A. DeWerd, *Development and characterization of a three-dimensional radiochromic film stack dosimeter for megavoltage photon beam dosimetry.* Medical Physics, 2014. **41**(5): p. 052104.

126. Henkner, K., et al., *A motorized solid-state phantom for patient-specific dose verification in ion beam radiotherapy.* Physics in Medicine and Biology, 2015. **60**: p. 7151.

127. Choi, K., et al., *FRoG-A New Calculation Engine for Clinical Investigations with Proton and Carbon Ion Beams at CNAO.* Cancers (Basel), 2018. **10**(11).

128. Karger, C.P., O. Jäkel, and G.H. Hartmann, *A system for three-dimensional dosimetric verification of treatment plans in intensity-modulated radiotherapy with heavy ions.* Med. Phys, 1999. **26**(10): p. 2125-2132.

129. Meschini, G., et al., *Evaluation of residual abdominal tumour motion in carbon ion gated treatments through respiratory motion modelling.* Physica Medica, 2017. **34**: p. 28-37.

130. Bevins, N.B., et al., *Practical application of AAPM Report 270 in display quality assurance: A report of Task Group 270.* Medical Physics, 2020. **n/a**(n/a).

131. Filippini, R. and P. Urschütz, *Risk management for a particle therapy accelerator: The MedAustron experience*. 2018. p. 1879-1886.

132. Arjomandy, B., et al., *Use of a two-dimensional ionization chamber array for proton therapy beam quality assurance.* Med. Phys, 2008. **35**(9): p. 3889-3894.

133. Matter, M., et al., *Alternatives to patient specific verification measurements in proton therapy: a comparative experimental study with intentional errors.* Physics in Medicine & Biology, 2018. **63**(20): p. 205014.

134. Maryanski, M.J., et al., *NMR relaxation enhancement in gels polymerized and cross-linked by ionizing radiation: A new approach to 3D dosimetry by MRI.* Magnetic Resonance Imaging, 1993. **11**(2): p. 253-258.

135. Schuy, C., et al., *Technical note: Vendor-agnostic water phantom for 3D dosimetry of complex fields in particle therapy.* Journal of Applied Clinical Medical Physics, 2020. **21**(10): p. 227-232.

136. Lin, L., et al., *Use of a novel two-dimensional ionization chamber array for pencil beam scanning proton therapy beam quality assurance.* Journal of Applied Clinical Medical Physics, 2015. **16**: p. 270.

137. Lima, T.V.M., et al., *Monte Carlo Calculations Supporting Patient Plan Verification in Proton Therapy.* Frontiers in Oncology, 2016. **6**(62).

138. Kamada, T., et al., *Carbon ion radiotherapy in Japan: an assessment of 20 years of clinical experience.* Lancet Oncol, 2015. **16**(2): p. e93-e100.

139. Chun, S.G., et al., *Impact of Intensity-Modulated Radiation Therapy Technique for Locally Advanced Non-Small-Cell Lung Cancer: A Secondary Analysis of the NRG Oncology RTOG 0617 Randomized Clinical Trial.* Journal of clinical oncology : official journal of the American Society of Clinical Oncology, 2017. **35**(1): p. 56-62.

140. Rios, J., et al., *Treatment and outcomes of non-small-cell lung cancer patients with high comorbidity.* Cancer management and research, 2018. **10**: p. 167-175.

141. Wang, Y., et al., *Assessment of respiration-induced motion and its impact on treatment outcome for lung cancer.* BioMed research international, 2013. **2013**: p. 872739-872739.

142. Bradley, J.D., et al., *Standard-dose versus high-dose conformal radiotherapy with concurrent and consolidation carboplatin plus paclitaxel with or without cetuximab for patients with stage IIIA or IIIB non-small-cell lung cancer (RTOG 0617): a randomised, two-by-two factorial phase 3 study.* Lancet Oncol, 2015. **16**(2): p. 187-99.

143. Trnkova, P., et al., *Clinical implementations of 4D pencil beam scanned particle therapy: Report on the 4D treatment planning workshop 2016 and 2017.* Phys Med, 2018. **54**: p. 121-130.

144. Eley, J.G., et al., *Robustness of target dose coverage to motion uncertainties for scanned carbon ion beam tracking therapy of moving tumors.* Physics in Medicine and Biology, 2015. **60**(4): p. 1717-1740.

145. Richter, D., et al., *Four-dimensional patient dose reconstruction for scanned ion beam therapy of moving liver tumors.* Int J Radiat Oncol Biol Phys, 2014. **89**(1): p. 175-81.

146. Wolf, M.E., et al., *Robust treatment planning with 4D intensity modulated carbon ion therapy for multiple targets in stage IV non-small cell lung cancer.* Phys Med Biol, 2020.

147. Lis, M., et al., *A facility for the research, development, and translation of advanced technologies for ion-beam therapies.* Journal of Instrumentation, 2020.

148. Lis, M., et al., *A facility for the research, development, and translation of advanced technologies for ion-beam therapies.* Journal of Instrumentation, 2021. **16**(03): p. T03004.

149. Saito, N., et al. *Technical accuracy of a beam tracking system for scanned particle therapy of intra-fractionally moving targets*. in *World Congress on Medical Physics*. 2009. Munich, Germany: Springer.

150. Lauve, A., et al., *Simultaneous integrated boost intensity-modulated radiotherapy for locally advanced head-and-neck squamous cell carcinomas: II—clinical results.* International Journal of Radiation Oncology*Biology*Physics, 2004. **60**(2): p. 374-387.

151. Wilson, L.J., W.D. Newhauser, and C.W. Schneider, *An objective method to evaluate radiation dose distributions varying by three orders of magnitude.* Medical Physics, 2019. **46**(4): p. 1888-1895.

152. Luoni, F., et al., *Beam Monitor Calibration for Radiobiological Experiments With Scanned High Energy Heavy Ion Beams at FAIR.* Frontiers in Physics, 2020. **8**(397).

153. Lis, M., et al., *A Modular System for Treating Moving Anatomical Targets With Scanned Ion Beams at Multiple Facilities: Pre-Clinical Testing for Quality and Safety of Beam Delivery.* Frontiers in Oncology, 2021. **11**(323).

154. Stelljes, T.S., et al., *Dosimetric characteristics of the novel 2D ionization chamber array OCTAVIUS Detector 1500.* Medical Physics, 2015. **42**(4): p. 1528-1537.

155. Yonai, S., et al., *Experimental evaluation of dosimetric characterization of Gafchromic EBT3 and EBT-XD films for clinical carbon ion beams.* Radiation Protection Dosimetry, 2018. **180**(1-4): p. 314-318.

156. Reinhardt, S., et al., *Investigation of EBT2 and EBT3 films for proton dosimetry in the 4–20 MeV energy range.* Radiation and Environmental Biophysics, 2015. **54**(1): p. 71-79.

157. Saito, N., et al., *Speed and accuracy of a beam tracking system for treatment of moving targets with scanned ion beams.* Phys. Med. Biol, 2009. **54**(16): p. 4849-4862.

158. Lis, M., et al., *Preliminary tests of dosimetric quality and projected therapeutic outcomes of multi-phase 4D radiotherapy with proton and carbon ion beams* Frontiers in Oncology, 2021.

159. Bert, C., S.O. Grözinger, and E. Rietzel, *Quantification of interplay effects of scanned particle beams and moving targets.* Phys. Med. Biol, 2008. **53**(9): p. 2253-2265.

160. Lüchtenborg, R., et al., *On-line compensation of dose changes caused by intrafractional tumor motion.* Radiotherapy and Oncology, 2010. **96**(S1): p. S539.

161. Lis, M., et al., *A modular system for treating moving anatomical targets with scanned ion beams at multiple facilities; pre-clinical testing for quality and safety of beam delivery* in *Frontiers in Oncology*. 2021.

162. Karube, M., et al., *Carbon-ion pencil beam scanning for thoracic treatment - initiation report and dose metrics evaluation.* Journal of radiation research, 2016. **57**(5): p. 576-581.

163. Bolwin, K., et al., *Anthropomorphic thorax phantom for cardio-respiratory motion simulation in tomographic imaging.* Physics in Medicine and Biology, 2018. **63**(3): p. 035009.

164. den Boer, E., et al., *Technical Note: Investigating interplay effects in pencil beam scanning proton therapy with a 4D XCAT phantom within the RayStation treatment planning system.* Medical Physics, 2021. **48**(3): p. 1448-1455.

165. Shih, H.A., et al., *Internal target volume determined with expansion margins beyond composite gross tumor volume in three-dimensional conformal radiotherapy for lung cancer.* International Journal of Radiation Oncology*Biology*Physics, 2004. **60**(2): p. 613-622.

166. Giraud, P. and A. Houle, *Respiratory Gating for Radiotherapy: Main Technical Aspects and Clinical Benefits.* ISRN Pulmonology, 2013. **2013**: p. 519602.

167. Schulz-Ertner, D. and H. Tsujii, *Particle Radiation Therapy Using Proton and Heavier Ion Beams.* Journal of Clinical Oncology, 2007. **25**(8): p. 953-964.

168. Schlaff, C.D., et al., *Bringing the heavy: carbon ion therapy in the radiobiological and clinical context.* Radiation Oncology, 2014. **9**(1): p. 88.

169. Mohamad, O., et al., *Carbon Ion Radiotherapy: A Review of Clinical Experiences and Preclinical Research, with an Emphasis on DNA Damage/Repair.* Cancers, 2017. **9**(6): p. 66.

170. Chi, A., et al., *Systemic review of the patterns of failure following stereotactic body radiation therapy in early-stage non-small-cell lung cancer: Clinical implications.* Radiotherapy and Oncology, 2010. **94**(1): p. 1-11.

171. Bradley, J.D., et al., *Standard-dose versus high-dose conformal radiotherapy with concurrent and consolidation carboplatin plus paclitaxel with or without cetuximab for patients with stage IIIA or IIIB non-small-cell lung cancer (RTOG 0617): a randomised, two-by-two factorial phase 3 study.* The Lancet Oncology, 2015. **16**(2): p. 187-199.

172. Tucker, S.L., et al., *Validation of Effective Dose as a Better Predictor of Radiation Pneumonitis Risk Than Mean Lung Dose: Secondary Analysis of a Randomized Trial.* International Journal of Radiation Oncology*Biology*Physics, 2019. **103**(2): p. 403-410.

173. Shipley, W.U., et al., *Advanced prostate cancer: The results of a randomized comparative trial of high dose irradiation boosting with conformal protons compared with conventional dose irradiation using photons alone.* International Journal of Radiation Oncology*Biology*Physics, 1995. **32**(1): p. 3-12.

174. Liao, Z., et al., *Bayesian Adaptive Randomization Trial of Passive Scattering Proton Therapy and Intensity-Modulated Photon Radiotherapy for Locally Advanced Non–Small-Cell Lung Cancer.* Journal of Clinical Oncology, 2018. **36**(18): p. 1813-1822.

175. Brandner, E.D., et al., *Motion management strategies and technical issues associated with stereotactic body radiotherapy of thoracic and upper abdominal tumors: A review from NRG oncology.* Medical Physics, 2017. **44**(6): p. 2595-2612.

176. Bert, C. and K. Herfarth, *Management of organ motion in scanned ion beam therapy.* Radiation Oncology, 2017. **12**(1): p. 170.

177. Hanley, J., et al., *Deep inspiration breath-hold technique for lung tumors: the potential value of target immobilization and reduced lung density in dose escalation.* International Journal of Radiation Oncology*Biology*Physics, 1999. **45**(3): p. 603-611.

178. Lin, L., et al., *Evaluation of motion mitigation using abdominal compression in the clinical implementation of pencil beam scanning proton therapy of liver tumors.* Medical Physics, 2017. **44**(2): p. 703-712.

179. Seppenwoolde, Y., et al., *Treatment precision of image-guided liver SBRT using implanted fiducial markers depends on marker–tumour distance.* Physics in Medicine and Biology, 2011. **56**(17): p. 5445-5468.

180. Chi, A., et al., *Comparison of photon volumetric modulated arc therapy, intensity-modulated proton therapy, and intensity-modulated carbon ion therapy for delivery of hypo-fractionated thoracic radiotherapy.* Radiation Oncology, 2017. **12**(1): p. 132.

181. Dokic, I., et al., *Next generation multi-scale biophysical characterization of high precision cancer particle radiotherapy using clinical proton, helium-, carbon- and oxygen ion beams.* Oncotarget, 2016. **7**(35): p. 56676-56689.

182. Grun, R., et al., *Assessment of potential advantages of relevant ions for particle therapy: a model based study.* Med Phys, 2015. **42**(2): p. 1037-47.

183. Weber, U. and G. Kraft, *Comparison of carbon ions versus protons.* Cancer J, 2009. **15**(4): p. 325-332.

184. Schlaff, C.D., et al., *Bringing the heavy: carbon ion therapy in the radiobiological and clinical context.* Radiation oncology (London, England), 2014. **9**(1): p. 88-88.

185. Shirai, K., et al., *Clinical outcomes using carbon-ion radiotherapy and dose-volume histogram comparison between carbon-ion radiotherapy and photon therapy for T2b-4N0M0 non-small cell lung cancer—A pilot study.* PLOS ONE, 2017. **12**(4): p. e0175589.

186. Liermann, J., et al., *Carbon ion radiotherapy as definitive treatment in non-metastasized pancreatic cancer: study protocol of the prospective phase II PACK-study.* BMC Cancer, 2020. **20**(1): p. 947.

187. Anzai, M., et al., *Safety and Efficacy of Carbon-ion Radiotherapy Alone for Stage III Non-small Cell Lung Cancer.* Anticancer Research, 2020. **40**(1): p. 379.

188. Krämer, M. and O. Jäkel, *Therapy Planning for Heavy Ion Irradiation*. 1997.

189. Bert, C., et al., *Rescanning to mitigate the impact of motion in scanned particle therapy,* in *GSI Scientific Report 2008,* K. Große, Editor. 2009: Darmstadt, Germany. p. 397.

190. Lis, M., et al., *Dosimetric validation of a modular system to treat moving tumors using scanned ion beams that are synchronized with anatomical motion.* Submitted, 2021.

191. Rowe, B.P., et al., *Stereotactic Body Radiotherapy for Central Lung Tumors.* Journal of Thoracic Oncology, 2012. **7**(9): p. 1394-1399.

192. Marks, L.B., et al., *Use of Normal Tissue Complication Probability Models in the Clinic.* International Journal of Radiation Oncology*Biology*Physics, 2010. **76**(3, Supplement): p. S10-S19.

193. Lambrecht, M., et al., *Radiation dose constraints for organs at risk in neuro-oncology; the European Particle Therapy Network consensus.* Radiotherapy and Oncology, 2018. **128**(1): p. 26-36.

194. A, M. and O. M., *An overview on the clinical application of radiobiological modeling in radiation therapy of cancer* Int J Radiol Radiat Ther., 2016. **2**(1): p. 9-14.

195. Zaider, M. and L. Hanin, *Tumor control probability in radiation treatment.* Medical Physics, 2011. **38**(2): p. 574-583.

196. Paz, A.E., et al., *Tumor Control Probability Analysis for Single-Fraction Carbon-Ion Radiation Therapy of Early-Stage Non-small Cell Lung Cancer.* International Journal of Radiation Oncology*Biology*Physics, 2018. **102**(5): p. 1551-1559.

197. Sanchez-Nieto, B. and A.E. Nahum, *The delta-TCP concept: a clinically useful measure of tumor control probability.* International Journal of Radiation Oncology*Biology*Physics, 1999. **44**(2): p. 369-380.

198. Rutkowska, E., C. Baker, and A. Nahum, *Mechanistic simulation of normal-tissue damage in radiotherapy-–implications for dose–volume analyses.* Physics in Medicine and Biology, 2010. **55**(8): p. 2121-2136.

199. Stavrev, P., et al., *On differences in radiosensitivity estimation: TCP experiments versus survival curves. A theoretical study.* Physics in Medicine and Biology, 2015. **60**(15): p. N293-N299.

200. Gay, H.A. and A. Niemierko, *A free program for calculating EUD-based NTCP and TCP in external beam radiotherapy.* Physica Medica, 2007. **23**(3): p. 115-125.

201. A, C., et al., *What should we know about photon dose calculationalgorithms used for radiotherapy? Their impact on dose distribution and medical decisions based on TCP/NTCP.* Int J Cancer TherOncol, 2016. **4**(4): p. 4418.

202. Martel, M.K., et al., *Estimation of tumor control probability model parameters from 3-D dose distributions of non-small cell lung cancer patients.* Lung Cancer, 1999. **24**(1): p. 31-37.

203. Scheenstra, A.E.H., et al., *Alpha/Beta Ratio for Normal Lung Tissue as Estimated From Lung Cancer Patients Treated With Stereotactic Body and Conventionally Fractionated Radiation Therapy.* International Journal of Radiation Oncology*Biology*Physics, 2014. **88**(1): p. 224-228.

204. Schultz-Hector, S., M. Sund, and H.D. Thames, *Fractionation response and repair kinetics of radiation-induced heart failure in the rat.* Radiotherapy and Oncology, 1992. **23**(1): p. 33-40.

205. Klement, R.J., et al., *Estimation of the α/ β ratio of non-small cell lung cancer treated with stereotactic body radiotherapy.* Radiotherapy and Oncology, 2020. **142**: p. 210-216.

206. Sun, L.-M., et al., *Concomitant boost radiation therapy for inoperable non–small-cell lung cancer: preliminary report of a prospective randomized study.* International Journal of Radiation Oncology*Biology*Physics, 2000. **47**(2): p. 413-418.

207. Emami, B., et al., *Tolerance of normal tissue to therapeutic irradiation.* International Journal of Radiation Oncology, Biology, Physics, 1991. **21**(1): p. 109-122.

208. Okunieff, P., et al., *Radiation dose-response of human tumors.* International Journal of Radiation Oncology, Biology, Physics, 1995. **32**(4): p. 1227-1237.

209. Vlachaki, M., et al., *Impact of Respiratory Gating Using 4-Dimensional Computed Tomography on the Dosimetry of Tumor and Normal Tissues in Patients With Thoracic Malignancies.* American Journal of Clinical Oncology, 2009. **32**(3).

210. Niemierko, A. and M. Goitein, *Dose-volume distributions: a new approach to dose-volume histograms in three-dimensional treatment planning.* Med Phys, 1994. **21**(1): p. 3-11.

211. Chang, J.H., et al., *RADBIOMOD: A simple program for utilising biological modelling in radiotherapy plan evaluation.* Physica Medica, 2016. **32**(1): p. 248-254.

212. Gagliardi, G., et al., *Radiation Dose-Volume Effects in the Heart.* International Journal of Radiation Oncology, Biology, Physics, 2010. **76**(3): p. S77-S85.

213. Seppenwoolde, Y., et al., *Comparing different NTCP models that predict the incidence of radiation pneumonitis.* International Journal of Radiation Oncology, Biology, Physics, 2003. **55**(3): p. 724-735.

214. Semenenko, V.A. and X.A. Li, *Lyman–Kutcher–Burman NTCP model parameters for radiation pneumonitis and xerostomia based on combined analysis of published clinical data.* Physics in Medicine and Biology, 2008. **53**(3): p. 737-755.

215. Mori, S., et al., *A serial 4DCT study to quantify range variations in charged particle radiotherapy of thoracic cancers.* J Radiat Res, 2014. **55**(2): p. 309-19.

216. Niemierko, A. and M. Goitein, *Calculation of normal tissue complication probability and dose-volume histogram reduction schemes for tissues with a critical element architecture.* Radiotherapy and Oncology, 1991. **20**(3): p. 166-176.

217. Dokic, I., et al., *Next generation multi-scale biophysical characterization of high precision cancer particle radiotherapy using clinical proton, helium-, carbon- and oxygen ion beams.* Oncotarget; Vol 7, No 35, 2016.

218. Tommasino, F., A. Nahum, and L. Cella, *Increasing the power of tumour control and normal tissue complication probability modelling in radiotherapy: recent trends and current issues.* Translational Cancer Research, 2017: p. S807-S821.

219. Furukawa, T., et al., *Performance of the NIRS fast scanning system for heavy-ion radiotherapy.* Medical Physics, 2010. **37**(11): p. 5672-5682.

Vita

Michelle Lis was born in Chicago, Illinois to Krystyna Lis and Stanislaw Lis. After graduating from Maine Township Highschool South, she attended Loyola University Chicago, where she majored in physics and molecular biology and minored in math. The summer before her final year of her studies, she was awarded a summer research fellowship at Loyola Medical Center, where she first discovered medical physics and decided to pursue a career in that direction. After she earned a Bachelors in Science in 2010, she worked as a Software QA for one year before beginning her graduate studies at Louisiana State University. During her second year of studies, Michelle was awarded the Optimization of Medical Accelerators Marie-Sklodowska Curie Actions ITN fellowship. She moved to Darmstadt, Germany in January, 2017 to begin her research, and slowly integrated into German life. During her doctoral studies, Michelle took up climbing and bouldering, and would spend weekends climbing in the local gyms and crags. She also discovered CrossFit, aerial silks and began to participate in various obstacle course runs. Upon completion of her dissertation, Michelle will begin working in industry, where she will apply her expertise in medical physics research to managing the development of new technologies.